Title

Intratumoral Dendritic Cell Vaccine Reprograms the Tumor Microenvironment and Enhances the Efficacy of Immune Checkpoint Blockade in Non-Small Cell Lung Cancer

Author

Lim, Raymond John S

Publication Date

2022

Peer reviewed|Thesis/dissertation

UNIVERSITY OF CALIFORNIA

Los Angeles

Intratumoral Dendritic Cell Vaccine Reprograms the Tumor Microenvironment and Enhances the Efficacy of Immune Checkpoint Blockade in Non-Small Cell Lung Cancer

A dissertation submitted in partial satisfaction of the requirements for the degree

Doctor of Philosophy in Molecular and Medical Pharmacology

by

Raymond John S Lim

2022

ABSTRACT OF THE DISSERTATION

Intratumoral Dendritic Cell Vaccine Reprograms the Tumor Microenvironment and Enhances the Efficacy of Immune Checkpoint Blockade in Non-Small Cell Lung Cancer

by

Raymond John S Lim

Doctor of Philosophy in Molecular and Medical Pharmacology

University of California, Los Angeles, 2022

Professor Steven M. Dubinett, Chair

Lung cancer remains the most common cause of cancer death worldwide with approximately 85% of patients having non-small cell lung cancer (NSCLC). Checkpoint blockade immunotherapy has evolved the current treatment landscape with robust and durable responses in approximately 20% of patients with progressive, locally advanced, or metastatic NSCLC, as well as in treatment-naïve advanced disease. Inefficient tumor antigen presentation, diminished T cell infiltration into tumor and LKB1-inactivating mutations contribute to the mechanisms of resistance to programmed death-ligand 1 (PD-L1) or programmed cell death protein 1 (PD-1) blockade in NSCLC. One approach to overcome this immunosuppressive tumor microenvironment (TME) is to utilize *in situ* vaccination with gene-modified functional antigen presenting cells (APCs) to enhance tumor antigen presentation and promote tumor-specific T cell activation. Here I address two potential therapies: 1) CCL21-genetically engineered dendritic cells (CCL21-DC) and 2) CXCL9/10-genetically engineered dendritic cells (CXCL9/10-DC), which are shown to remodel the tumor immune microenvironment and promote an anti-tumor immune response. In addition, the pre-clinical studies detailed here investigate the mechanisms of how these potential therapies can

potentiate checkpoint blockade immunotherapy. These preclinical models serve as a platform to enhance our understanding of the molecular mechanisms of response and resistance to immunotherapy. In addition, these studies provide insights to anti-tumor immunity mediated by *in situ* DC vaccination and may in turn facilitate the improvement of novel vaccine therapies. The final chapter addresses the pressing need for the development of innovative approaches to detect and intercept lung cancer at its earliest stages of development. Using spatial multiplex immunofluorescence, this chapter highlights the efforts to understand the immune landscape in the tumor microenvironment associated with early-stage lung carcinogenesis and provides further understanding of the mechanism of lung cancer evolution. Research focusing on the development of novel strategies for cancer interception prior to the progression to advanced stages will potentially lead to a paradigm shift in the treatment of lung cancer and have a major impact on clinical outcomes.

The dissertation of Raymond John S Lim is approved.

Bin Liu

Lily Wu

Michael Alan Teitell

Robert M. Prins

Steven M. Dubinett, Committee Chair

University of California, Los Angeles

2022

DEDICATION

This is dedicated to :

My family and friends who have supported me through all the difficult times.

My father who taught me to take the losses and focus on the bigger picture.

My mother – for her advice, her love, her patience, and faith

Because she always understood.

Whatever you do, do it all for the glory of God – 1 COR 10:31

TABLE OF CONTENTS

ACKNOWLEDGEMENTS

I would like to express my greatest thanks to my mentor Dr. Steven Dubinett for his patience, support, and guidance over the past years. I am very grateful for the opportunities that I have been provided with and the time spent learning from someone who truly is an inspiration.

I would like to express my deepest appreciation to my amazing committee members Dr. Bin Liu, Dr. Lily Wu, Dr. Michael Teitell, and Dr. Robert Prins for all their support and guidance.

I am blessed to have spent time under the tutelage of Dr. Bin Liu. Without her thoughtful encouragement and careful supervision, this thesis would never have taken shape. I gratefully acknowledge the support and guidance of Dr. Ramin Salehi-rad, Dr. Kostyantyn Krysan and Dr. Linh Tran. Thank you for challenging my ideas and providing me with fresh perspectives.

My thanks go out to those who kindly participated in this research by giving generously of their time. For Camelia Dumitras, who was always willing to help and always being available for lunch. For Dr. Rui Li, Stephanie Ong and Silvia Huang who got me started in the lab. For Jensen Abascal, William Crosson and other graduate students, who helped in the research. For the other members of the lab and those who have helped me on my past and current work, research is such a collaborative effort and all of this has been capable because of the help I have received.

I am grateful to the ones I taught for giving me another kind of education. My undergraduate and high school students: Ashley Carrillo, Tejas Patel, Samantha Man, Cara Yean, Dara Dooley and others. May the things you learned under my guidance lead to success in your future endeavors.

I would like to thank Dr. Aaron Mochizuki and Dr. Alex Lam for their help and guidance in life and preparation of this dissertation. I would also like to acknowledge my past mentors for guiding me in my early stages of research. I would not be here today had it not been for those critical years of learning.

Excerpts were taken for Chapter 3 from **Lim RJ**, Liu B, Krysan K, Dubinett SM. *Lung Cancer and Immunity Markers*. Cancer Epidemiol Biomarkers Prev. Focus section, "NCI Early Detection Research Network: Making Cancer Detection Possible." 2020 Dec;29(12):2423-2430. doi: 10.1158/1055-9965.EPI-20-0716.

My research was supported by the Tobacco-related Disease Research Program (TRDRP) Dissertation Award T30DT0963 and UCLA Technology Development Group 2020 Innovation Fund.

Vita

EDUCATION

2009	Bachelor of Science in Biochemistry and Molecular Biology University of California, Irvine *Summa Cum Laude*

EMPLOYMENT

2017	Biological Research Scientist – Retinal Disease Team Allergan, Inc
2013 – 2017	Senior Professional, Biology – Retinal Disease Team Allergan, Inc
2009 – 2013	Professional, Biology – Retinal Disease Team Allergan, Inc

AWARDS AND HONORS

2019 – 2022	Tobacco Related-Disease Research Program (TRDRP) Award for Pre-Doctoral Fellowship
2019	Ruth L. Kirschstein National Research Service Award Institutional Predoctoral T32 Training Program in Vascular Biology - Declined
2019	UCLA Department of Medicine Research Day Poster Award
2018	UCLA Department of Medicine Research Day Poster Award
2017	Allergan Award for Excellence of Research
2016	Allergan Award for Excellence of Research
2014	Allergan Award for Excellence of Research
2013	Allergan Award for Excellence of Research
2009	Undergraduate Research Opportunities Program Grant Recipient

PUBLICATIONS

Liu S, Knochelmann HM, Lomeli SH, Hong A, Richardson M, Yang Z, **Lim RJ**, Wang Y, Dumitras C, Krysan K, Timmers C, Romeo MJ, Krieg C, O'Quinn EC, Horton JD, Dubinett SM, Paulos CM, Neskey DM, and Lo RS. *Response and recurrence correlates in individuals treated with neoadjuvant anti-PD-1 therapy for resectable oral cavity squamous cell carcinoma.* Cell Reports Medicine 2021 Oct.

Saggese P, Martinez CA, Tran LM, **Lim RJ**, Dumitras C, Grogan T, Elashoff D, Salehi-Rad R, Dubinett SM, Liu B and Scafoglio S. *Genotoxic treatment enhances immune response in a genetic model of lung cancer.* Cancers 2021 July.

Li R*, Salehi-Rad R*, Crosson W, Momcilovic M, **Lim RJ**, Ong SL, Huang ZL, Zhang T, Abascal J, Dumitras C, Jing Z, Park SJ, Krysan K, Shackelford DB, Tran LM, Liu B, Dubinett SM. *Inhibition of granulocytic myeloid-derived suppressor cells overcomes resistance to immune checkpoint inhibition in LKB1-deficient non-small cell lung cancer.* Cancer Res. 2021 Apr.

Salehi-Rad R*, Li R*, Tran LM, **Lim RJ**, Abascal J, Momcilovic M, Park SJ, Ong SL, Shabihkhani M, Huang ZL, Paul M, Shackelford DB, Krysan K, Liu B, Dubinett SM.

Novel Kras-mutant murine models of non-small cell lung cancer possessing co-occurring Oncogenic mutations and increased tumor mutational burden. Cancer Immunol Immunother. 2021 Jan.

Lim RJ, Liu B, Krysan K, Dubinett SM. *Lung Cancer and Immunity Markers*. Cancer Epidemiol Biomarkers Prev. Focus section, "NCI Early Detection Research Network: Making Cancer Detection Possible." 2020 Dec.

Schwab K, Hamidi S, Chung A, **Lim RJ**, Khanlou N, Hoesterey D, Dumitras C, Adeyiga OB, Phan-Tang M, Wang TS, Saggar R, Goldstein J, Belperio JA, Dubinett SM, Kim JT, Salehi-Rad R. *Occult colonic perforation in a patient with coronavirus disease 2019 after interleukin-6 receptor antagonist therapy.* Open Forum Infectious Diseases 2020 Sept.

Janes MR, Limon JJ, So L, Chen J, **Lim RJ**, Chavez MA, Vu C, Lilly MB, Mallya S, Ong ST, Konopleva M, Martin MB, Ren P, Liu Y, Rommel C, Fruman DA. *Effective And selective targeting of leukemia cells using a TORC1/2 kinase inhibitor*. Nat Med. 2010 Feb.

POSTERS and PRESENTATIONS

2022 Poster	Association of American Cancer Research (AACR) Conference
2022 Oral presentation	UCLA Pharmacology Friday Seminar
2021 Poster	Lung Spore
2021 Oral presentation	UCLA Pharmacology Friday Seminar
2021 Oral presentation	SU2C Lung Cancer Interception Dream Team Teleconference
2020 Oral pitch	UCLA Technology Development Group Innovation Pitch Day
2020 Oral presentation	Johnson & Johnson Pre-Cancer Genome Atlas
2020 Oral presentation	UCLA Pharmacology Friday Seminar
2019 Poster	UCLA Department of Medicine Research Day
2019 Oral presentation	Lung SPORE
2019 Poster	Association of American Cancer Research (AACR) Conference
2018 Poster	UCLA Pharmacology Retreat
2018 Poster	UCLA Department of Medicine Research Day
2012 Poster	Association for Research Vision and Ophthalmology Conference
2011 Poster	Association for Research Vision and Ophthalmology Conference
2009 Poster	Undergraduate Research Opportunities Program Symposium

INTRODUCTION

LUNG CANCER TREATMENT PARADIGM

Critical need to improve the efficacy of ICB immunotherapy for NSCLC patients

Lung cancer is the leading cause of cancer death worldwide[1-3]. Nearly 83% of the patients will die of the disease within five years[4]. For patients with metastatic disease, the 5-year survival rate is 6%. Approximately 85% of lung cancer patients have NSCLC, among which lung adenocarcinoma (LUAD) and lung squamous cell carcinoma (LUSC) are the two major subtypes[5-7]. Recent advances in immunotherapy with immune checkpoint blockade (ICB), which includes Programmed Death-1/Programmed Death-Ligand 1 (PD-1/PD-L1) inhibition, have revolutionized the treatment of NSCLC with robust and durable responses in a subset of patients[7-10]. However, the majority of patients do not respond to ICB monotherapy (primary resistance) and others relapse after an initial response (acquired resistance)[11-13]. Although combination of ICB and chemotherapy as the front-line treatment in advanced stage NSCLC conferred a significantly improved objective response rate (ORR) and overall survival (OS), nearly half of the patients do not respond, and effective options are limited following disease progression[14-18].

Mechanisms of resistance to ICB immunotherapy

Studies reveal that responses to PD-1/PD-L1 blockade are associated with high tumor mutational burden (TMB), increased tumor infiltration of $CD8^+$ cytolytic T lymphocytes (CTLs), and high baseline tumor PD-L1 expression[19-24]. Recent studies further identified clonal neoantigen burden, a dormant tumor infiltrating lymphocyte (TIL) signature, an IFN signature and high CXCL9 expression in the tumor microenvironment (TME) as factors associated with clinical benefit of ICB[25-28]. In contrast, impaired tumor antigen presentation and an immunosuppressive TME are correlated with resistance to ICB[11-13,29,30]. When co-expressed in *KRAS*-mutant LUAD, *Liver Kinase B1* (*LKB1, also known as Serine/Threonine Kinase 11 or STK11)* inactivating mutations have been identified as a primary driver of resistance to anti-PD-1[31], which is associated with a predominance of myeloid-derived suppressor cells (MDSCs) and low PD-L1 expression in the

TME[32,33]. These data implicate tumor-specific host adaptive immune responses as the critical mediators of ICB efficacy. Therefore, strategies that enhance tumor antigen presentation and promote tumor-specific T cell responses hold significant potential for augmenting the efficacy of ICB in NSCLC refractory to ICB immunotherapy.

In situ vaccination with genetically-engineered dendritic cells as a novel strategy to improve ICB efficacy

Although lung cancers express tumor antigens, they do not function well as antigen presenting cells (APC) due to alterations in human leukocyte antigen (*HLA*) genes and transcriptional repression of neoantigen expression[29,30,34,35]. The tumor's lack of co-stimulatory molecules in combination with its production of inhibitory factors promotes an immunosuppressive TME[36-40]. Recent studies reveal that approximately 10% of pre-existing T cells in the TME are tumor-reactive T cells with limited reinvigoration capacity and that tumor-specific T cell responses derive from a distinct TCR repertoire recruited into the TME in response to ICB[41-44]. Therefore, the most effective therapeutic strategies are likely those that increase the frequency and breadth of tumor-specific T cell clones by enhancing tumor antigen presentation and T cell infiltration/activation in the TME. Our approach to improve the efficacy of ICB is *in situ* vaccination with chemokine gene-modified functional DC that takes advantage of the full repertoire of available tumor antigens to restore tumor antigen presentation. The engineered chemokine expression in the TME is designed to promote immune cell infiltration and ameliorate the immunosuppressive TME, leading to augmented and sustained tumor-specific T cell activation both locally and systemically. DC-based in situ vaccination has emerged as a potential component for immunotherapy due to both its favorable toxicity profile and its essential role in T cell priming and activation. DC vaccination may be enhanced in combination with other approaches that overcome T cell exhaustion, DC dysfunction and the immunosuppressive TME[45-49].

CHAPTER 1

CXCL9/CXCL10-ENGINEERED DENDRITIC CELLS

Rationale for CXCL9 and CXCL10

Checkpoint blockade has been shown to have limited efficacy in patients with *LKB1* loss caused by an immunosuppressive environment and poor T lymphocyte recruitment or activation[32,33]. It has been demonstrated that CXCL9/10 secreted by $CD103^+$ DCs are crucial for effector T lymphocyte infiltration and anti-tumor immunity[27-29,50,51]. Furthermore, CXCL9/10 have anti-angiogenic properties which can shift the angiogenic balance from tumor-induced angiogenesis to angiostasis which can help stabilize blood vessels for proper T cell trafficking into the tumor microenvironment[52 33]. T lymphocyte infiltration into the TME has been observed to correlate with anti-tumor efficacy[53,54]. Recruitment of these effector T lymphocytes, including $CD8^+$ effector T cells and $CD4^+$ non-T regulatory cells[28,34] are mediated via the CXCR3 receptor [30]. In fact, gene expression profiling has shown a strong correlation between the presence of $CD8^+$ T cells and expression of CXCL9 and CXCL10[29,35]. Recent studies have also revealed that somatic copy-number alterations (SCNAs) can be associated with loss of CXCL9/10, immune suppression, cytotoxic lymphocyte depletion in the tumor and failure to respond to ICB[55,56]. Thus, aneuploid-dependent immune suppression may require the addition of chemokines downstream of the interferon-gamma pathway for effective therapy in patients who lack the capacity for CXCL9/10 production. CXCL9 expression have also been found to be one of the strongest predictors favoring a successful ICB reponse in a pan-tumor analysis[28]. Therefore, we hypothesize that IT injection of *CXCL9/10-DCs can potentiate the response to anti-PD-1 monotherapy in LKB1-deficient NSCLC by promoting antigen presentation and inducing T cell infiltration elicit anti-tumor immunity*.

The CXCL9/10 and CXCR3 axis correlations with tumor-infiltrating immune cells in human NSCLC

To determine the association of *CXCL9/10* and *CXCR3* expression with immune infiltration, we analyzed The Cancer Genome Atlas (TCGA) NSCLC data of both lung adenocarcinoma (LUAD)

and lung squamous carcinoma (LUSC). We utilized xCell and TIMER to estimate the gene expression signature of *CXCL9, CXCL10 and CXCR3* and various immune cell populations based on gene expression levels[57,58]. First, we identified strong Spearman correlation with high significance between *CXCL9*, *CXCL10* and *CXCR3* in LUAD (**Fig 1a**). The strong correlation between the components of the CXCL9/10 and CXCR3 axis also extends to LUSC (**Fig S1a**).

Given the strong associations between *CXCL9*, *CXCL10* and *CXCR3*, we then examined potential associations of CXCL9 as a surrogate for the various cell types in the tumor microenvironment. When compared to tumor content/purity, CXCL9 has a weak negative correlation coefficient in both LUAD and LUSC suggesting no association (**Fig 1b, Fig S1b**). However, there is a strong correlation in both T cell subtypes with a preference for $CD8^+$ T cells followed by the Th2 subtype of $CD4^+$ T cells (**Fig 1b, Fig S1b**). Though correlation does not necessarily demonstrate causation, this data suggests that the presence of a strong CXCL9/10 signature can have a higher T cell signature. This further confirms that CXCL9 and CXCL10 can potentially facilitate the recruitment of T cells into the tumor microenvironment[50,51]. Dendritic cells and macrophages have been shown to be the main cell type secreting CXCL9 and CXCL10[50,51]. Thus, the gene signatures of these cell types were investigated with *CXCL9*. There was weak to no correlation between *CXCL9* and dendritic cells (**Fig 1c, Fig S1c**). However, when an activated dendritic cell signature was analyzed, there was a strong correlation with *CXCL9* in both LUAD and LUSC. Furthermore, a positive correlation was also detected with macrophages, specifically, M1 type macrophages, in both subtypes of NSCLC (**Fig 1c, Fig S1c**). Conversely, neutrophils, which are not thought to be associated with CXCL9/10 signature, have no correlation (**Fig 1d, Fig S1d**). There was a weak to no correlation found with monocytes, while no correlation was seen with either NK or NKT cell signatures in either LUAD or LUSC (**Fig 1d, Fig S1d**). A stronger correlation with both activated dendritic cells and M1 macrophages suggests that these cells may be responsible for secretion

of CXCL9/10 chemokines and thus, facilitate the recruitment of T cells to promote an anti-tumor immune response.

In situ vaccination with CXCL9/10-DC promotes an anti-tumor immune response in murine models of lung cancer

Chemokines CXCL9 and CXCL10 have been shown to be a strong indicator of an immune response in cancer[27-29,50,51]. *In situ* vaccination of dendritic cells engineered to secrete chemokines have been successful in promoting antigen presentation and inducing an anti-tumor immune response[40,59-62]. Thus, we hypothesize that *in situ* vaccination through intratumoral injection of dendritic cells engineered to secrete CXCL9 and CXCL10 (CXCL9/10-DC) can augment the intrinsic anti-tumor immune response and limit tumor growth. Bone marrow derived MHC $II^{+}CD11c^{+}CD11b^{low}$ dendritic cells were differentiated utilizing GM-CSF and IL-4[40,59,61]. These dendritic cells were then transduced with a lentiviral construct to express CXCL9 or CXCL10 (**Fig S2a**). An equal number of lentivirally transduced CXCL9-DC and CXCL10-DC was used to generate CXCL9/10-DCs that secrete at least 10ng of each cytokine per million cells (**Fig S2b**).

Since CXCL9/10-DC can potentially augment the immune system, we tested the efficacy of intratumoral injection of CXCL9/10-DC in multiple murine models of NSCLC. CXCL9/10-DC significantly reduced tumor growth in a *Kras*-mutant murine model of NSCLC, LKR13 and L1C2 as measured by both tumor volume and tumor weights at the end of study[38,63] (**Fig 2a**, **Fig S2c**). CXCL9/10-DC also mitigated tumor growth in a model of $Kras^{G12D}$ $p53^{-/-}$ when compared to mock-transduced DC alone or PBS control[64] (**Fig 2b**). To further examine the anti-tumor efficacy of CXCL9/10-DC we evaluated this therapy in mice bearing *Kras*-mutant tumors with inactivating mutations of *Lkb1* ($Kras^{G12D}$ $p53^{-/-}$ $Lkb1^{-/-}$-3M or KPL-3M), which has been recently identified as the major genetic driver of primary resistance to immune checkpoint blockade (ICB) in NSCLC[32,33,64]. CXCL9/10-DC significantly reduced tumor growth in *Lkb1*-null tumors when

compared to control, equivalent concentrations of recombinant CXCL9/10 chemokines and mock transduced DC alone (**Fig 2c**). Though CXCL9 and CXCL10 belong to the same family of chemokines, whether their function is truly redundant is still unknown[65]. Various papers have also shown that CXCL9 is the main driver of response while others highlight CXCL10[50,51]. Thus, we examined whether CXCL9-DC vs CXCL10-DC or a combination of CXCL9/10-DC would have greater efficacy in a *Kras Lkb1*-null model. Both CXCL9-DC and CXCL10-DC were equally as potent in anti-tumor efficacy when compared to CXCL9/10-DC, suggesting that in this murine model, either CXCL9 or CXCL10 can drive efficacy (**Fig 2d**). These experiments highlight that CXCL9/10-DC can augment anti-tumor immunity in various murine models of NSCLC and are superior to mock-transduced DC alone. In addition, data suggest that CXCL9 or CXCL10 may be redundant in this model. Consequently, we opted to move forward with a mixture of CXCL9/10-DC for immune phenotyping.

CXCL9/10-DC facilitates T cell recruitment and activation that are required for anti-tumor efficacy

To investigate if CXCL9/10-DC facilitates changes in the tumor immune microenvironment, flow cytometry was performed to examine various immune phenotypes. There was a significant increase of $CD4^+$ T cells in the tumor following CXCL9/10-DC treatment (**Fig 3a**). This was mainly driven by a statistically significant increase in helper $CD4^+FOXP3^-$ T cells as opposed to $CD4^+FOXP3^+$ T regulatory cells (**Fig 3a**). Comparison of the $CD4^+FOXP3^-$ T cell compartment showed a statistically significant decrease of $CD62L^+CD44^-$ naïve cells with a shift to $CD62L^-CD44^+$ effector cells following CXCL9/10-DC treatment (**Fig 3a**). There was no change in central memory phenotype. Further analysis of effector $CD4^+FOXP3^-CD62L^-CD44^+$ T cells revealed an increase in PD-1 staining, marking tumor dependent T cell activation and less exhausted cells marked by $PD\text{-}1^+Tim3^+$ double staining (**Fig 3a**)[66,67]. This leads to the conclusion that treatment with CXCL9/10-DC facilitates an increase in $CD4^+$ T helper cells in the tumor microenvironment

favoring the effector state with less exhaustion markers. To further establish the role of $CD4^+$ T cells in CXCL9/10-DC, we initiated depletion of $CD4^+$ T cells prior to the injection of CXCL9/10-DC until end of study. Removal of $CD4^+$ T cells reversed the efficacy shown by CXCL9/10-DC (**Fig 3b**). To further test the role of early recruitment of $CD4^+$ T cells, we provided 2 loading doses of antibodies that facilitate depletion for the duration of the CXCL9/10-DC treatment (**Fig 3c**). This also reversed efficacy shown by CXCL9/10-DC, highlighting the importance of $CD4^+$ T cells early in the therapy.

In addition to $CD4^+$ T cell changes, there was an increase in $CD8^+$ T cells following CXCL9/10-DC (**Fig 3d**). Similar to $CD4^+$ T cells, there was a shift from naïve to effector state following therapy and a decrease in $PD1^+TIM3^+$ exhausted $CD8^+CD44^+$ T cells (**Fig 3d**). To highlight the importance of CD8+ T cells following CXCL9/10-DC, CD8+ T cell depletion was performed which reversed the anti-tumor efficacy (**Fig 3e**). Other immune phenotypes demonstrate minimal or no change. There was a trend toward increasing NK cells and statistically significant increase of NKT cells following therapy (**Fig S3a**). There were no changes in monocytes, macrophages or total dendritic cells, with a minimal increase in cDC1 dendritic cells (**Fig S3b,c**). There was a trend toward decreasing $Ly6G^+$ $Ly6C^-$ neutrophils with a potential increase of $Ly6G^+$ $Ly6C^+$ neutrophils (**Fig S3d**). Changes were mainly driven by T cells following CXCL9/10-DC therapy.

Spatial analysis of T cell recruitment following CXCL9/10-DC treatment

Though an increase in activated $CD4^+$ and $CD8^+$ T cells was identified, flow cytometry does not reflect the spatial profile of the immune microenvironment. Multiplex immunofluorescence (7-plex) was performed with the following markers: $CD4^+$, $CD8^+$, $FOXP3^+$, Granzyme B, Ki67, PanC/K (tumor marker) and DAPI (nuclear marker) (**Fig 4a**). Representative images of control vs CXCL9/10-DC treated mouse tumors uncovered an increased density of immune activity at the tumor edge following treatment (**Fig 4b**). Quantifying the spatial infiltration of $CD4^+$ T cells, we see

a slight increasing trend in the intra-tumoral regions as early as D14 with a statistically significant increase in the peritumoral regions following CXCL9/10-DC therapy (**Fig 4c**, **Fig S4a**). By D23, we see a statistically significant increase in $CD4^+$ T cells in both intra- and peri- tumoral regions of CXCL9/10-DC treated tumors (**Fig 4c**). Analysis of Ki67 of $CD4^+$ T cells shows a significant increase in the peritumoral space at both timepoints (**Fig 4c**). Though we see an increase in the $FOXP3^+$ $CD4^+$ T cells following CXCL9/10-DC treatment, the actual composition of $FOXP3^+$ $CD4^+$ T cells are similar at D14 between control and CXCL9/10-DC, suggesting that the increase in total $CD4^+$ T cells may be mainly driven by an increase in effector cells (**Fig 4c**, **Fig S4b**). There is an increase $FOXP3^+$ $CD4^+$ T regulatory cells at D23 mainly in the control group suggesting an immunosuppressive T cell response.

Analyzing $CD8^+$ T cells, we see no changes in T cell infiltration in the intratumoral space at D14 (**Fig 4d**). There is, however, a significant increase in the peritumoral space (**Fig 4d**). At D23, we see a continued increase in $CD8^+$ T cells in the peritumoral space with statistically significant increases also found at the -200 to 0 intratumoral region (**Fig 4d**). When we analyzed the Granzyme B secretion of these $CD8^+$ T cells, we see the largest difference in the peritumoral space, consistent with the increased $CD8^+$ T cells at D14 (**Fig 4d**). By D23, we see an increase in Granzyme B across the entire tumor environment (**Fig 4d**). Proliferation of $CD8^+$ T cells appears to be localized at the peritumoral region as shown by Ki67 staining (**Fig 4d**).

T cell recruitment from lymph nodes is essential for CXCL9/10-DC-mediated efficacy

Spatial analysis demonstrates that the highest density of T cells is found in the tumor border, suggesting active recruitment of T cells into the tumor microenvironment. To better understand the source of the recruited T cells, tumor draining lymph nodes of control and CXCL9/10-DC treated mice were analyzed. No statistically significant difference in the number of $CD4^+$ T cells was found, although there is a decrease in $CD8^+$ T cells which suggests T cell migration from the

lymph node (**Fig 5a**). Analyzing the proliferative capacity of the T cells in the lymph node, we see a statistically significant increase in $Ki67^+$ staining for both $CD4^+$ and $CD8^+$ T cells following treatment with CXCL9/10-DC (**Fig 5a**). Further examining the T cell recruitment-related chemokine axis, we found an increase in CXCR3 expression of the T cells in the tumor draining lymph.

To test if this increased proliferation of T cells is then recruited to the tumor microenvironment, fingolimod, a sphingosine 1-phosphate inhibitor, was utilized to block T cell egress from the lymph node. There was no change in control tumors treated with or without fingolimod (**Fig 5b**). However, we see complete eradication of CXCL9/10-DC efficacy following combination treatment with fingolimod (**Fig 5b**). This suggests that activated T cells from the lymph node are recruited into the tumor microenvironment following CXCL9/10-DC treatment. To further ascertain whether the CXCL9/10-CXCR3 axis is the main chemokine gradient responsible for T cell recruitment, a CXCR3 depleting antibody was used to block the recruitment of $CXCR3^+$ T cells to the CXCL9/10 gradient in the tumor. There is a slight increase tumor growth following CXCR3 blockade in the control tumors when compared to PBS alone (**Fig 5c**). CXCR3 depletion, however, reversed anti-tumor efficacy of CXCL9/10-DC treated tumors suggesting the dependency on the CXCR3 axis to recruit T cells into the tumor space.

CXCL9/10-DC potentiates ICB immunotherapy in murine models of NSCLC

Though checkpoint blockade has become the first line treatment for non-EGFR non-ALK driven NSCLC, the majority of patients do not respond to ICB monotherapy (primary resistance) and others relapse after an initial response (acquired resistance)[11-13]. To determine if CXCL9/10-DC can potentiate anti-PD-1 response in KPL tumors, combination therapy was tested in a *Kras*^{G12D} *p53*$^{-/-}$ *LKB1*$^{-/-}$ model of NSCLC. We identified robust tumor growth in PBS treated tumors, followed by partial efficacy following anti-PD-1 treatment (**Fig 6a**). In addition, CXCL9/10-DC also partially

attenuated tumor growth (**Fig 6a**). When in combination, we see a robust reduction of tumor growth around D14 that is followed by tumor regression which leads to complete tumor reduction in roughly 30% of tumors as measured by both tumor volume and tumor weights (**Fig 6a**). In addition to reduced tumor size following combination therapy, immunofluorescent staining of PanC/K to measure tumor density showed significantly reduced tumor content and increased stroma area (**Fig S6a**). CXCL9/10-DC was also found to potentiate PD-L1 and enhance the efficacy of single-arm anti-PD-L1 (**Fig 6b**). In addition, CXCL9-DC or CXCL10-DC can potentiate anti-PD-1 therapy similarly to the combination of CXCL9/10-DC (**Fig S6b**).

CXCL9/10-DC in combination with anti-PD-1 facilitated the highest increase of $CD4^+$ T cells when compared to control at D16 which was maintained up to D19 (**Fig 6c**). Further analysis of $CD4^+$ T cells at D16 demonstrated an increase in $CD4^+$ $FOXP3^-$ T helper cells following CXCL9/10-DC therapy when compared to control or anti-PD-1 alone. These T cells also had increased PD-1 staining suggestive of tumor recognition and activation while exhibiting a decreased exhausted state as indicated by $PD1^+TIM3^+$ double stain (**Fig 6c**). $CD8^+$ T cells had an increasing trend from D16 to D19 following CXCL9/10-DC treatment with minimal changes in PD1 status or exhaustion state (**Fig 6d**). There does seem to be a slight increase in $PD1^+$ cells following CXCL9/10-DC monotherapy (**Fig 6d**).

CXCL9/10-DC and anti-PD-1 combination treatment generates systemic immunity against tumor rechallenge

To assess the effect of intratumoral administration of CXCL9/10-DC on systemic immune changes, flow cytometry was performed with the spleens harvested from the same 4-arm mouse experiments. Following CXCL9/10-DC, there was a decrease in the naïve compartment of $CD4^+$ T cells which coincides with a statistically significant increase in central memory cells as labeled by $CD44^+$ $CD62L^+$ stain (**Fig 7a**). An increase in CD4 $PD1^+$ T cells and interferon gamma (IFNg)

staining was also discovered suggesting more activation (**Fig 7a**). In the $CD8^+$ T cell population, we see a similar response of decreased naïve cells and increased central memory cells (**Fig 7a**). Similar to $CD4^+$ T cells, we see statistically significant PD-1 upregulation with increased IFNg signature in $CD8^+$ effector T cells (**Fig 7a**). These data suggest a shift in the activation of splenocytic T cells and the formation of central memory cells.

To study if this increase in central memory and activated cells can lead to systemic immunity, a rechallenge experiment was performed on cured mice. Two months following successful tumor eradication in a subset of CXCL9/10-DC and anti-PD-1 treated mice, double the amount of KPL-3M tumor cells were injected into the opposite flank (**Fig 7b**). Age-matched naïve mice were injected as experimental controls. Successful tumor establishment was verified by tumor growth initiation as early as D2 using the IVIS Spectrum *in vivo* imaging modality to visualize the tumor's luciferase reporter (**Fig 7b**). Tumor growth continues to increase at D4 but decreases by D7 (**Fig 7b**). Most of the tumors were rejected by D10 but one tumor remained, which was eventually eradicated by D14; conversely, the aged-matched naïve mice succumbed to the tumor in approximately 30 days (**Fig 7b-7c**). This suggests that we have successfully initiated systemic tumor immunity in CXCL9/10-DC + anti-PD-1 cured mice. To confirm tumor specificity, these mice were rechallenged with a syngeneic tumor cell line, MyCAP. Both naïve and cured mice succumbed to the MyCAP tumor (**Fig 7c**).

Discussion

In multiple murine models of NSCLC, CXCL9/10-DC successfully promotes an anti-tumor response through recruitment and activation of effector T cells. Depletion studies highlight the importance of both $CD4^+$ and $CD8^+$ T cells. Successful trafficking from the tumor draining lymph node and chemotaxis of these cells utilizing the CXCR3 axis was shown to drive the response. CXCL9/10-DC also potentiated ICB therapy in a translational pre-clinical KPL-3M model of lung

cancer which can have potential clinical implications. In addition, tumor eradication following combination therapy leads to systemic immunity that provides insight into potential dendritic cell vaccination therapy.

TCGA data of the CXCL9/10-CXCR3 axis signature suggests multiple interactions with various immune cells. Here, we identify high expression correlating with activated dendritic cells and M1 type macrophages suggesting the secretion of these chemokines following anti-tumor activation[50,51]. This also correlates to a higher T cell signature, however, as we see in Fig 1b, not all tumors have T cell infiltration. Thus, not all high CXCL9/10 gene expression correlates with successful immune activation[68,69]. This can be due to a lack of antigen presentation, the presence of immunosuppressive factors or inadequate signal to recruit activated T cells[68,70]. Alternatively, one potential caveat is the early collection methods of TCGA samples focusing on high tumor content thus, not accurately representing the immune cells in the tumor microenvironment[71]. Though TCGA provides some insight into the importance of the CXCL9/10-CXCR3 axis in lung cancer, follow-up experiments are required to account for other determinants of an immune response in the tumor microenvironment especially with a focus on genetic drivers and tumor heterogeneity.

CXCL9/10-DC can successfully intervene against cancer in various mouse models of NSCLC by promoting a T cell response. This therapy successfully increased the recruitment and activation of various T cells in the microenvironment. Increased effector state and PD-1 activation suggests engagement with tumor cells that are reflected by the decrease in tumor growth[67,72,73]. Spatial analysis of the KPL-3M tumor model demonstrated dense tumor growth with a leading tumor edge, accurately representing previous findings of an immunosuppressive environment devoid of T cells[31-33,74]. Regardless, CXCL9/10-DC therapy successfully led to the increased recruitment of T cells to the tumor environment. Specific activation of $CD8^+$ granzyme B^+ T cells potentially

contributed to tumor burden reduction while activated $CD4^+$ T cells were prevalent across multiple tumor regions. In-depth subtyping of these $CD4^+$ T cells using single cell RNA-seq (data not shown) suggests a preference for a Th2 response. This coincides with the TCGA data suggesting a stronger correlation with Th2 $CD4^+$ T cells suggests. Further studies will investigate the prominent role of $CD4^+$ T cells in the immune and therapeutic response. Direct inhibition of tumor growth or indirect activation of other anti-tumor immune cell types are potential components of the $CD4^+$ T cell response[75,76].

It was also demonstrated that CXCL9/10-DC therapy is dependent on recruitment from tumor draining lymph nodes, highlighting the importance of the chemokine gradient for a successful immune response. As previously shown, intratumoral dendritic cell injection persists only for a few days; thus, we hypothesize that the therapy initially recruits tumor-specific activated T cells, which then potentially secrete interferon gamma and “jump start” the immune recognition of the tumor[59]. Though the injected cells only persisted for a few days (data not shown), they were able to promote a long-lasting anti-tumor response that eventually overwhelmed tumor growth.

Previous studies have highlighted the role and importance of checkpoint inhibition in maintaining a successful T cell immune response[19,20,22,24]. CXCL9/10-DC monotherapy, though successful in recruiting activated T cells, still leaves tumors susceptible to checkpoint inhibition. This is confirmed in Figure 6, where successful combination of both CXCL9/10-DC and anti-PD-1/PD-L1 therapy is displayed. T cells recruited from CXCL9/10-DC benefit from checkpoint blockade, leading to an improved and prolonged anti-tumor response. Simultaneously, checkpoint blockade benefits from the increased recruitment of T cells that were previously suppressed by PD-1/PD-L1 interaction. This is highlighted by the 30% cures found in mice that received combination therapy. On the other hand, not all mice respond to combination treatment, necessitating investigation into whether tumor heterogeneity and clonal evolution can provide some insight into

mechanisms of escape[77,78]. In addition, though there was an increase in recruited T cells and activation status, not all recruited T cells expressed activation markers, suggesting the recruitment of bystander T cells as well[41,79].

Successful treatment, however, led to complete tumor eradication and persistent systemic immunity. Through multiple rechallenges, the mice were able to successfully reject KPL-3M, suggesting that systemic immunity to mutated tumor proteins can be generated. Though this has been displayed in a pre-clinical model, it provides a positive outlook for dendritic cell vaccination strategies that can potentially impact patients with relapsed disease following initial response to therapeutic treatments for NSCLC.

CHAPTER 1 - FIGURE 1

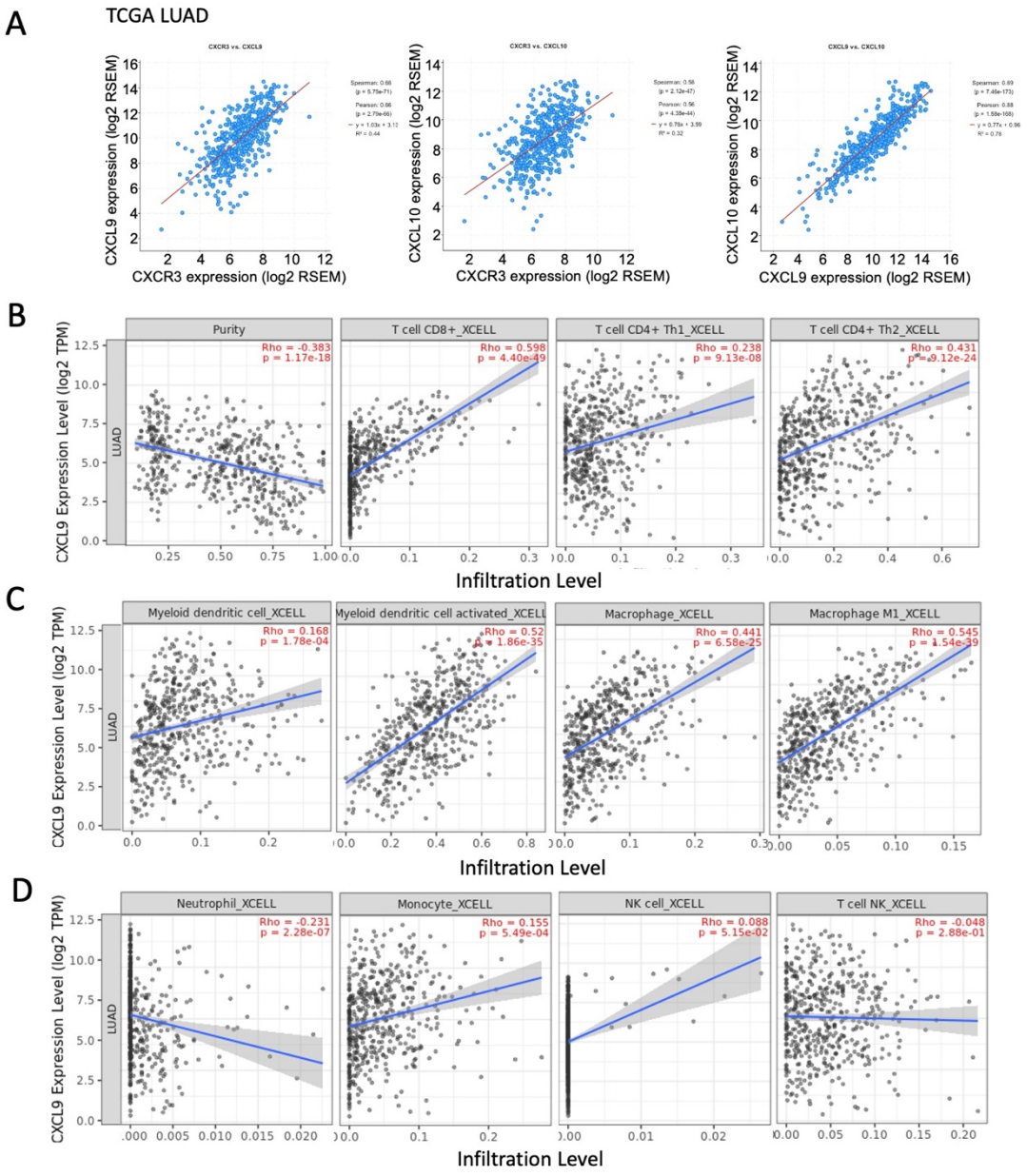

FIGURE 1

CXCL9/10 and CXCR3 axis correlation with immune cells in human LUAD

Spearman correlations between CXCL9, CXCL10, CXCR3 expression levels and immune infiltration in the TCGA database of LUAD using xCell expression signatures. **A)** CXCL9, CXCL10 and CXCR3 expression levels plotted against each other to demonstrate significant correlations. **B)** $CD8^+$ T cells and both $CD4^+$ Th1 and Th2 T cells, but not tumor content, demonstrated significant correlations with CXCL9 levels. **C)** CXCL9 gene expression levels showed no correlation with dendritic cells but significant correlation with activated dendritic cells, total macrophages and M1 subtype macrophages. **D)** Weak or no correlations were found with neutrophils, monocytes, NK and NK T cells.

CHAPTER 1 - SUPPLEMENTAL FIGURE 1

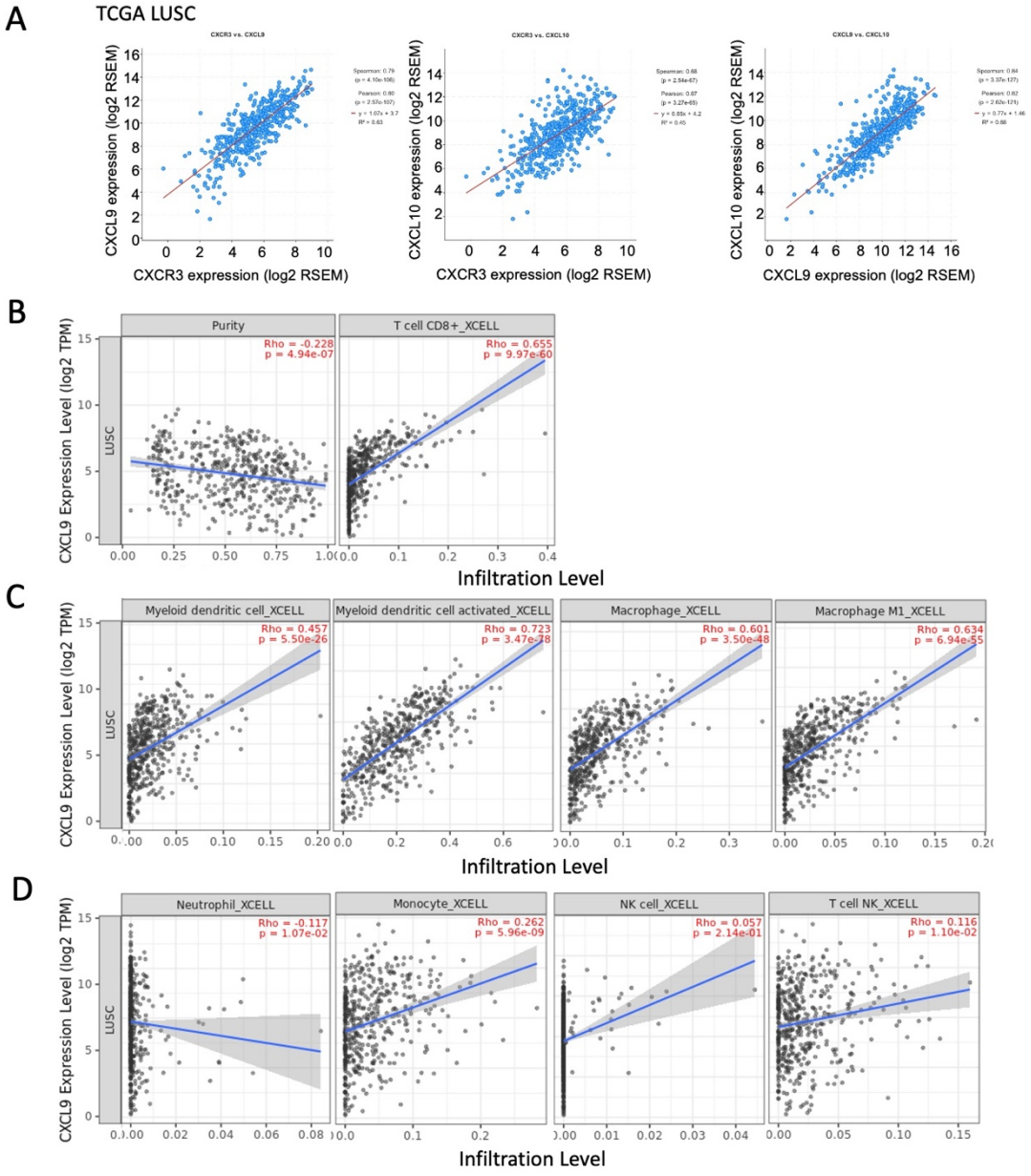

SUPPLEMENTAL FIGURE 1

CXCL9/10 and CXCR3 axis correlation with immune cells in human LUSC

Spearman correlations between CXCL9, CXCL10, CXCR3 expression levels and immune infiltration in the TCGA database of LUSC using xCell expression signatures. **A)** CXCL9, CXCL10 and CXCR3 expression levels were plotted against each other to demonstrate significant correlations. **B)** Similar to LUAD, $CD8^+$ T cells, but not tumor content, showed significant correlation with CXCL9 levels. **C)** CXCL9 gene expression levels showed weak correlation with dendritic cells but stronger correlation with activated dendritic cells, total macrophages and M1 subtype macrophages. **D)** Weak or no correlations were found with neutrophils, monocytes, NK and NK T cells.

CHAPTER 1 - FIGURE 2

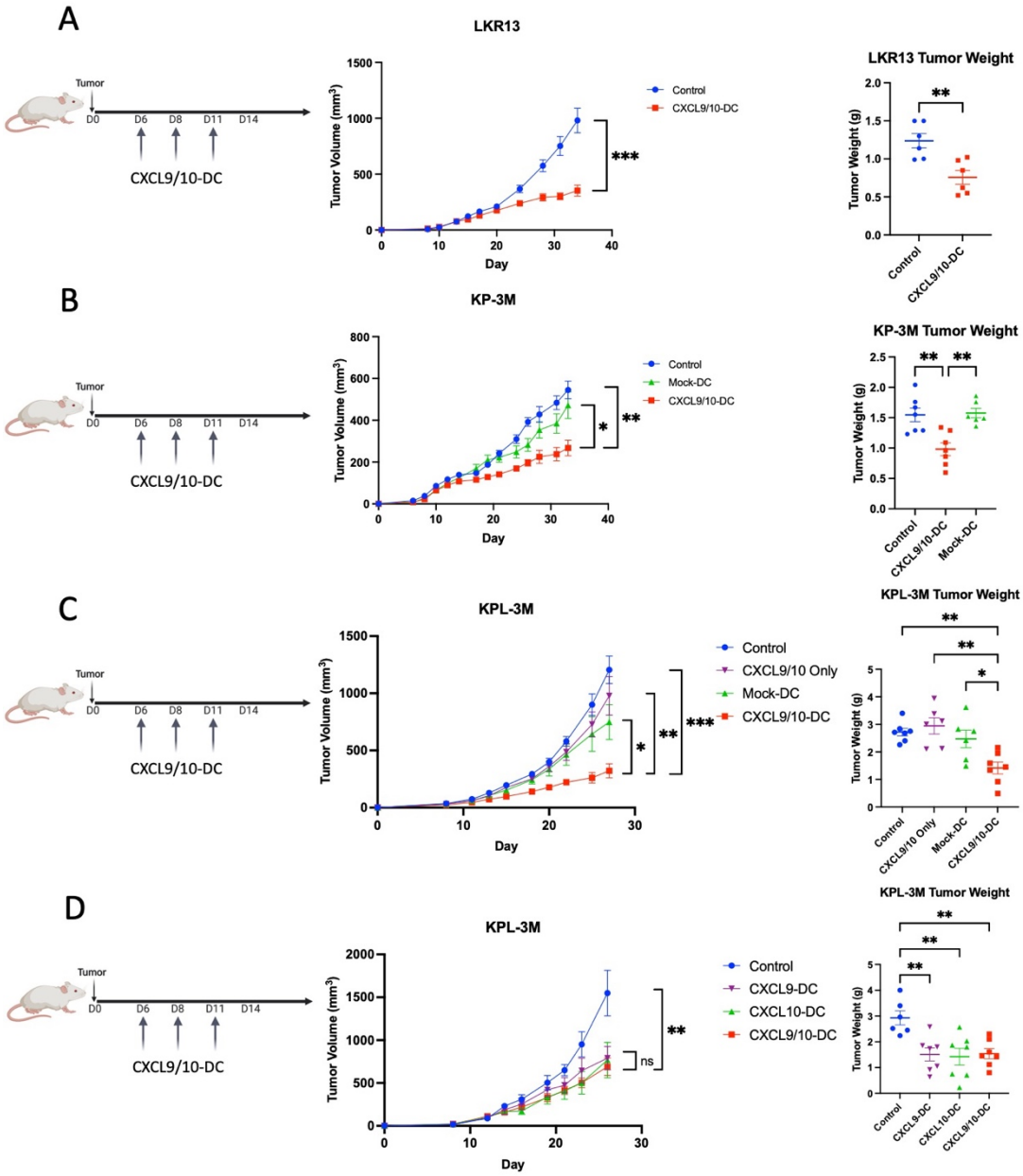

FIGURE 2

***In situ* vaccination with CXCL9/10-DC promotes an anti-tumor response in murine models of lung cancer**

Study design of *in vivo* mouse models of NSCLC. **A)** On D6 post tumor inoculation ($1.0x10^6$ LKR13 tumor cells delivered SC), 129-E mice bearing ~$50mm^3$ tumors were treated with i) vehicle, ii) $2.0x10^6$ CXCL9/10-DC for a total of 3 injections at D6, D8 and D11. **B)** On D6 post tumor inoculation ($2.0x10^6$ *Kras*^{G12D}*p53*$^{-/-}$-3M tumor cells delivered SC), FVB/NCrl mice bearing ~$50mm^3$ tumors were treated with i) vehicle, ii) $2.0x10^6$ mock transduced DC for a total of 3 injections at D6, D8 and D11, iii) $2.0x10^6$ CXCL9/10-DC for a total of 3 injections at the same time point. **C)** On D6 post tumor inoculation ($1.25x10^5$ *Kras*^{G12D}*p53*$^{-/-}$*Lkb1*$^{-/1}$-3M or KPL-3M tumor cells delivered SC), FVB/NCrl mice bearing ~$50mm^3$ tumors were treated with i) vehicle, ii) CXCL9 and CXCL10 recombinant protein at 20ng each for a total of 3 injections at D6, D8 and D11, iii) $2.0x10^6$ mock transduced DC for a total of 3 injections at the same time points, iv) $2.0x10^6$ CXCL9/10-DC for a total of 3 injections at the same time points. **D)** On D6 post tumor inoculation ($1.25x10^5$ KPL-3M tumor cells delivered SC), FVB/NCrl mice bearing ~$50mm^3$ tumors were treated with i) vehicle, ii) $2.0x10^6$ CXCL9-DC for a total of 3 injections at D6, D8 and D11, iii) $2.0x10^6$ CXCL10-DC with similar time points and iv) $2.0x10^6$ CXCL9/10-DC at the same time points. Tumor volumes were recorded every 2-3 days and tumor weights on the day of euthanasia were collected. *P* values were determined by unpaired *t*-test. n.s., not significant; *, $P<0.05$; **, $P< 0.005$, ***, $P< 0.0005$, ****, $P< 0.00005$

CHAPTER 1 - SUPPLEMENTAL FIGURE 2

A

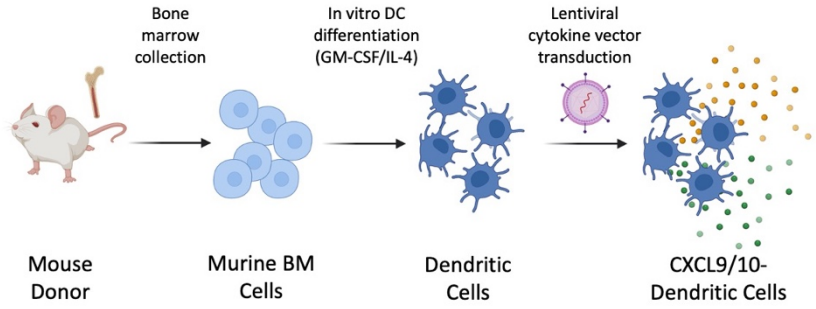

B

DC transduced with CXCL9 lentivirus	(ng/million cells) 24 Hours
DC Vector Only (48 Hour Collection)	BLQ
CXCL9-DC Batch I (48 Hour Collection)	28.02
CXCL9-DC Batch II (60 Hour Collection)	27.72
CXCL9-DC Batch III (72 Hour Collection)	30.40

DC transduced with CXCL10 lentivirus	(ng/million cells) 24 Hours
DC Vector Only (48 Hour Collection)	BLQ
CXCL10-DC Batch I (48 Hour Collection)	35.09
CXCL10-DC Batch II (60 Hour Collection)	33.63
CXCL10-DC Batch III (72 Hour Collection)	32.12

C

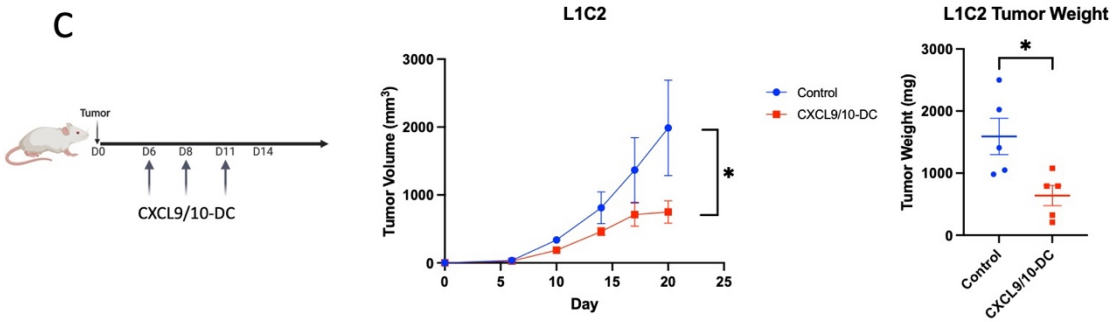

SUPPLEMENTAL FIGURE 2

Generation of CXCL9/10-DC and other models of NSCLC

A) Cartoon schematic of bone marrow collection from donor mice. Differentiation into dendritic cells utilizing GM-CSF/IL-4 followed by lentiviral transduction to generate CXCL9/10-DC. **B)** ELISA measurements of CXCL9 or CXCL10 protein 24 hours after lentiviral transduction. Multiple viral collection time points generate equivalent viral potency. **C)** On D6 post tumor inoculation ($1.0x10^6$ L1C2 tumor cells delivered SC), Balb/c mice bearing ~$50mm^3$ tumors were treated with i) vehicle, ii) $2.0x10^6$ CXCL9/10-DC for a total of 3 injections at D6, D8 and D11. Tumor volumes were recorded every 2-3 days and tumor weights on the day of euthanasia were collected. *P* values were determined by unpaired *t*-test. n.s., not significant; *, $P<0.05$; **, $P< 0.005$, ***, $P< 0.0005$, ****, $P< 0.00005$

CHAPTER 1 - FIGURE 3

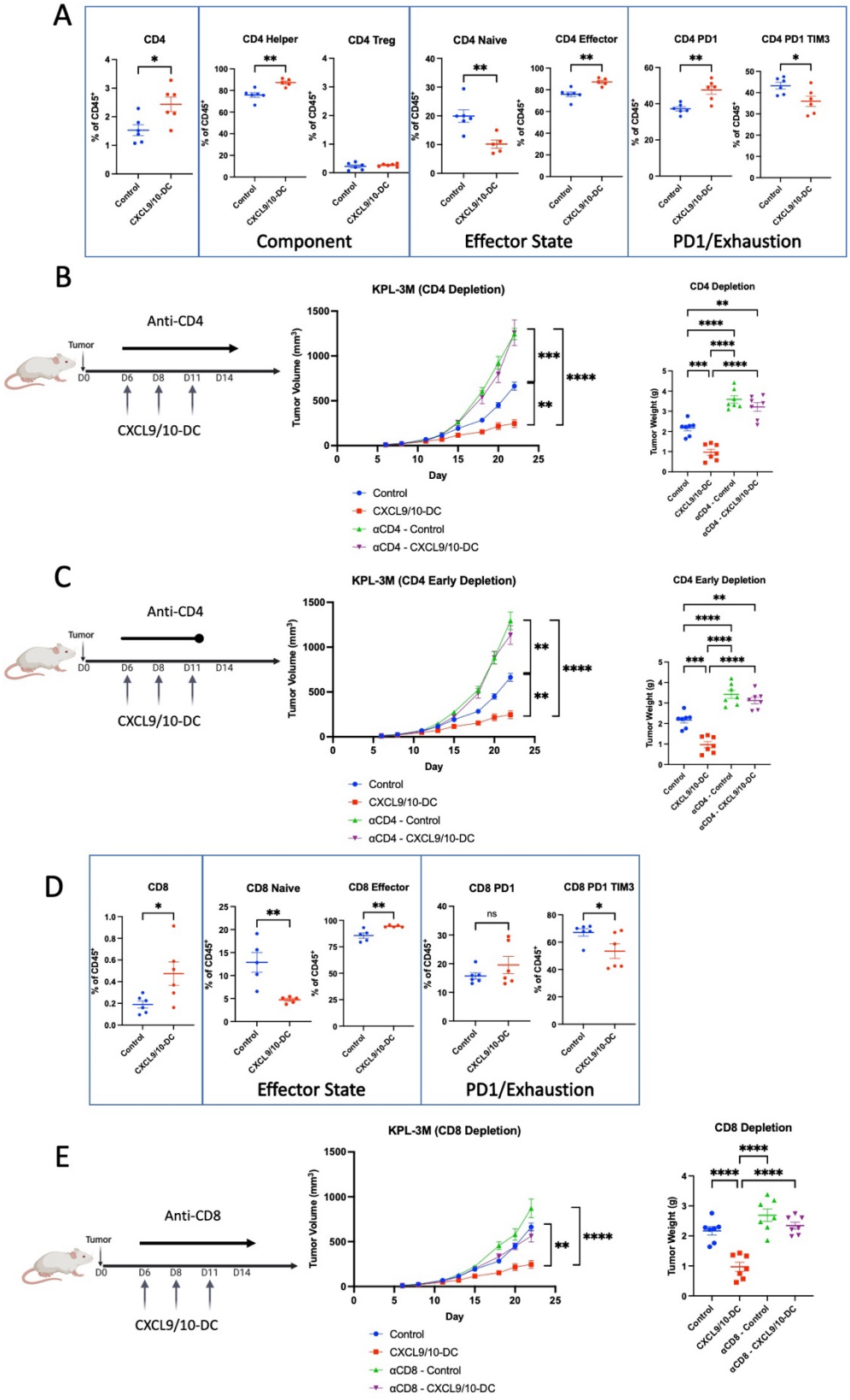

FIGURE 3

CXCL9/10-DC facilitates T cell recruitment and activation that are required for anti-tumor efficacy

Study design for flow phenotyping and *in vivo* mouse models. **A)** Tumors were collected on D14 post inoculation ($1.25x10^5$ KPL-3M delivered SC) following treatment with vehicle control or $2.0x10^6$ CXCL9/10-DC for a total of 3 injections. Flow cytometry was performed to assess $CD4^+$ T cell subtypes and phenotype in the tumor microenvironment (TME). Significant increase in $CD4^+$ T cells following CXCL9/10-DC therapy primarily driven by helper T cells as defined by $CD4^+FOXP3^-$ staining. No changes in $CD4^+FOXP3^+$ T regulatory cells. Significant increase in $CD44^+CD62L^-$ effector states coinciding with a decrease in $CD44^-CD62L^+$ naïve state. Increase in $CD4^+PD1^+$ T cells and decrease of $CD4^+PD1^+TIM3^+$ T cells when compared to control. **B)** On D6 post tumor inoculation ($1.25x10^5$ KPL-3M delivered SC), FVB mice bearing ~$50mm^3$ tumors were treated with i) vehicle, ii) $2.0x10^6$ CXCL9/10-DC for a total of 3 injections, iii) vehicle with IP dose of anti-mouse CD4 every two days, iv) CXCL9/10-DC with anti-mouse CD4 every two days. CD4 depletion reverses CXCL9/10-DC therapy in both tumor volume and weights. **C)** On D6 post tumor inoculation ($1.25x10^5$ KPL-3M delivered SC), FVB mice bearing ~$50mm^3$ tumors were treated with i) vehicle, ii) $2.0x10^6$ CXCL9/10-DC for a total of 3 injections, iii) vehicle with IP dose of anti-mouse CD4 at D6 and D7 only, iv) CXCL9/10-DC with two doses of anti-mouse CD4. Early CD4 depletion reverses CXCL9/10-DC therapy in both tumor volume and weights. **D)** Flow cytometry was performed to assess $CD8^+$ T cell subtypes and phenotype in the TME. Significant increase in $CD8^+$ T cells following CXCL9/10-DC therapy with significant increase in $CD44^+CD62L^-$ effector states coinciding with a decrease in $CD44^-CD62L^+$ naïve state. No changes in $CD4^+PD1^+$ T cells and decrease of $CD4^+PD1^+TIM3^+$ T cells when compared to control. **E)** On D6 post tumor inoculation ($1.25x10^5$ KPL-3M delivered SC), FVB mice bearing ~$50mm^3$ tumors were treated with i) vehicle, ii) $2.0x10^6$ CXCL9/10-DC for a total of 3 injections, iii) vehicle with IP dose of anti-mouse CD8 every two days, iv) CXCL9/10-DC with anti-mouse CD8 every

two days. CD8 depletion reverses CXCL9/10-DC therapy in both tumor volume and weights. *P* values were determined by one-way ANOVA, adjusting for multiple comparisons. *, $P<0.05$; **, $P< 0.005$, ***, $P< 0.0005$, ****, $P< 0.00005$

CHAPTER 1 - SUPPLEMENTAL FIGURE 3

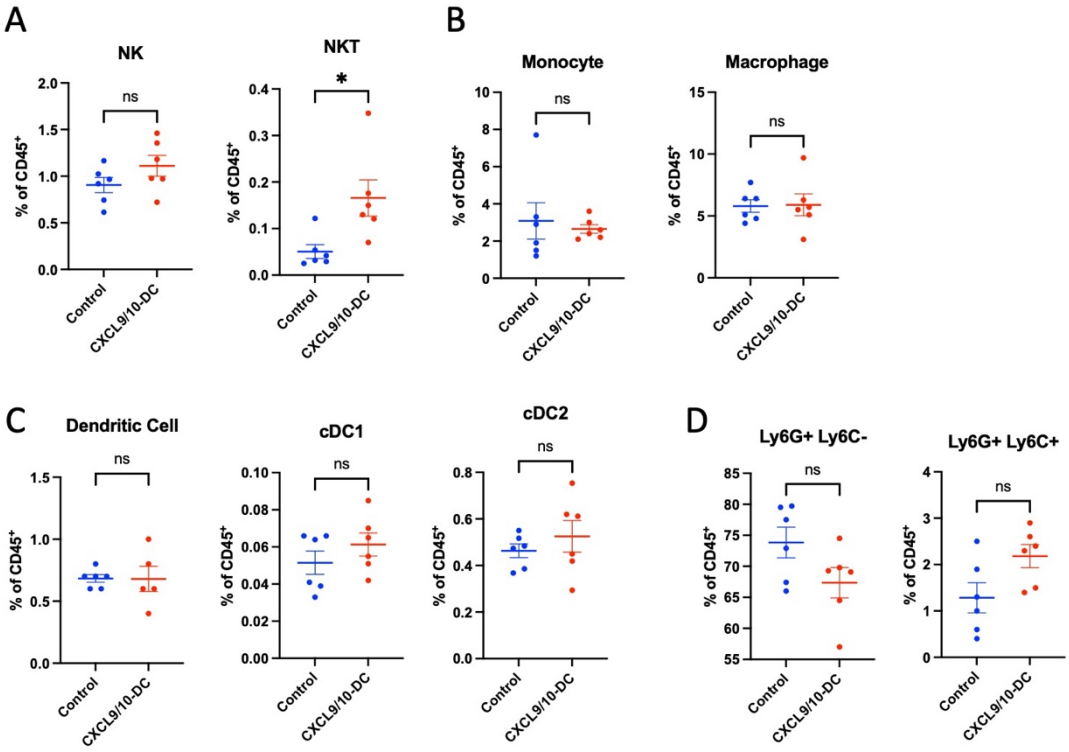

SUPPLEMENTAL FIGURE 3

Other immune cell populations following CXCL9/10-DC therapy

Study design for flow phenotyping. Tumors were collected on D14 post inoculation ($1.25x10^5$ KPL-3M delivered SC) following treatment with vehicle control or $2.0x10^6$ CXCL9/10-DC for a total of 3 injections. Flow cytometry was performed to assess various immune subtypes. **A)** NK ($CD45^+CD49b^+$) has an increasing trend while NKT ($CD45^+CD3^+CD49b^+$) cells demonstrate an increase. **B)** No changes in monocytes ($CD45^+MHCII^{hi}Ly6C^+$) or macrophages ($CD45^+MHCII^{hi}CD64^+$). **C)** No changes in total dendritic cells ($CD45^+MHCII^{hi}CD11c^+$) with minor increasing trends in both cDC1($CD45^+MHCII^{hi}CD11c^+XCR1^+$) and cDC2 ($CD45^+MHCII^{hi}CD11c^+SIRPa^+$) subtypes. **D)** Decreasing trend in $Ly6G^+Ly6C^-$ myeloid cells with increasing trends in $Ly6G^+Ly6C^+$ myeloid cells. *P* values were determined by unpaired *t*-test. n.s., not significant; *, $P<0.05$; **, $P< 0.005$, ***, $P< 0.0005$, ****, $P< 0.00005$

CHAPTER 1 - FIGURE 4

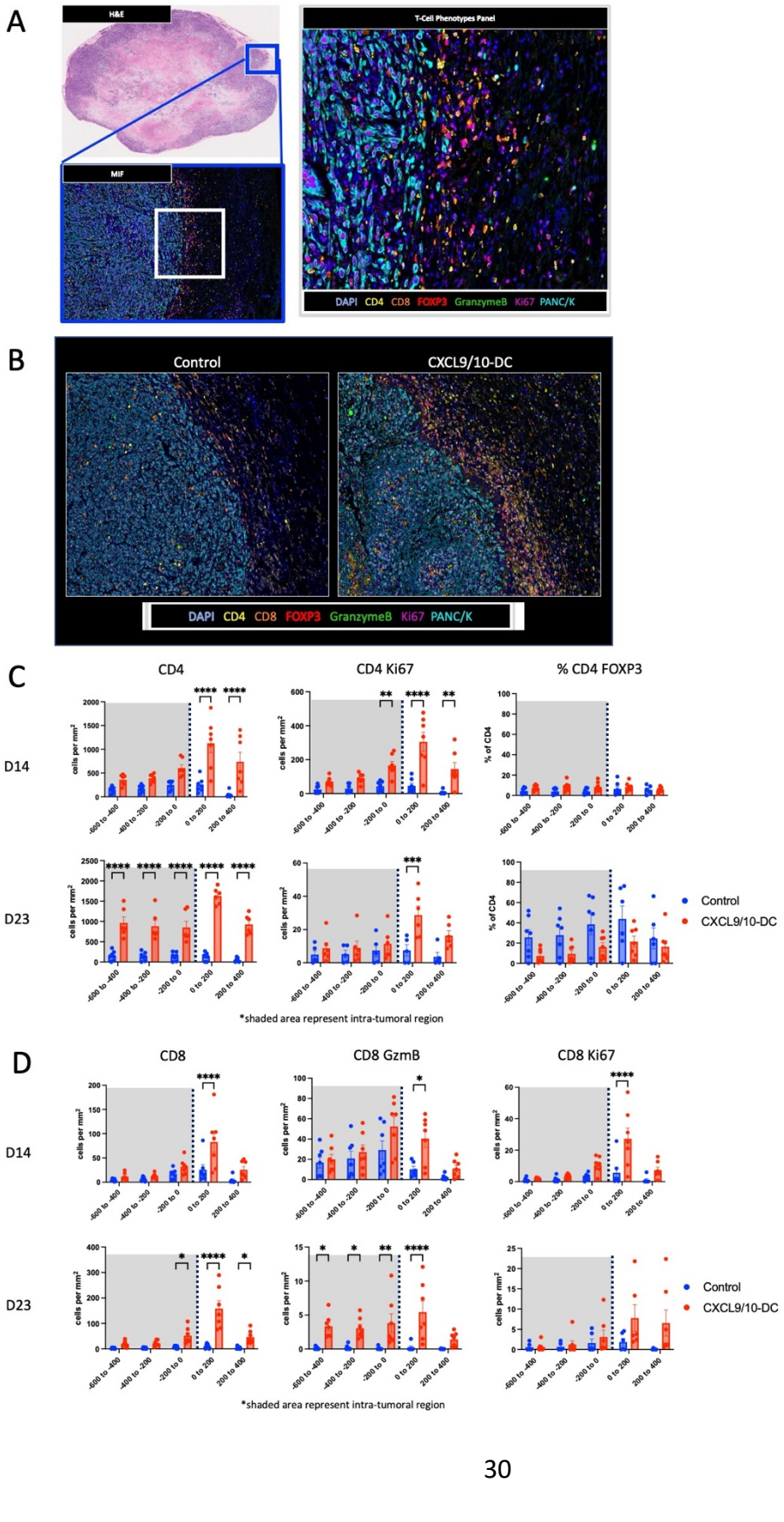

FIGURE 4

Spatial analysis of T cell recruitment following CXCL9/10-DC treatment

Study design for spatial phenotyping. Tumors were collected on D14 and D23 post inoculation ($1.25x10^5$ KPL-3M delivered SC) following treatment with vehicle control or $2.0x10^6$ CXCL9/10-DC and tissues were embedded for staining. **A)** Multiplex immunofluorescence (7-plex: CD4, CD8, Granzyme B, FOXP3, Ki67, PanC/K and DAPI) was performed on tumor sections to investigate the localization of various T-cell phenotypes. **B)** Representative images of control and CXCL9/10-DC tumors. **C)** There was an increase in $CD4^+$ T cells at the peritumoral space at D14 that increased across the tumor microenvironment by D23. $CD4^+$ T cell proliferation was mostly colocalized in the peritumoral space. No changes were identified in $CD4^+FOXP3^+$ T regulatory cells, with a slight increasing trend in the control group at D23. **D)** Increases in the $CD8^+$ T cell compartment were localized in the peritumoral space with increasing differences at D23. Granzyme B activation was primarily localized at the peritumoral space at D14 that persisted in the intratumoral space by D23. Proliferation as defined by $Ki67^+$ was localized in the peritumoral space. *P* values were determined by one-way ANOVA, adjusting for multiple comparisons. n.s., not significant; *, $P<0.05$; **, $P< 0.005$, ***, $P< 0.0005$, ****, $P< 0.00005$

CHAPTER 1 - SUPPLEMENTAL FIGURE 4

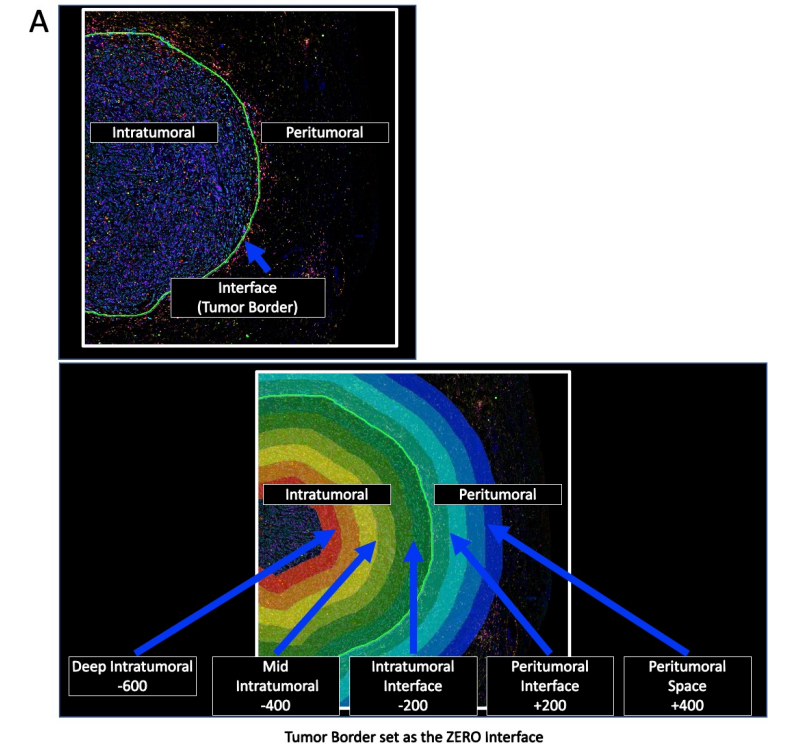

SUPPLEMENTAL FIGURE 4

Methods of spatial analysis and regulatory T cell recruitment following CXCL9/10-DC treatment

Study design for spatial phenotyping. Tumors were collected on D14 and D23 post inoculation ($1.25x10^5$ KPL-3M delivered SC) following treatment with vehicle control or $2.0x10^6$ CXCL9/10-DC and tissues were embedded for staining. **A)** Spatial infiltration at 200μm intervals was performed in relation to the tumor border (labeled interface) and corresponding neighboring regions (labeled intratumoral and peritumoral). **B)** Increase and proliferation of regulatory $CD4^+$ T cells in the peritumoral space following CXCL9/10-DC treatment. Decreasing trend of tumor cells across the intratumoral space following CXCL9/10-DC treatment. *P* values were determined by one-way ANOVA, adjusting for multiple comparisons. n.s., not significant; *, $P<0.05$; **, $P< 0.005$, ***, $P< 0.0005$, ****, $P< 0.00005$

CHAPTER 1 - FIGURE 5

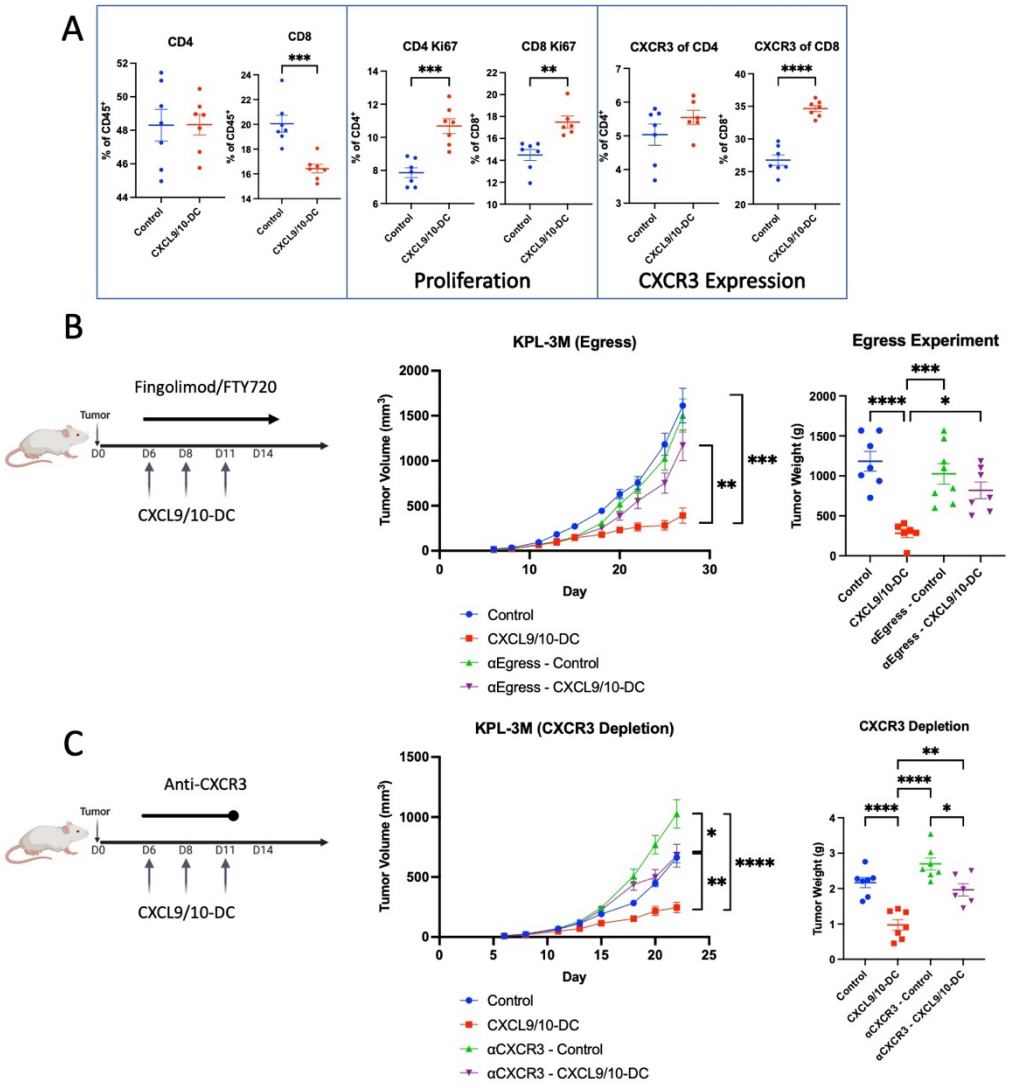

FIGURE 5

T cell recruitment from lymph nodes is essential for CXCL9/10-DC-mediated efficacy

Study design for flow phenotyping and *in vivo* mouse models. **A)** Tumor draining lymph nodes were collected on D16 post inoculation ($1.25x10^5$ KPL-3M delivered SC) following treatment with vehicle control or $2.0x10^6$ CXCL9/10-DC for a total of 3 injections. Flow cytometry was performed to assess $CD4^+$ and $CD8^+$ T cell subtypes and phenotype in the TME, demonstrating no changes in $CD4^+$ T cells with a decrease in $CD8^+$ T cells; increases in proliferation as defined by $Ki67^+$ of both $CD4^+$ and $CD8^+$ T cells; increasing trend in $CXCR3^+$ expression of $CD4^+$ and increase in $CD8^+$ T cells. **B)** On D6 post tumor inoculation ($1.25x10^5$ KPL-3M delivered SC), FVB mice bearing ~$50mm^3$ tumors were treated with i) vehicle, ii) $2.0x10^6$ CXCL9/10-DC for a total of 3 injections, iii) vehicle with every other day IP dose of 2mg/kg fingolimod, iv) CXCL9/10-DC with fingolimod every other day. Lymph node egress inhibition by fingolimod reverses CXCL9/10-DC therapy in both tumor volume and weights. **C)** On D6 post tumor inoculation ($1.25x10^5$ KPL-3M delivered SC), FVB mice bearing ~$50mm^3$ tumors were treated with i) vehicle, ii) $2.0x10^6$ CXCL9/10-DC for a total of 3 injections, iii) vehicle with IP dose of anti-mouse CXCR3 every two days, iv) CXCL9/10-DC with anti-mouse CXCR3 every two days. CXCR3 depletion reverses CXCL9/10-DC therapy in both tumor volume and weights. *P* values were determined by one-way ANOVA, adjusting for multiple comparisons. *, $P<0.05$; **, $P< 0.005$, ***, $P< 0.0005$, ****, $P< 0.00005$

CHAPTER 1 - FIGURE 6

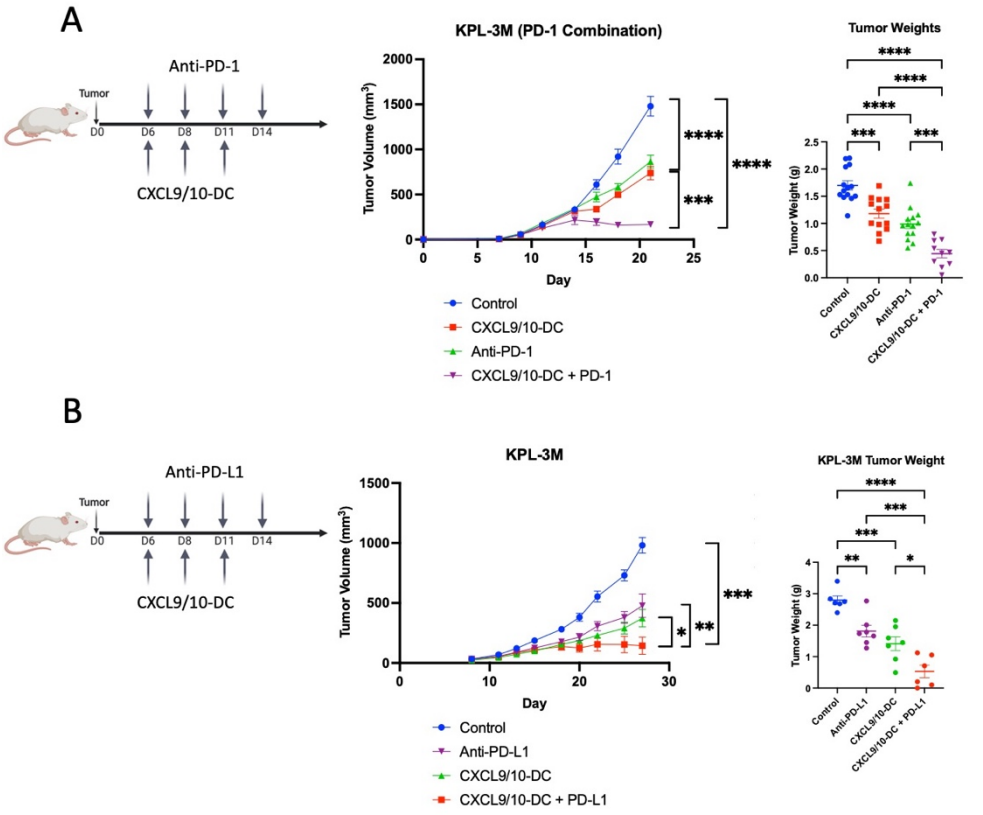

FIGURE 6

CXCL9/10-DC potentiates ICB immunotherapy in murine models of NSCLC

Study design for *in vivo* mouse models and flow phenotyping. **A)** On D6 post tumor inoculation ($1.25x10^5$ KPL-3M delivered SC), FVB mice bearing ~$50mm^3$ tumors were treated with i) vehicle, ii) $2.0x10^6$ CXCL9/10-DC for a total of 3 injections, iii) anti-PD-1 (200µg/dose IP every other day), or iv) combination therapy. Combination therapy was more efficacious than monotherapies as measured by tumor volume and tumor weights. **B)** On D6 post tumor inoculation ($1.25x10^5$ KPL-3M delivered SC), FVB mice bearing ~$50mm^3$ tumors were treated with i) vehicle, ii) $2.0x10^6$ CXCL9/10-DC for a total of 3 injections, iii) anti-PD-L1 (200µg/dose IP every other day), or iv) combination therapy. Similar to anti-PD-1, combination therapy was more efficacious than monotherapies as measured by tumor volume and tumor weights. **C)** Tumors were collected on D16 post inoculation ($1.25x10^5$ KPL-3M delivered SC) following treatment with vehicle control, $2.0x10^6$ CXCL9/10-DC, anti-PD-1 or in combination. Flow cytometry was performed to assess $CD4^+$ T cell subtypes and phenotype in the TME. Significant increase in $CD4^+$ T cells following CXCL9/10-DC therapy at D16 that is maintained until D19. No changes in $CD4^+FOXP3^+$ T regulatory cells with increases primarily driven by helper T cells as defined by $CD4^+FOXP3^-$ staining. Increase in $CD4^+PD1^+$ T cells and decrease of $CD4^+PD1^+TIM3^+$ T cells in both CXCL9/10-DC treated groups. **D)** Flow cytometry was performed to assess $CD8^+$ T cell subtypes and phenotype in the TME. No changes in $CD8^+$ T cells at D16 with increasing trend at D19. There is a slight increase $CD8^+PD1^+$ T cells for CXCL9/10-DC alone and no other major changes across the groups. *P* values were determined by one-way ANOVA, adjusting for multiple comparisons. *, $P<0.05$; **, $P< 0.005$, ***, $P< 0.0005$, ****, $P< 0.00005$

CHAPTER 1 - SUPPLEMENTAL FIGURE 6

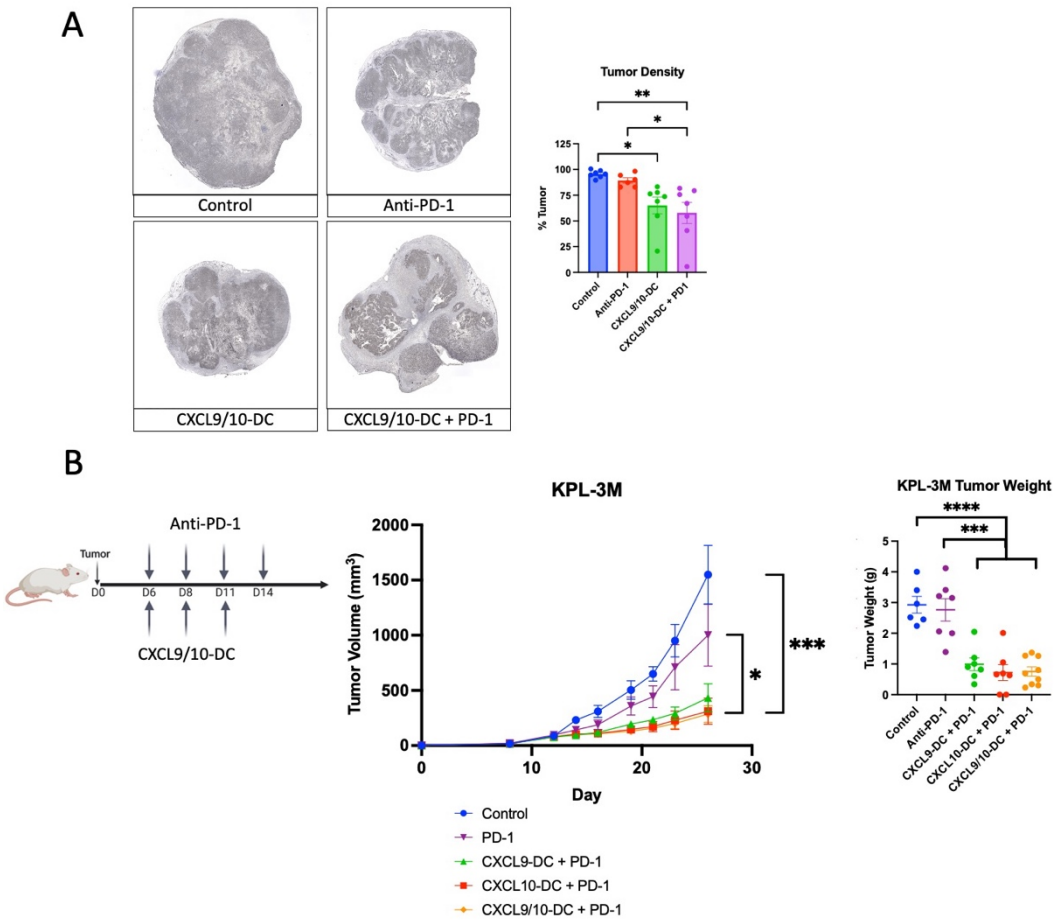

SUPPLEMENTAL FIGURE 6

CXCL9/10-DC potentiates immune checkpoint blockade and tumor density

Study design for spatial phenotyping and *in vivo* mouse models. **A)** Tumors harvested from combination treatment in Fig 6a were collected. Single-plex immunofluorescence using PanC/K was performed on tumor sections to evaluate tumor density. Combination treatment demonstrated significantly reduced tumor density when compared to control and anti-PD-1 treatment. **B)** On D6 post tumor inoculation ($1.25x10^5$ KPL-3M delivered SC), FVB mice bearing ~$50mm^3$ tumors were treated with i) vehicle, ii) anti-PD-1 (200µg/dose IP every other day), iii) $2.0x10^6$ CXCL9-DC for a total of 3 injections in combination with anti-PD-1, iv) $2.0x10^6$ CXCL10-DC in combination with anti-PD-1, or v) $2.0x10^6$ CXCL9/10-DC for a total of 3 injections in combination with anti-PD-1. Tumor volume and weights show equal efficacy of CXCL9-DC, CXCL10-DC, and CXCL9/10-DC in potentiating anti-PD-1 therapy. *P* values were determined by one-way ANOVA, adjusting for multiple comparisons. *, $P<0.05$; **, $P< 0.005$, ***, $P< 0.0005$, ****, $P< 0.00005$

CHAPTER 1 - FIGURE 7

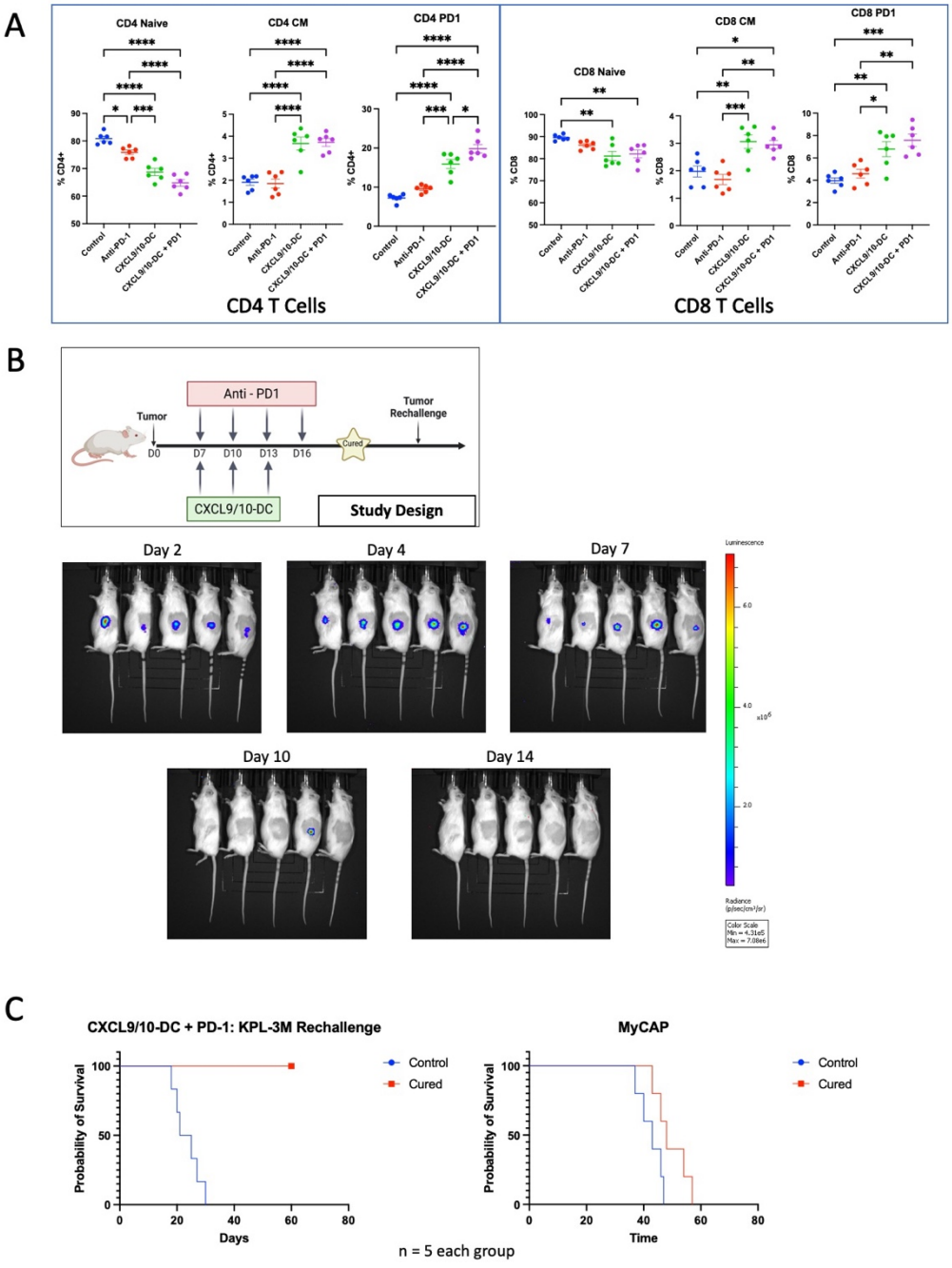

FIGURE 7

CXCL9/10-DC and anti-PD-1 combination treatment generates systemic immunity against tumor rechallenge

Study design for flow phenotyping and *in vivo* mouse models. **A)** Spleens were collected on D16 post inoculation ($1.25x10^5$ KPL-3M delivered SC) following treatment with vehicle control, anti-PD-1, CXCL9/10-DC or combination therapy. Flow cytometry was performed to assess $CD4^+$ and $CD8^+$ T cell subtypes and phenotype in the spleen to represent the systemic immune system. Significant decreases in $CD44^-CD62L^+$ naïve states of both $CD4^+$ and $CD8^+$ T cells with a shift to increasing $CD44^+CD62L^+$ central memory states. There was also an increase in $PD1^+$ staining for both cell types suggestive of activation. **B)** Mice treated with combination treatment of CXCL9/10-DC + anti-PD-1 leads to tumor eradication in some cases. Cured mice were rechallenged two months later with SC injection of $2.5x10^5$ KPL-3M tumors in the opposite flank. *In vivo* bioluminescence imaging (IVIS) was utilized to monitor tumor growth through the luciferase reporter in KPL-3M. Tumor engraftment was imaged at D2 and demonstrated tumor growth at D4. Tumor regression began as early as D7 and continued up to D10 with complete eradication in 5 mice by D14. **C)** Kaplan-Meier plot of KPL-3M rechallenge demonstrates rejection from cured mice while control mice maintained tumor growth post D4 and succumbed to tumor burden. Kaplan-Meier plot of syngeneic MyCAP rechallenge demonstrates that both cured and control mice were unable to eradicate MyCAP, highlighting tumor-specific systemic immunity.

CHAPTER 2

CCL21-ENGINEERED DENDRITIC CELLS

Rationale for CCL21

Despite recent advances in immunotherapy, many patients with non-small cell lung cancer (NSCLC) fail to respond to immune checkpoint inhibitors (ICI) and some relapse after an initial response[8,80-84]. Favorable responses to PD-1/PD-L1 blockade have been associated with high tumor mutational burden (TMB), increased baseline $CD8^+$ T lymphocytes tumor infiltration, and high PD-L1 expression in the tumor microenvironment (TME)[19,20,22,24]. Clonal TMB and a dormant tumor-infiltrating lymphocyte (TIL) signature as well as *IFN-g* and *CXCL9* signatures in the TME have also been associated with improved clinical benefit of ICI[25-28]. In contrast, impaired tumor antigen presentation in patients with NSCLC has been correlated with resistance to ICI[12,30,85]. These data implicate antigen-specific T cells as the critical mediators of anti-tumor responses to ICI in NSCLC. Therefore, therapies that enhance the quality and breadth of host tumor-specific T cell responses hold great promise for combating cancer immune resistance and evasion.

One approach to augment the efficacy of ICI is to promote host tumor-specific T cell responses by utilizing *in situ* vaccination (ISV) with autologous dendritic cells (DC)[86-88]. This antigen-agnostic approach provides the DCs access to the entire repertoire of tumor antigens and can potentially generate broad antigen-specific T cell responses. In preclinical trials, we have shown that gene-modified bone marrow-derived DCs that secrete C-C Motif Chemokine Ligand 21 (CCL21-DC) elicit potent anti-tumor immunity, which is dependent on CD4 and CD8 T lymphocytes as well as the IFN-g inducible chemokines CXCL9 and CXCL10[60,61,89]. CCL21 is a chemokine of interest because of its capacity to facilitate T cell activation by promoting co-localization of naïve lymphocytes and antigen-experienced DCs[90]. In a phase I trial in patients with advanced NSCLC, we have shown that intratumoral (IT) CCL21-DC increased CD8 T cells infiltration into the tumor and induced systemic tumor-specific immune responses in a subset of patients[59,91]. We observed a concurrent upregulation of PD-L1 in the TME following treatment, which may hinder T cell

function. We hypothesized that ISV with CCL21-DC could induce tumor-specific T cell responses and potentially sensitize immune resistant NSCLC to ICI.

Herein, we show that in multiple murine models of NSCLC with varying TMB, ISV with CCL21-DC synergizes with anti-PD-1 therapy, resulting in eradication of a subset of tumors and the establishment of systemic immune memory.

CCL21-DC ISV synergizes with anti-PD-1 therapy to inhibit NSCLC tumors

The efficacy of IT CCL21-DC in combination with anti-PD-1 was evaluated in multiple syngeneic murine models NSCLC. Treatment of immunocompetent mice bearing LKR-13 tumors with IT CCL21-DC or IP anti-PD-1 monotherapy generated moderate anti-tumor efficacy, while combination therapy resulted in a significant reduction of tumor growth (**Fig. 1A, Supplementary Fig S1**). Combination therapy with IT CCL21-DC and IP anti-PD-1 therapy was also evaluated in mice bearing *Kras*-mutant tumors with inactivating mutations of *Lkb1*, which has been recently identified as the major genetic driver of primary resistance to anti-PD-1 therapy[31]. As anticipated, mice bearing 1940A(KPL) tumors were resistant to anti-PD-1 therapy, but IT CCL21-DC monotherapy reduced tumor growth (**Fig. 1B**). Addition of anti-PD-1 to IT CCL21-DC resulted in synergistic inhibition of tumor growth (**Fig. 1B**). In contrast to human NSCLCs, genetically engineered murine models of NSCLC harbor low TMB with few protein-altering mutations[92-94]. Specifically, the LKR-13 and 1940A(KPL) tumors possess 0.67 and 1.75 mutations per Mb respectively, as determined by WES[64]. We reasoned that the paucity of tumor neoantigens in these models limits the anti-tumor efficacy of combination immunotherapy. Therefore, the efficacy of IT CCL21-DC and anti-PD-1 was evaluated in the KPL-3M syngeneic model with increased TMB (7.2 mutations per Mb)[64]. While IT CCL21-DC monotherapy provided moderate anti-tumor efficacy, the addition of anti-PD-1 resulted in a synergistic response with eradication of about 40%

of tumors (**Fig. 1C**). These data provide compelling evidence that IT vaccination with CCL21-DC can enhance the efficacy of anti-PD-1 therapy in murine models of NSCLC with low and high TMB.

CCL21-DC therapy promote enrichment of tumor-infiltrating neutrophils with a type I IFN signature

To evaluate the immune determinants of anti-tumor responses, we utilized the syngeneic KPL-3M model with loss of LKB1 and increased TMB that closely simulates the mutational landscape of immune-resistant NSCLC in human. The immune profiles of KPL-3M tumors and tumor-draining lymph nodes (Td-LN) were evaluated with flow cytometry 8 days after initiation of treatment (**Fig. 2A, Supplementary Fig. S2A**). Concurrently, pooled tumor cells from 6 mice in the control group and each treatment arm were enriched for $CD45^+$/Live cells by FACS sorting and processed via the 10X Single Cell 3' Gene Expression V3 with Novaseq S2. After exclusion of putative cell doublets and cells of high mitochondrial load (an indicator of cell death), cells were retained for analysis and visualized via UMAP.

Combination CCL21-DC/anti-PD-1 therapy resulted in a substantial enrichment of $CD45^+$ leukocyte in the TME compared to control or monotherapy as determined by flow cytometry (**Supplementary Fig. S2B**). scRNA-seq of tumors revealed 5 immune clusters compromising neutrophils, T and NK cells, and monocytes(Mono)/macrophages(MΦ)/cDCs, NK/T cells, plasmocytoid DC, and B cells based on expression profiles of known lineage marker genes (**Fig. 2B**). We observed an abundance of neutrophils within the $CD45^+$ compartment, consistent with prior reports revealing a neutrophil enriched TME in LKB1-deficient NSCLC[31-33,74] (**Fig. 2C**).

Spectral clustering of the tumor-infiltrating neutrophils (TIN) demonstrated four subsets (C1-4) (**Fig. 2D**). A recent single-cell analysis of tumor-infiltrating myeloid (TIM) cells in murine and human lung cancers identified six conserved neutrophil subsets (N1-N6)[95]. TINs formed a

continuum of states where N1 neutrophils, which were present in healthy tissue and expressed high amounts of canonical neutrophil markers (mmp8, mmp9, s100a8, s100a9, and adam8) progressed continuously in the tumor via N3 and N4 states to N5 neutrophils that promote tumor growth and expressed *Ccl3*, *Cd63*, *Cstb*, *Ctsb*, and *Irak2*[95]. A rare subpopulation of N2 neutrophils with strong transcriptional signature of type I interferon response genes, apart from the continuum of states, was also observed. Utilizing the reference datasets of the report[95], we defined C1 as N2 and C4 as N5. C2 shared the gene expression of closely related N4 and N6 subsets and the transcriptome of C3 resembled the gene expression profile of N1 and N3 (**Fig. 2E**). Treatment with CCL21-DC and combination therapy resulted in the reduction of TINs in the CD45+ compartment as determined by scRNA-seq and flow cytometry (**Fig. 2F-G** and **Supplementary Fig. S2C**). Significant enrichment of the C1/N2 subset with an expression signature of type I interferon response was noted in mice treated with anti-PD-1, CCL21-DC, or combination therapy compared to control (**Fig. 2F**). Increased expression of downstream interferon genes such as antigen-presenting genes, *H2-k1*, *H2-d1*, and *B2m,* and the interferon inducible checkpoint inhibitor *Cd274*(PD-L1) was noted in TINs following treatment (**Fig. 2H**). Increased PD-L1 protein expression on TINs was also seen by flow cytometry with the highest magnitude observed with combination CCL21-DC/anti-PD-1 therapy (**Fig. 2I**). These results suggest that CCL21-DC monotherapy and CCL21-DC/anti-PD-1 combination therapy profoundly alters the neutrophil compartment within the TME and results in enrichment of C1/N2 neutrophils with gene signature of type I interferon response.

CCL21-DC therapy result in the enrichment of 'activated' DC3 in the TME and the enhancement of cDC1/cDC2 migration to TdLN

Spectral clustering of the Mono/Mf/cDC population identified four subsets (C1-C4) (**Supplementary Fig. S3A**). C1 expressed monocyte- and macrophage-associated genes(**Supplementary Fig. S3B-C**). C2 shared gene profiles of Mono1 and Mono2 and C4 was

assigned as Mono3. C3 expressed signature genes associated with cDC. Flow analysis of TIMs identified six populations, namely neutrophils, Mono, conventional DC (cDC), Mf, Monocyte-derived (MC; Ly6c^{hi}MHCII^{hi}CD64^{-}) and Ly6c^{hi}MHCII^{hi}CD64^{-} cells (**Supplementary Fig. S3D**). Treatment with CCL21-DC monotherapy induced Mono infiltration into the TME but did not result in enrichment of MC and Ly6c^{hi}MHCII^{hi}CD64^{-} cells, which represent varying states of monocyte differentiation in the context of inflammation[96]. Combination therapy was associated with a statistically significant increase in Mo and MC within the TME. No changes in the Mf population was observed with treatment.

Dissection of the cDC population identified three clusters (C1-C3) (**Fig. 3A**). C1 and C3 shared gene signatures of both cDC1 and cDC2 but deferred in the expression of proliferation genes, which was enriched in C3 (**Fig. 3B&C** and **Supplementary Fig. S3E**). C2 lacked the conventional gene signatures associated with cDC1 and cDC2 and resembled recently described tumor-infiltrating 'activated' cDCs that upregulate the expression of maturation and migration genes upon uptake of tumor antigens and secrete IL-12 in response to IFN-g[95,97,98] (**Fig. 3B&C** and **Supplementary Fig. S3F**). This cluster was annotated as DC3. While, treatment with CCL21-DC monotherapy and combination therapy resulted in a statistically significant decrease in the DC population in the TME (**Fig. 3C&D**), DC3s were significantly enriched following treatment with CCL21-DC and combination therapy (**Fig. 3C**). ISV with CCL21-DC monotherapy or in combination with anti-PD-1 increased CD103^{+}cDC1 and cDC2 trafficking to the TdLN, which was accompanied by an enrichment of antigen experienced CD4 and CD8 T cells. These data highlight the role of autologous DCs in inducing therapeutic immunity in the TdLN.

CCL21-DC therapy induces Th1 polarization and the expansion of polyfunctional progenitor/precursor T cells in the TME

CCL21-DC monotherapy and combination therapy promoted infiltration of effector FOXP3$^-$CD4 and CD8 T cells and Tregs into the TME as determined by flow and scRNA-seq (**Fig. 4A** and **Supplementary Fig. S4A-D**). CD4 effector T cells were comprised of four clusters with distinct gene signatures corresponding to Th1, Th2, dysfunctional CD4 T cells (Tdysfx) expressing multiple exhaustion markers such as *Ctla4*, *Lag3*, *Pdcd1*, and *Havcr2* and central memory precursor CD4 T cells (Tcmp) with expression of Tcf7 (encoding TCF-1) associated with increased memory potential[99] (**Fig. 4B&C**). Although the transcriptional states of CD4 effector cells were conserved between treatment arms, CCL21-DC and combination therapy promoted significant expansion of the Th1 and Tcmp cells in the TME (**Fig. 4D**). Concurrent flow phenotyping of the FOXP3$^-$CD4 effector cells in the TME showed that CCL21-DC and combination therapy were associated with increased expression of the activation maker PD-1 and a substantial reduction in terminally exhausted PD1$^+$TIM3$^+$ cells (**Fig. 4E**). CCL21-DC and combination therapy also enhanced proliferation as determined by Ki-67 expression and INF-g secretion in FOXP3$^-$CD4 effector cells, which was greatest with combination therapy (**Fig. 4F&G**).

Tumor-infiltrating CD8 effector T cells, which predominantly expressed the PD-1 activation/exhaustion marker, were comprised of three clusters (C1-C3) (**Fig. 4H** and **Supplementary Fig. S4E**). C1 had low expression of effector gene program but expressed memory and exhaustion gene signature (**Fig. 4I**). This cluster was identified as progenitor exhausted effector CD8 T cells (progenitor_exh) base on comparison to the gene-sets from recent reports that have highlighted the self-renewal properties of these polyfunctional undifferentiated TILs that mediating the proliferative response to anti-PD-1 therapy[100,101]. C2 and C3 were annotated as terminally exhausted (terminally_exh) and effector like (effector_like), respectively. CCL21-DC monotherapy or combination therapy resulted in the enrichment of CD8 TILs in the TME with increased proliferation and the expansion of the progenitor-exh cells within the CD8 effector compartment (**Fig. 4A&J&K**). Only combination therapy resulted in increased IFN-g

secretion by CD8 effector cells (**Fig. 4L**). Tumor enrichment of NK cells with increased proliferation and INF-g secretion was also observed following CCL21-DC and combination therapy (**Fig. 4M-O**). All treatment arms, including anti-PD-1, CCL21-DC and their combination, resulted in increased PD-L1 expression on the tumors and MHC-II^{hi} Mf, MC, and cCD (**Fig. 4P**). Across all populations the expression of PD-L1 as determined by mean fluorescent intensity (MFI) was the highest following combination therapy, likely as a result of enhanced IFN-g production by NK and T cells.

CCL21-DC therapy induces maintained Th1 response both locally and systemically

To assess the evolution of local and systemic adaptive immune responses with time after ISV, flow phenotyping of tumors and spleens were performed at a later time, 11 days after the initiation of therapy (**Fig. 5A** and **Supplementary Fig. S5A**). An enrichment of CD45^{+} leukocytes was observed in the TME following CCL21-DC and combination therapy compared to control or anti-PD-1 monotherapy (**Supplementary Fig. S5B**). While a statistically significant decrease in FOXP3^{-}CD4 T cells was observed on day 18 (D18) compared to D15 in the control mice, no detriment in TILs was noted within the TME following CCL21-DC monotherapy and combination therapy resulted in enrichment of TILs, although it did not reach statistical significance (**Fig. 5B**). Significant enrichment of TILs was noted in the TME following CCL21-DC and combination therapy compared to anti-PD-1 and control. In addition, TILs from control mice had diminished function as determined by IFN-g production on D18 compared to D15 (**Fig. 5C**). The highest amount of stable IFN-g secretion by FOXP3^{-}CD4 and CD8 T cells was noted with the addition of anti-PD-1 to CCL21-DC. These data illustrate that ISV with CCL21-DC induces durable infiltration of CD4 and CD8 effectors in the TME and the addition of anti-PD-1 augments tumor-infiltration and function of those lymphocytes.

Comparison of lymphocyte compartment from the spleen of tumor-bearing mice on D15 and D 18 revealed expansion of central memory (CM) FOXP3$^-$CD4 and CD8 T cells, effector memory (EM) CD8 T cells, and Tregs in all treatment groups, but the prevalence of FOXP3$^-$CD4 T cells did not change with time (**Fig. 5D**). CCL21-DC and combination therapy resulted in a significant enrichment of the CM and EM CD8 T cells in spleen compared to anti-PD-1 and control on D18. CCL21-DC and combination therapy also resulted in the highest enrichment of EM FOXP3$^-$CD4 T cells and a concurrent decrease in Tregs (**Fig. 5D**). Concurrently, increased IFN-g secretion from splenic CD4 and CD8 T cells was observed on D18 compared to D15, which was highest in magnitude following CCL21-DC and combination therapy (**Fig. 5E**). Collectively, these data suggest expansion of systemic T cell responses following ISV with CCL21-DC as monotherapy or in combination with anti-PD-1.

CCL21-DC/anti-PD-1 therapy results in immunoediting of tumor subclones and generates systemic tumor-specific immune memory

The dynamic interplay between antigen-specific T cells and tumor cells can result in immunoediting of the tumor cells and the escape of resistant clones[102]. To assess whether combination therapy with CCL21-DC and anti-PD-1 facilities immunoediting of tumor subclones, SQ KPL-3M tumors in immunocompetent FVB mice, which are composed of a heterogenous pool of tumor clones[64], were harvested on day 7 prior to initiation of therapy and on day 25 after treatment with vehicle control or combination therapy (**Fig. 6A**). Given that the combination therapy results in eradication of a significant fraction of tumors, only tumors that were stabilized or growing were selected from the combination group. WES of FACS sorted Live/CD45- population revealed 7 clusters of tumor subclones (**Fig. 6B**). Combination treatment resulted in complete elimination of C2-3 and near complete elimination of C1&4. No change in the variant allele frequency (VAF) of C5&6 was noted following treatment, suggesting immune resistance. Emergence of C7 was noted following combination treatment, which likely represents enrichment

of an immune resistant subclone. These data provide compelling evidence that ISV with CCL21-DC combined with anti-PD-1 induces immunoediting of tumor subclones.

Next, to assess whether combination therapy could result in the establishment of systemic tumor-specific immune memory, mice cured of KPL-3M tumors following combination therapy were inoculated with KPL-3M or control MycCAP tumors from the same FVB background 90 days after treatment (**Fig. 6C&D**). Cured mice rejected all KPL-3M tumors but succumbed to MycCAP tumors. WT FVB mice served as additional control and succumbed to both KPL-3M and MycCAP tumors (**Fig. 6C&D**). These data demonstrate the generation of systemic tumor-specific immune memory following successful eradication of KPL-3M tumors with CCL21-DC ISV in combination with anti-PD-1.

Discussion

In various murine models of NSCLC with varying TMB, *in situ* vaccination with CCL21-DC synergizes with anti-PD-1 therapy to inhibit tumor growth leading to tumor eradication in a subset of mice and the establishment of systemic immunity. Phenotypic analysis of CCL21-DC treatment highlights a remodeling of the immune microenvironment to promote an anti-tumor response. Enrichment of infiltrating neutrophils expressing a type I IFN signature was shown. In addition, CCL21-DC therapy lead to the activation of dendritic cells labeled cDC3 followed by an enhanced migration of cDC1/cDC2 subtypes to the tumor draining lymph. This coincided with increased activation of T cells in the tumor draining lymph node. In depth analysis of T cells highlighted an increase in effector T cells with the Th1 subtype and CD8 effector T cells. This led to an increased IFNg signature from both T cell subtypes that persisted over time in the tumor. Tumor clonality analysis showed immunoediting following CCL21-DC therapy and the successful generation of systemic immunity in cured mice specific to KPL-3M.

Previously in a phase I trial in patients with advanced NSCLC, intratumoral (IT) CCL21-DC increased CD8 T cells infiltration into the tumor and induced systemic tumor-specific immune responses in a subset of patients[59,91]. In this preclinical model, it was demonstrated that CCL21-DC can potentially synergize with anti-PD-1 therapy to enhance the anti-tumor response. Currently, our lab is undergoing a phase I clinical trial to investigate this combination and its safety profile in patients of NSCLC (NCT03546361). Immune phenotyping from collected PBMC and tumor biopsies were performed to better understand the patient immune response following therapy. We hope to synthesize both pre-clinical and clinical changes to better understand the immune response following combination therapy, and potentially sensitize immune resistant NSCLC to ICI.

Chapter 2 – Figure 1

Figure 1

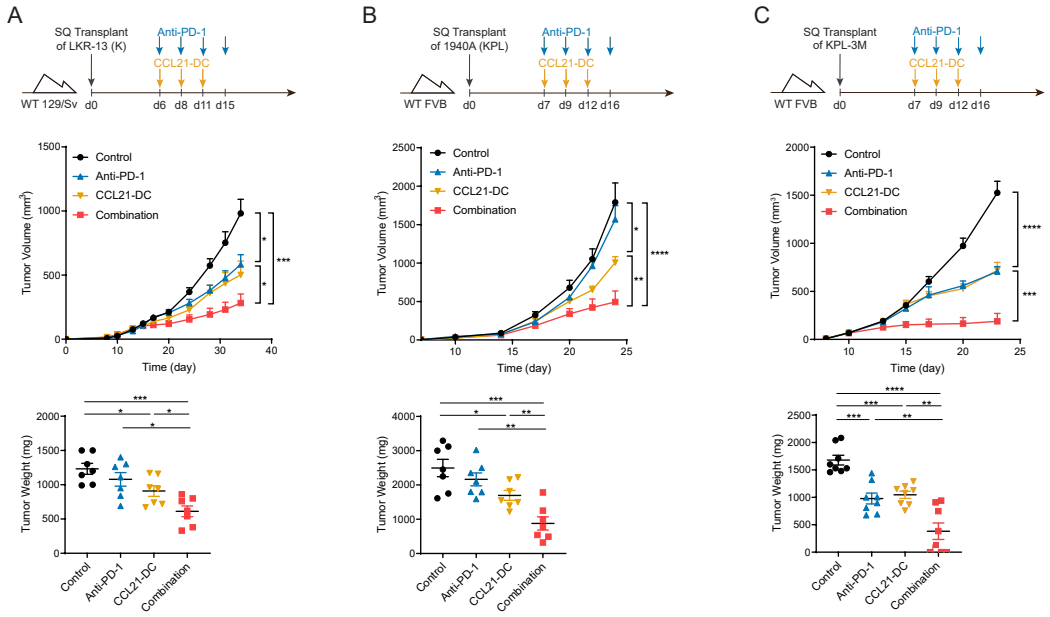

FIGURE 1

CCL21-DC ISV synergizes with anti-PD-1 therapy to inhibit NSCLC tumors

Study design of *in vivo* mouse models of NSCLC. **A)** On D6 post tumor inoculation ($1.0x10^6$ LKR13 tumor cells delivered SC), 129-E mice bearing ~$50mm^3$ tumors were treated with i) vehicle, ii) $2.0x10^6$ CCL21-DC for a total of 3 injections at D6, D8 and D11, iii) anti-PD-1 (200µg/dose IP) at D6, D8, D11 and D15, or iv) combination therapy. Combination therapy was synergistically more efficacious than monotherapies as measured by tumor volume and tumor weights. **B)** On D6 post tumor inoculation ($1.0x10^6$ 1940A KPL tumor cells delivered SC), FVB/NCrl mice bearing ~$50mm^3$ tumors were treated with i) vehicle, ii) $2.0x10^6$ CCL21-DC for a total of 3 injections at D6, D8 and D11, iii) anti-PD-1 (200µg/dose IP) at D6, D8, D11 and D15, or iv) combination therapy. Combination therapy was synergistically more efficacious than monotherapies in a low tumor mutational burden of *Kras*-mutant tumors with inactivating mutations of *Lkb1*. **C)** On D6 post tumor inoculation ($1.0x10^6$ 1940A KPL tumor cells delivered SC), FVB/NCrl mice bearing ~$50mm^3$ tumors were treated with i) vehicle, ii) $2.0x10^6$ CCL21-DC for a total of 3 injections at D6, D8 and D11, iii) anti-PD-1 (200µg/dose IP) at D6, D8, D11 and D15, or iv) combination therapy. Combination therapy was synergistically more efficacious than monotherapies in a high tumor mutational burden of *Kras*-mutant tumors with inactivating mutations of *Lkb1*.

Chapter 2 – Supplemental Figure 1

Supplemental Figure 1

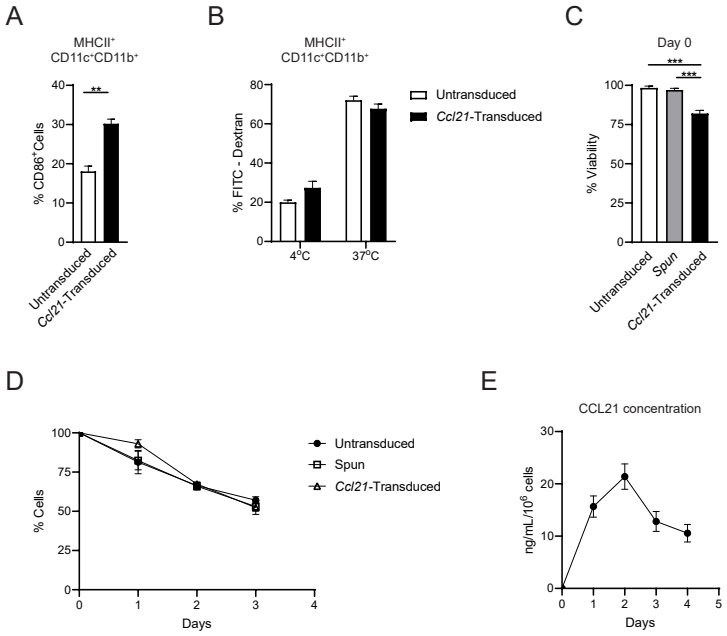

SUPPLEMENTAL FIGURE 1

Generation of CCL21-DC and phenotyping

Characterization of CCL21-DC by flow cytometry. **A)** Increased $CD86^{+}$ expression of CCL21-DC following lentiviral transduction. **B)** CCL21-DC maintains function following transduction as measured by FITC dextran uptake assay. **C)** CCL21-DC viability though reduced maintains a >80% viability following transduction. **D)** Transduction with CCL21 doesn't affect survivability of transduced dendritic cells. **E)** CCL21-DC secretion of CCL21 protein as measured by ELISA over time.

Chapter 2 – Figure 2

Figure 2

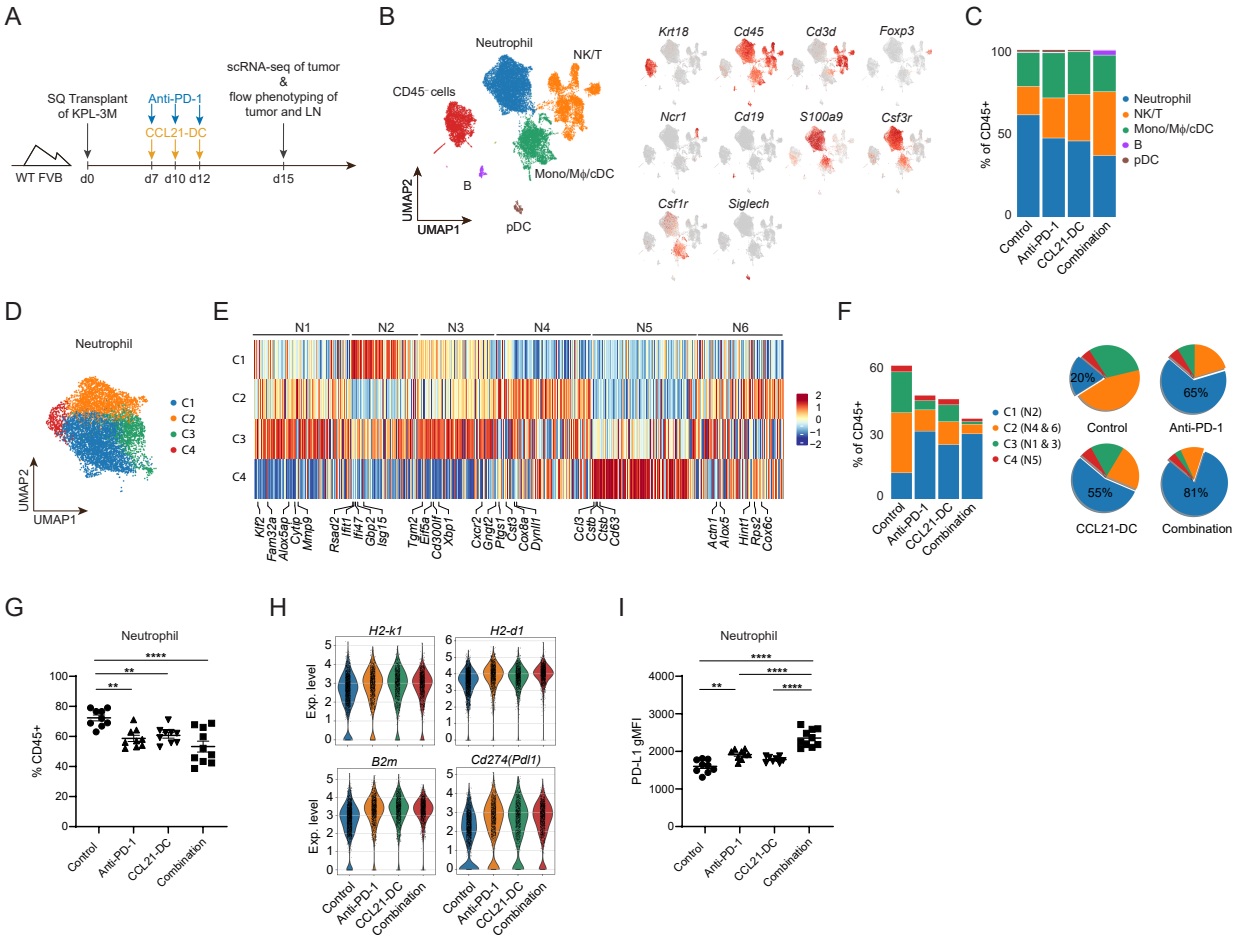

FIGURE 2

CCL21-DC promotes enrichment of tumor-infiltrating neutrophils with a type I IFN signature

Single cell analysis and flow phenotyping of CCL21-DC treated tumors. **A)** Tumors were collected on D15 post inoculation ($1.25x10^5$ KPL-3M delivered SC) following treatment with vehicle control, anti-PD-1, CCL21-DC or in combination for single cell RNA sequencing and flow phenotyping. **B)** Immune clustering of various immune cell populations identified 5 major populations comprising neutrophils, T and NK cells, and monocytes(Mono)/macrophages(MΦ)/cDCs, NK/T cells, plasmocytoid DC, and B cells based on expression profiles of known lineage marker genes. **C)** Quantification of the different immune populations based on treatment groups. **D&E)** Spectral clustering of the tumor-infiltrating neutrophils demonstrated four subsets classified based on their gene signatures to a recent publication investigated six conserved neutrophil subsets in murine and human lung cancers[95]. **F)** Treatment with CCL21-DC showed a reduction in TINs and enrichment of the C1(N2) subset compared to control. **G)** Flow cytometry confirms statistical decrease of TINs when compared to control. **H)** Increased expression of downstream interferon genes, *H2-k1*, *H2-d1*, and *B2m,* and *Cd274*(PD-L1) was noted in TINs following treatment. **I)** Increased PD-L1 protein expression on TINs was also seen by flow cytometry.

Chapter 2 – Supplemental Figure 2

Supplemental Figure 2

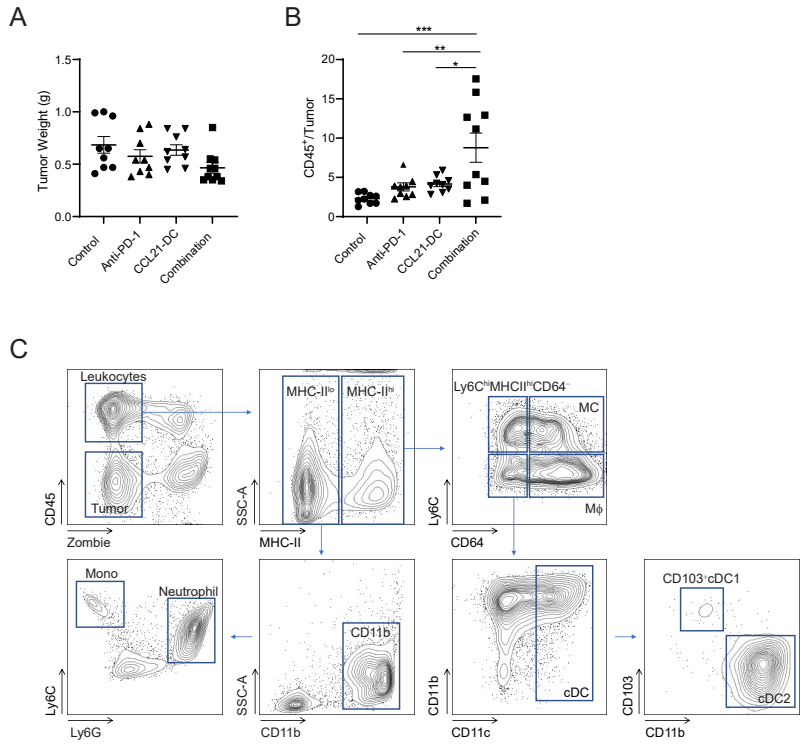

SUPPLEMENTAL FIGURE 2

Tumor collection and gating strategy for immune phenotyping

Flow phenotyping of *in vivo* CCL21-DC treated tumors. **A)** Tumor weights measured during tissue collection of four treatment groups shows no change; control, anti-PD-1, CCL21-DC and combination therapy. **B)** Increase in $CD45^{+}$ to tumor ratio following combination therapy. **C)** Flow phenotype gating strategy of various immune phenotypes.

Chapter 2 – Figure 3

Figure 3

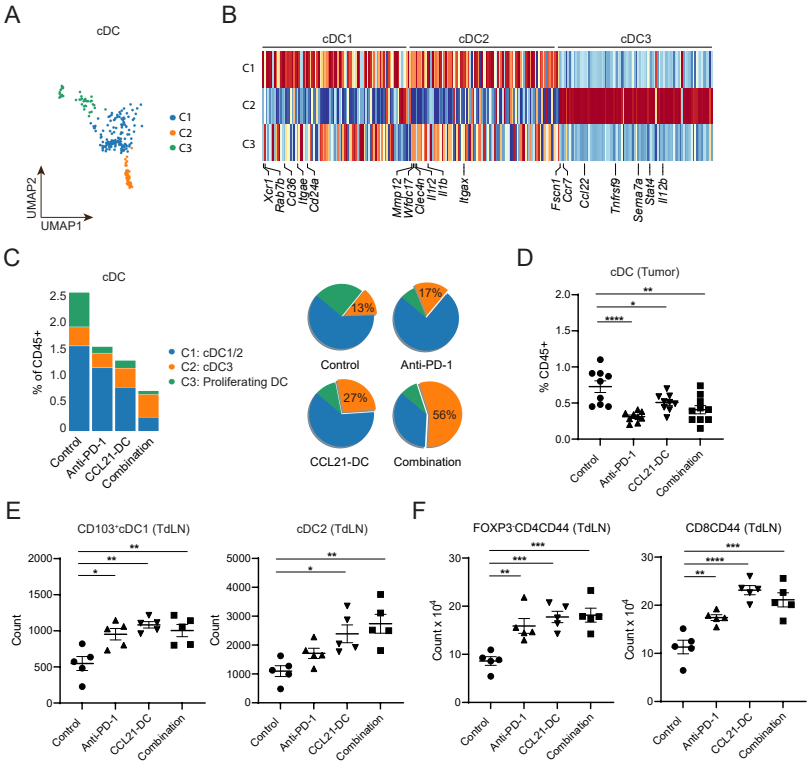

FIGURE 3

CCL21-DC results in enrichment of results in the enrichment of 'activated' DC3 in the TME and the enhancement of cDC1/cDC2 migration to tumor-draining LN

Single cell analysis and flow phenotyping of CCL21-DC treated tumors and TdLN. **A)** Spectral clustering of the cDC population identified three clusters (C1-C3). **B)** Gene signature analysis identifies C1 as cDC1 and cDC2, C2 as cDC3. **C)** Cluster 2, cDC3, were significantly enriched following treatment with CCL21-DC and combination therapy. **D)** Flow cytometry showing significant decrease in cDC compartment following therapy. **E)** Tumor draining lymph node shows increased in $CD103^{+}$cDC1 and cDC2 compartment following CCL21 therapy. **F)** Flow cytometry showed increase activation of $FOXP3^{-}CD4^{+}CD44^{+}$ and $CD8^{+}CD44^{+}$ following CCL21-DC therapy.

Chapter 2 – Supplemental Figure 3

Supplemental Figure 3

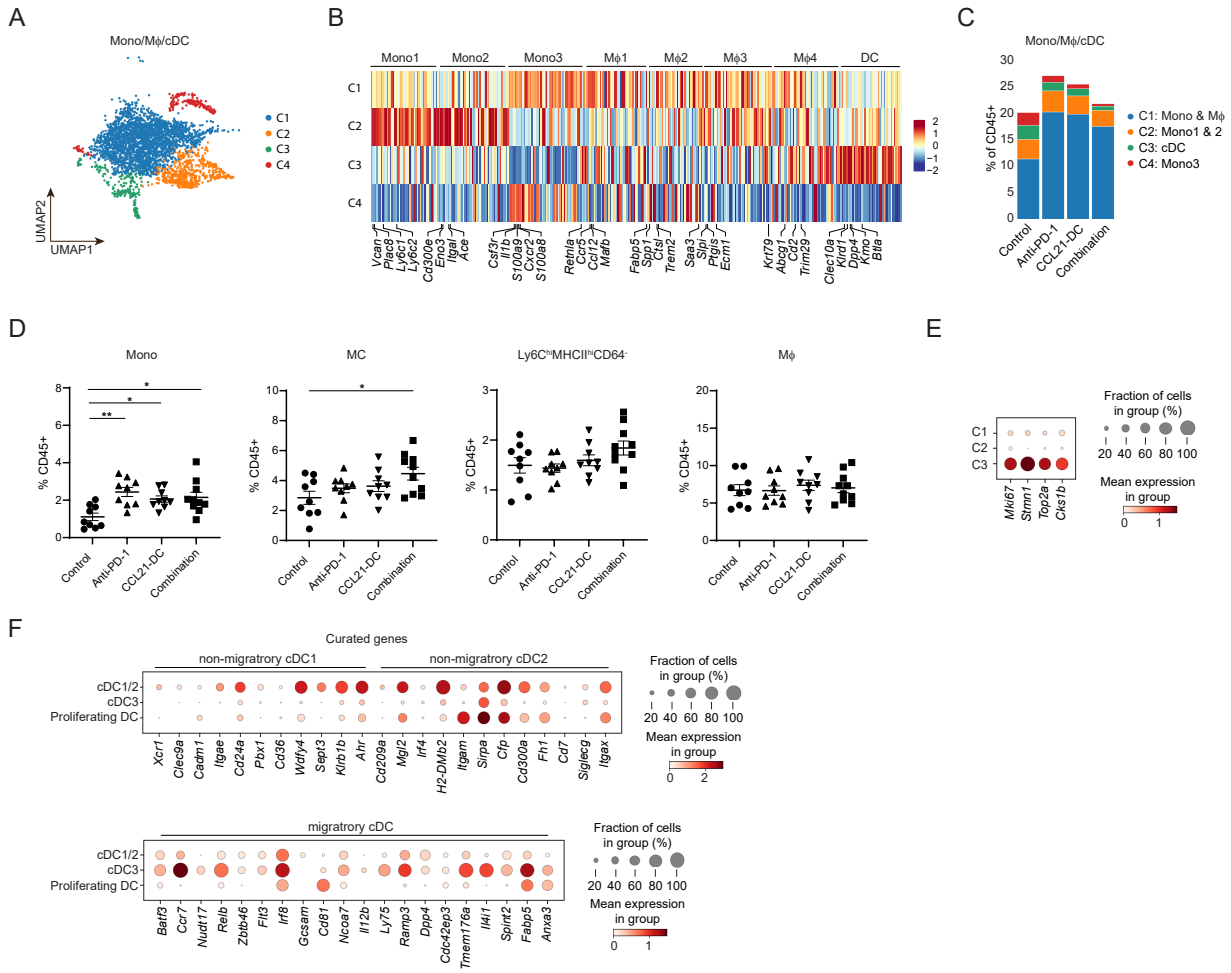

SUPPLEMENTAL FIGURE 3

Spectral clustering of Mono/Mf/cDC population

Single cell analysis and flow phenotyping of CCL21-DC treated tumors **A&B)** Spectral clustering of the Mono/Mf/cDC population identified four subsets with C1 associated with monocyte and macrophage associated genes, C2 was primarily Mono 1 and Mono 2monocyte genes, C3 showed dendritic cells profiles and C4 showed Mono3. **C)** Treatment with control, anti-PD-1, CCL21-DC or combination leads to changes in the various subclusters. **D)** Flow analysis of TIMs identified four other populations, namely monocytes, macrophages, Monocyte-derived (MC; $Ly6c^{hi}MHCII^{hi}CD64^{-}$) and $Ly6c^{hi}MHCII^{hi}CD64^{-}$ cells. **E)** Single cell analysis of cDC1 subgroups highlights the proliferative nature of cluster 3. **F)** Further single cell analysis of dendritic cells subclusters highlights cDC3 migratory phenotype.

Chapter 2 – Figure 4

Figure 4

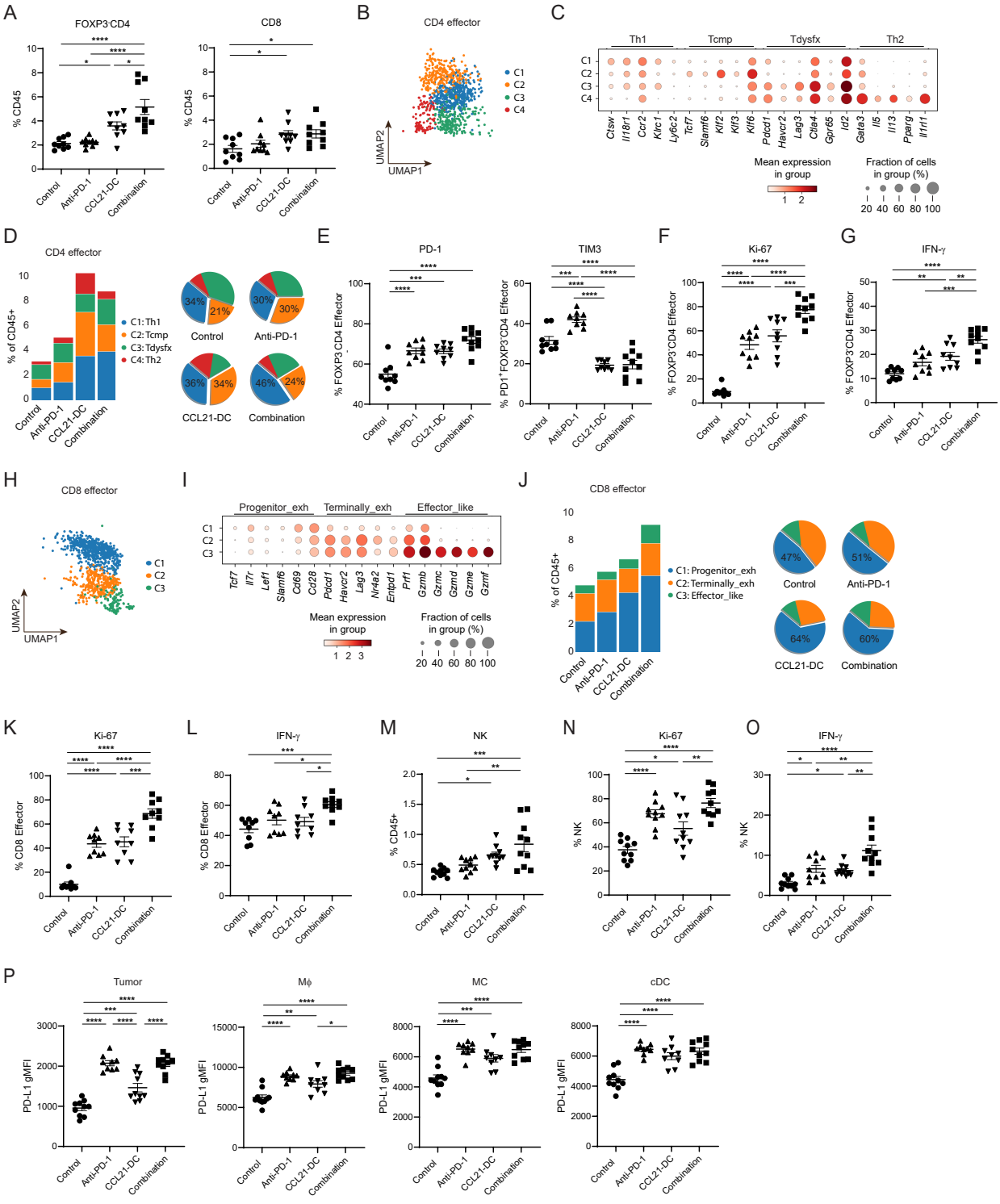

FIGURE 4

CCL21-DC induces Th1 polarization and the expansion of polyfunctional progenitor/precursor T cells in the TME

Single cell analysis and flow phenotyping of CCL21-DC treated tumors. **A)** Flow phenotyping demonstrates increase of $FOXP3^{-}CD4^{+}$ and $CD8^{+}$ T cells following CCL21-DC therapy. **B&C)** Spectral clustering of the $CD4^{+}$ T cell population identifies Th1 subtype, Th2 subtpye , dysfuntional T cells (Tdysfx) and central memory precursors (Tcmp). **D)** Single cell analysis shows treatment with CCL21-DC leads to increased Th1 and central memory precursors. **E)** Flow phenotyping of the $FOXP3^{-}CD4$ effector cells in the TME showed that CCL21-DC increased expression of PD-1 activation and a substantial reduction in terminally exhausted $PD1^{+}TIM3^{+}$ cells. **F&G)** Flow phenotype showed increase proliferation ($Ki67^{+}$) and activation of the Th1 subtype (IFNg). **H&I)** Single cell clustering of $CD8^{+}$ T cell show progenitor exhausted, terminally exhausted and effector like states. **J)** CCL21-DC therapy led to increase of effector like $CD8^{+}$ T cells when compared to control. **K&L)** Similar to $CD4^{+}$ T cells, $CD8^{+}$ T cells showed increase proliferation and activation based on $Ki67^{+}$ and IFNg staining, respectively. **M)** CCL21-DC also facilitated an increase in NK cells following treatment. **N&O)** Increased activation of NK cells following CCL21-DC therapy. **P)** PD-L1 expression based on flow phenotyping of tumor, macrophages, monocytes and cDC immune cells.

Chapter 2 – Supplemental Figure 4

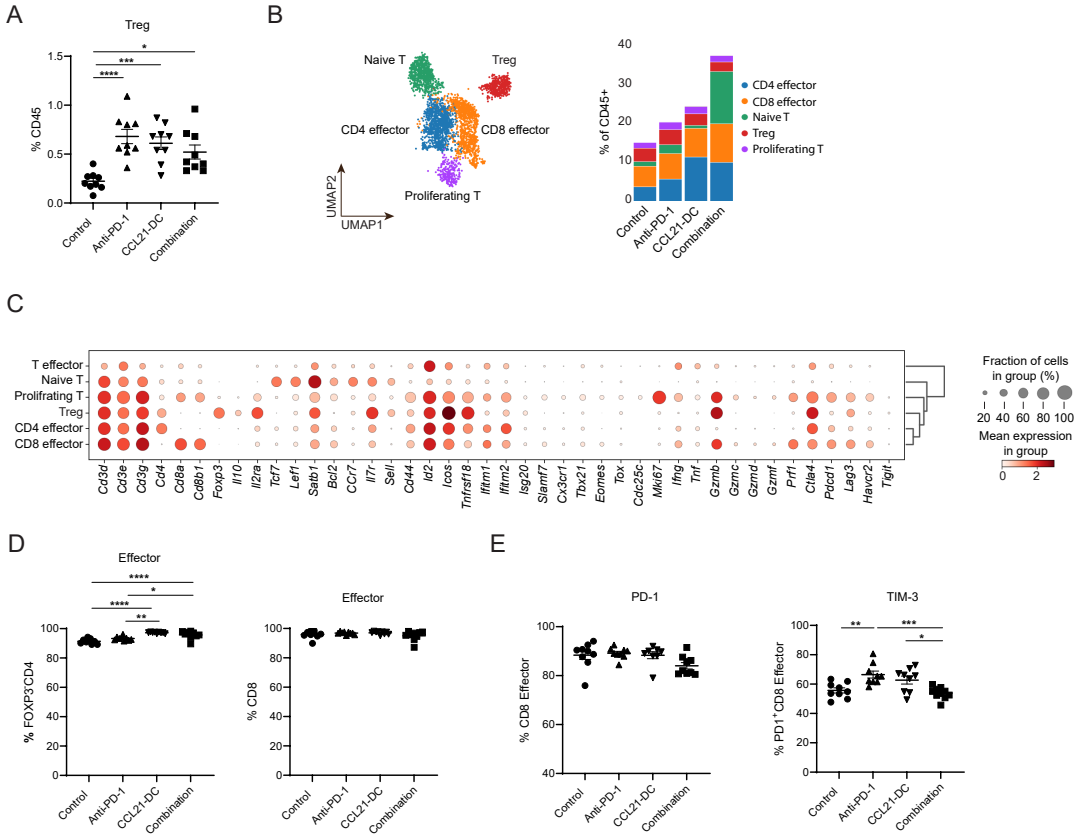

SUPPLEMENTAL FIGURE 4

Single cell analysis and flow phenotyping of tumor infiltrating T cells

Single cell analysis and flow phenotyping of CCL21-DC treated tumors **A)** Flow analysis of T regulatory cells defined by $CD4^{+}FOXP3^{+}$ shows increase following treatment when compared to control. **B)** Spectral clustering of T cell subtypes shows clustering of naïve T cells, T regulatory cells, proliferating T cells, CD4 effector and CD8 effector T cells. Bar graph shows quantification following single cells analysis of clusters. **C)** Gene expression data of T cell subsets. **D)** Flow phenotyping shows increase in activation state (CD44) of $FOXP3^{-}CD4^{+}$ T cells while $CD8^{+}$ T cells show no change. **E)** Flow phenotyping of $CD8^{+}$ effector T cells show no changes in PD-1 expression with a decrease in $TIM3^{+}$ suggestive of exhaustion.

Chapter 2 – Figure 5

Figure 5

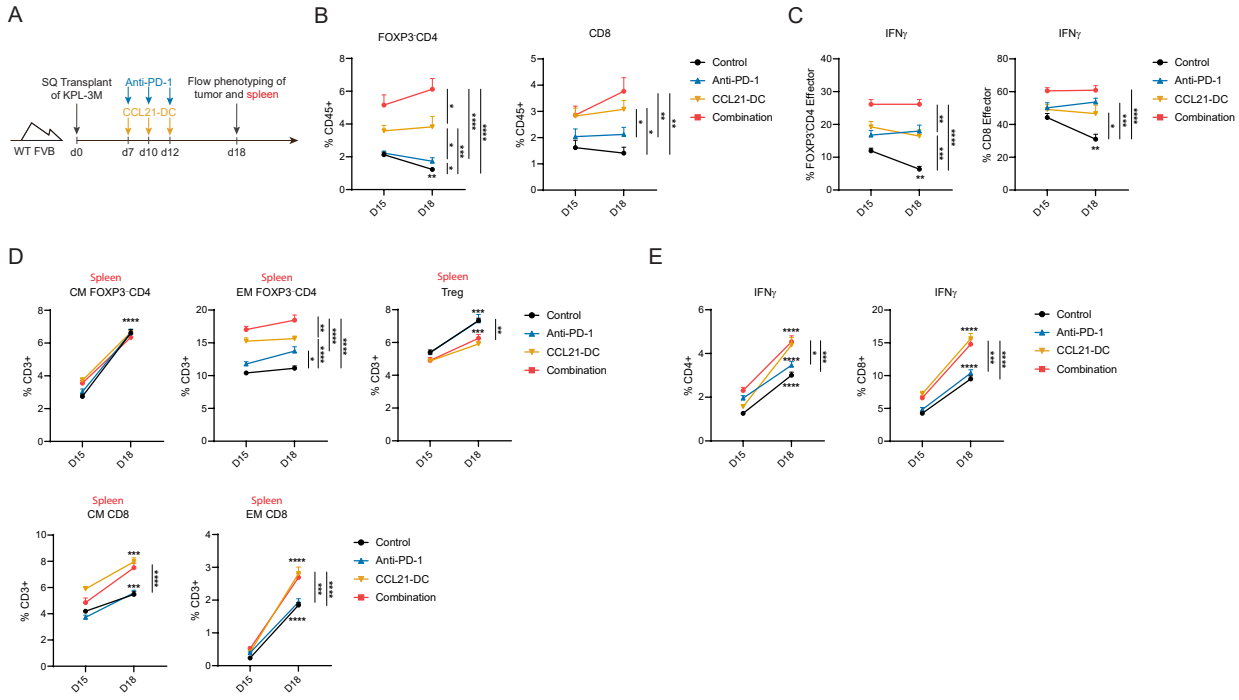

FIGURE 5

CCL21-DC monotherapy and CCL21/anti-PD-1 therapy induces maintained Th1 response both locally and systemically

Flow phenotyping of CCL21-DC treated tumors and spleen. **A)** Tumors were collected on D15 and D18 post inoculation ($1.25x10^5$ KPL-3M delivered SC) following treatment with vehicle control, anti-PD-1, CCL21-DC or in combination for single cell RNA sequencing and flow phenotyping. **B)** Flow phenotyping of the $FOXP3^-CD4$ effector cells and $CD8^+$ T cells showed an increase over time following combination therapy. **C)** IFNg signature is elevated and maintained in both CD4+ and CD8+ T cells with CCL21-DC and anti-PD-1 therapy. **D)** Increases in both central memory and effector memory for both CD4+ and CD8+ T cells with significant increases following CCL21-DC therapy. Higher percentage of regulatory $CD4^+$ T cells were also found in control and anti-PD-1 groups. **E)** Significant increase in IFNg signature in splenic CD4+ and CD8+ T cells following CCL21-DC therapy.

Chapter 2 – Supplemental Figure 5

Supplemental Figure 5

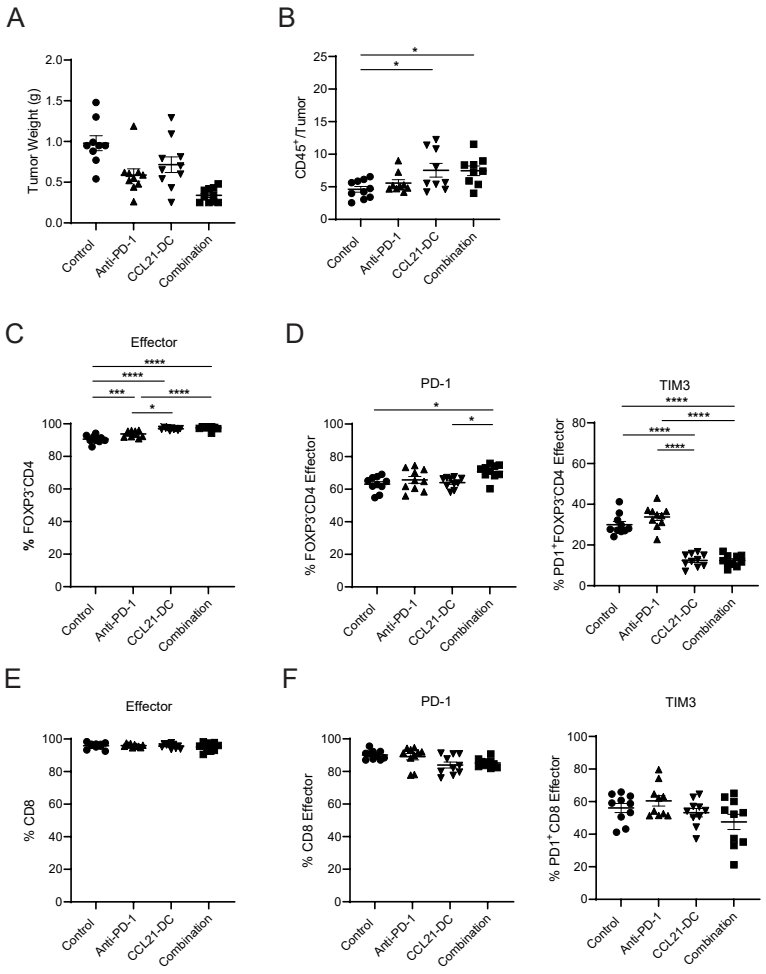

SUPPLEMENTAL FIGURE 5

Flow phenotyping of splenic T cells

Flow phenotyping of spleens from CCL21-DC treated mice. Tumor and spleens were collected on D15 and D18 post inoculation ($1.25x10^5$ KPL-3M delivered SC) following treatment with vehicle control, anti-PD-1, CCL21-DC or in combination for flow phenotyping. **A)** Tumor weights on D18 of the four treatment groups prior to single cell isolation for flow phenotyping. **B)** Increase in $CD45^+$ to tumor ratio following combination therapy at D18. **C&D)** Flow phenotyping showed increase in activation state (CD44) of $FOXP3^-CD4^+$ T cells at D18 with slight increase in PD-1 activation following therapy and significant decrease in $TIM3^+$ staining. **E&F)** Flow phenotyping of $CD8^+$ T cells showed no change in effector state (CD44), $PD1^+$ or $TIM3^+$ staining at D18.

Chapter 2 – Figure 6

Figure 6

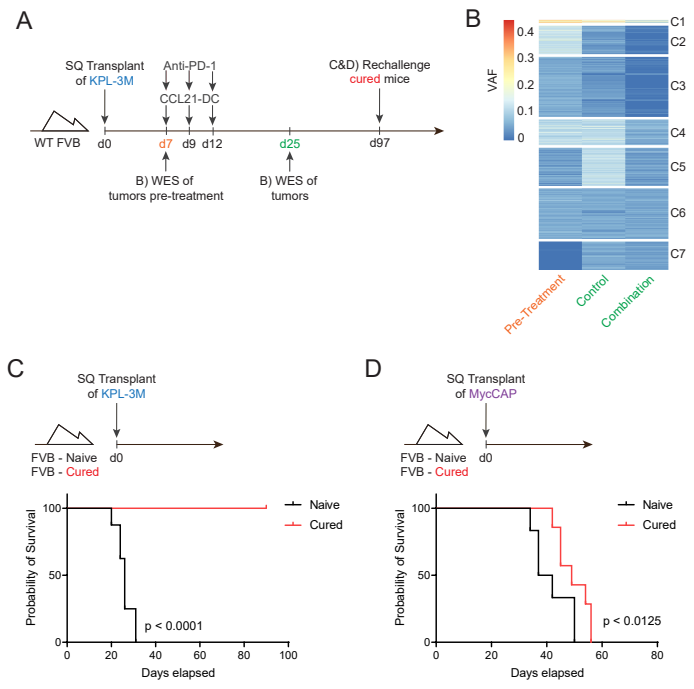

FIGURE 6

CCL21-DC/anti-PD-1 combination therapy results in immunoediting of tumor subclones and generates systemic tumor-specific immune memory

Study design for *in vivo* mouse models. **A)** KPL-3M tumors in immunocompetent FVB mice were harvested on day 7 prior to initiation of therapy and on day 25 after treatment with vehicle control or combination therapy. A subset of cured mice were rechallenged at d97 following successful tumor eradication. **B)** Whole exome sequencing were performed on FACS sorted Live/CD45- population to reveal 7 clusters of tumor subclones. Analysis was on how combination treatment changed the various tumor subclones. **C&D)** Mice cured of KPL-3M tumors following combination therapy were inoculated with KPL-3M or control MycCAP tumors from the same FVB background 90 days after treatment. Kaplan-Meier survival curves are plotted to demonstrate complete rejection of KPL-3M tumors by cured mice but succumbed to MyCAP tumors. Naïve mice succumbed to both types of tumors.

CHAPTER 3

LUNG CANCER PREMALIGNANCY AND IMMUNE MARKERS

Introduction

An in-depth understanding of lung cancer biology and mechanisms of tumor progression has facilitated significant advances in the treatment of lung cancer [7]. For example, tyrosine kinase inhibitor (TKI) targeted therapies and immune checkpoint blockade (ICB) immunotherapies have resulted in durable responses and survival benefits in subsets of non-small cell lung cancer (NSCLC) patients. The lung cancer survival rate, however, remains low, particularly for metastatic disease. There is a pressing need for the development of innovative approaches to detect and intercept lung cancer at its earliest point. Recent advances in genomics, computational biology and new technologies offer unique opportunities to identify the earliest cellular and molecular events associated with lung carcinogenesis as well as the immune landscape in the tumor microenvironment (TME). This will afford the development of novel strategies for cancer interception prior to the progression to advanced stages [103,104]. Here, we will highlight the concept of immunoediting and focus on recent studies assessing immune changes in the context of lung cancer pathogenesis and early detection.

History of Immunosurveillance and Cancer Immunoediting

Among the earliest demonstrations of the capacity of the immune system to affect tumor development were those formulated by Paul Ehrlich in 1909. He found that the injection of weakened cancer cells generated tumor immunity in mice and concluded that the host defense system can keep emerging tumors at bay [105]. This revolutionary concept was galvanized by Lewis Thomas in 1959 who postulated that the immune system has the capacity to protect against the development of cancer [106]. These early notions laid the foundation for Burnet's concept of immunosurveillance. He wrote: "*it is an evolutionary necessity that there should be some mechanism for eliminating or inactivating such potentially dangerous mutant cells and it is postulated that this mechanism is of immunological character."* [107] Studies from Old and Boyse at that time supported this hypothesis through the identification of murine tumor antigens [108].

These studies shaped the early concepts of immunosurveillance but they were limited by scientific approaches to fully demonstrate that the immune system played a role in cancer pathogenesis. It was not until the early 2000s with advances in knockout mice and genetic models that the immunosurveillance concept was experimentally confirmed. For example, immunogenic tumor cells expressing dominant negative Interferon Gamma (IFN-γ) receptors were found to have enhanced growth *in vivo* [109]. Other studies using perforin knockout mice and eventually recombination activating gene 1 (RAG-1) or RAG-2 knockout mice solidified the concept that the immune system, specifically lymphocytes, protected the host against chemically induced tumors and spontaneously developing epithelial tumors [110]. The studies by Smyth *et al*. and Dunn *et al*. shed further light on the mechanisms of immunosurveillance [111-114]. Subsequent studies not only suggested the involvement of the immune system in protecting humans, but also demonstrated the emergence of tumors with reduced immunogenicity.

These studies established immunosurveillance while simultaneously raising a new question: if the immune system has the capability to prevent and eradicate neoplastic cells, why does cancer still develop? This question, along with the discovery of tumors with reduced immunogenicity, led to the concept of cancer immunoediting. Cancer immunoediting highlights a three-phase model of tumor growth: elimination, equilibrium and escape [112]. Elimination embodies the classical concept of cancer immunosurveillance in which the immune system eradicates neoplastic disease. Equilibrium defines a state of continued immune elimination with incomplete tumor destruction. Finally, escape is the outgrowth of tumor cells that have successfully evaded the immune response of the previous phase.

Premalignancy, Lung Cancer and Early Detection

Lung cancer is the leading cause of cancer death worldwide, accounting for 25% of all cancer deaths. In 2017, there were 2.2 million incident cases and 1.9 million deaths. The Global Burden of Disease Collaboration has reported that from 2007 to 2017, lung cancer cases have increased by 37% worldwide [115]. Approximately 85% lung cancer patients have NSCLC, which are composed of two major subtypes, lung squamous cell carcinoma (LUSC) and lung adenocarcinoma (LUAD) [7]. Lung cancer is often diagnosed at advanced stages leading to a poor prognosis. The 5-year survival rate is approximately 17%. Multiple efforts are now being directed at diagnosing lung cancer at earlier stages. The National Lung Screening Trial (NSLT) [116,117] and the Nederlands-Leuvens Longkanker Screenings Onderzoek, (NELSON) trial [118] both used low-dose computed tomography (LDCT) to screen high-risk populations to reduce lung cancer mortality. These ground-breaking studies demonstrate the importance and impact of early detection. Studies are now focused on improving the performance characteristics of LDCT scans via radiomics and machine learning as well as using additional non-invasively obtained biomarkers to complement imaging based assessments. An abnormal LDCT scan could result from benign, premalignant or invasive disease. Understanding the cellular and molecular determinants of pulmonary premalignancy progression to invasive cancer will facilitate detection and interception of lung cancer at its earliest stages.

With the recognition that a better understanding of early stages of lung cancer pathogenesis can improve patient outcomes through early diagnosis and interception, the National Cancer Institute (NCI) launched multiple initiatives to direct the research effort to lung cancer early detection. The Early Detection Research Network (EDRN) was initiated by the NCI to bring together multiple institutions to identify biomarkers for clinical applications for early cancer detection. Another effort facilitated by the NCI is the PreCancer Atlas (PCA) initiative, which aims to utilize a comprehensive multi-omic strategy to establish detailed molecular and cellular characteristics of premalignant lesions and their evolution to invasive cancer [119-121]. Technological advances in

autofluorescence bronchoscopy (AFB), multispectral imaging and laser capture microdissection (LCM) have allowed for better characterization of these lesions. Coupled with enhanced analysis tools in multiplex immunofluorescence (MIF), mass cytometry by time-of-flight (CyTOF), genome-wide omic approaches and single cell sequencing, studies are assessing premalignancy and the immune microenvironment to better understand the molecular and cellular determinants of lung cancer progression. Efforts focusing on MIF are highlighted below that are aimed at defining immunity markers in pulmonary premalignancy and early-stage lung cancer.

Immune changes in LUAD premalignancy and early-stage NSCLC focusing on changes in precursor atypical adenomatous hyperplasia (AAH)

The mutational landscape and the associated immune contexture in the LUAD continuum were interrogated by Krysan *et al*. who performed whole exome sequencing (WES) of resection biospecimens from 41 lung cancer patients, which included laser captured microdissection of 89 AAH lesions, 15 adenocarcinomas *in situ* (AIS), 55 invasive LUAD and their adjacent normal lung tissues [122]. The authors designated the somatic mutations detected in both lung adenomatous premalignant lesions and the associated tumors as progression-associated mutations (PAMs). Putative neoantigens from these mutations correlated with the infiltration of $CD4^+$ and $CD8^+$ T cells and the upregulation of PD-L1, suggesting adaptive immunity and possible recognition of neoepitopes occurring in pulmonary premalignancy. The percentage of putative progression-associated neoantigens significantly correlated with the percentage of $CD8^+$ T cells infiltrating AAH lesions, whereas the overall neoantigen load in AAH was associated with $CD4^+$ T cell infiltration and PD-L1 expression. Analysis of the immune-related gene expression in the Cancer Genome Atlas (TCGA) LUAD dataset revealed that patients with higher immune-related gene expression had better survival compared to patients with the lowest expression of immune genes. This difference was most prominent in stage I patients, suggesting that modulation of the immune-

related pathways, especially at the early stages of LUAD, may have a significant impact on patient outcomes.

To further examine the premalignant lesions, H&E patient samples were collected and analyzed by a pathologist to identify disease lesions. Regions of interest (ROI) were identified and labeled as normal, adjacent normal, atypical adenomatous hyperplasia (AAH), adenocarcinoma *in situ* (AIS) and finally malignant adenocarcinoma (ADC) (**Fig 1**). From there unstained FFPE sections were stained with various multiplex immunofluorescent panels to better understand the immune changes following cancer progression. Panel 1 focuses on the PD-1/PD-L1 axis to better understand how checkpoint inhibition can potentially play a role in cancer progression. Multiplex immunofluorescence (7-plex) was performed with the following markers: $CD3^{+,}$ $CD8^{+}$, $CD68^{+}$, $PD\text{-}1^{+}$, $PD\text{-}L1^{+}$, PanC/K (tumor marker) and DAPI (nuclear marker) (**Fig 2**). This panel also examines the involvement of macrophages labeled by $CD68^{+}$ and how they can potentially play an inhibitory role by overexpressing PD-L1. Panel 2 focuses on T cell phenotyping with the multiplex immunofluorescence (7-plex) composed of following markers: $CD4^{+,}$ $CD8^{+}$, $FOXP3^{+}$, Granzyme B, Ki67, PanC/K (tumor marker) and DAPI (nuclear marker) (**Fig 3**). This panel investigates the various T cells being recruited into the tumor microenvironment and their potential interaction between tumor and other T cells. Granzyme B staining will highlight activation of $CD8^{+}$ T cells while $CD3^{+}$ $FOXP3^{+}$ $CD8^{-}$ cells will represent T regulatory cells that promote and immunosuppressive environment. These experiments are currently ongoing and can potentially shed some spatial perspectives on how immune cells can impact cancer progression. Additionally, more multiplex panels are being developed to focus on other areas of immune involvement in cancer.

Cancer Interception

These studies demonstrate that early detection of lung cancer in premalignancy is feasible and informative. Knowledge of lung cancer-associated immune biomarkers not only provides in-depth understanding of the pathogenesis of the disease, but also affords the opportunities for lung cancer early detection and interception. The concept of cancer interception introduced by Blackburn implies that in addition to preventative measures and cancer risk reduction, such as tobacco cessation, pharmacological and therapeutic approaches can be considered to prevent, delay or reverse carcinogenic progression to invasive disease in high risk patients [103]. Emerging techniques to help understand immune changes in cancer premalignancy may reveal potential targets for cancer interception at the earliest and most effective stages. In the following section a review is made on how immunotherapy can be utilized to modulating immune responses for lung cancer interception.

Immunotherapy for Cancer Prevention and Early-Stage Lung Cancer

Recent studies revealed immune cell infiltration and activation in lung premalignant lesions, which correlated with immunogenic somatic mutations and upregulation of immune checkpoints such as PD-L1 [122,123], suggesting that ICB may be a viable preventative strategy for lung cancer interception. An ongoing clinical trial is to evaluate pembrolizumab in treating patients with high-risk pulmonary nodules (NCT03634241).

ICB therapy has also been explored in early stage NSCLC patients in either adjuvant or neoadjuvant settings. Results from the PACIFIC trial, which studied adjuvant anti-PD-L1 therapy, durvalumab, compared with placebo in unresectable stage III patients treated with concurrent chemoradiation, demonstrated a significant increase in PFS [124]. Durvalumab is now approved as consolidation therapy following concurrent chemoradiation in unresectable stage III NSCLC patients. Currently, several large phase III trials are evaluating the use of adjuvant PD-1/PD-L1 blockade after surgical resection of NSCLC [125]. Initial results from a phase II study testing

neoadjuvant atezolizumab in resectable NSCLC revealed that preoperative treatment of atezolizumab is well tolerated, and the initial major pathologic response (MPR) rate is approximately 21%, while longer assessment is pending [126] [NCT02927301]. A recent phase II trial showed that Atezolizumab plus carboplatin and nab-paclitaxel given as a neoadjuvant regimen, achieved 56% major pathological response rate with no compromise to surgical resection and manageable treatment-related toxic effects [127] [NCT02716038]. Given the potential synergy between chemoradiation and ICB therapies, several ongoing trials are evaluating the combination of neoadjuvant chemo or radiation therapy with PD-1/PD-L1 blockade in early stage NSCLC with promising initial and interim results [125]. These studies highlight the potential of ICB as an effective therapeutic approach for lung cancer interception at early stages.

Discussion

Although recent advances in TKI and ICB therapies have revolutionized the treatment of lung cancer, durable responses are limited to only a subset of patients, and the overall survival rate for metastatic disease remains low. Therefore, innovative strategies to detect and intercept lung cancer at the earliest points of disease progression will have a major impact on patient care and clinical outcomes.

Among the most challenging problems in the field of precancer investigation is the availability of sufficient premalignant tissues collected spatially and temporally to allow for precise determination of genomic, epigenomic, transcriptomic and immune changes associated with tumor progression. Advances in obtaining precancerous tissues, and the possibility of serial biopsies of the same lesions longitudinally will enable studies that fully define the determinants of progression to invasive disease. Studies that focus on the molecular profiling of premalignant lung tissues and their associated immune microenvironment, as well as the course of immune recognition and adaptive responses across the spectrum of disease will provide further insight in the mechanisms

of lung cancer evolution and progression. This will identify actionable and personalized targets for lung cancer early interception.

Chapter 3 – Figure 1

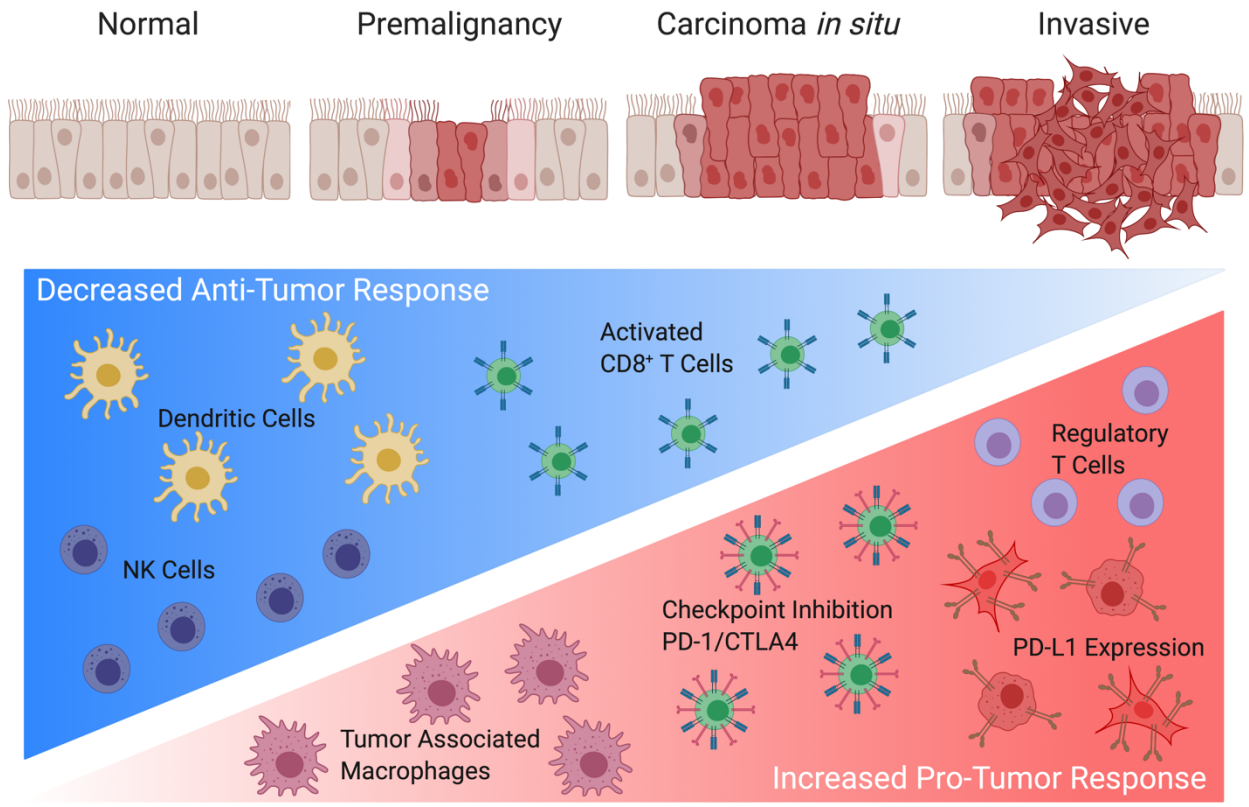

Figure 1

Immune Changes during Lung Cancer Progression

Graphical presentation showing progression from normal epithelium to premalignant cells advancing to invasive malignancy. Lung tumorigenesis is accompanied by a decrease in anti-tumor responses with the hallmark of decreased dendritic cells, activated natural killer (NK) cells and granzyme B secreting activated $CD8^+$ T cells. In addition, lung cancer progression is coupled with an increase in tumor associated macrophages, a prevalence of regulatory $CD4^+FOXP3^+$ T cells, an upregulation of PD-L1 expression in tumor and myeloid populations, and transition from activated T cells to an exhausted state identified by the expression of checkpoint inhibition markers, such as PD-1 and CTLA4. Images were made with Biorender.

Chapter 3 – Figure 2

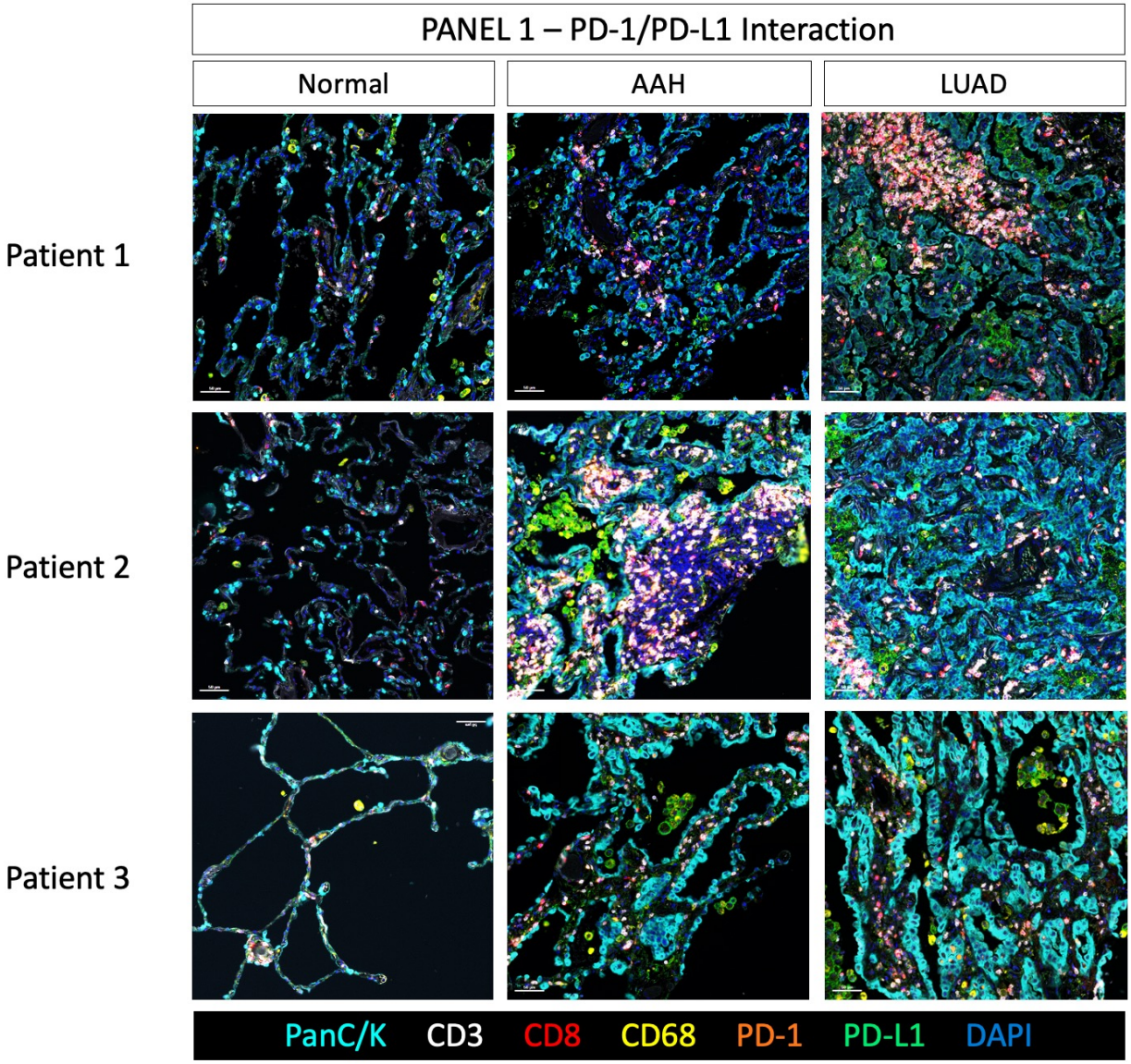

Figure 2

Representative images of multiplex immunofluorescence panel 1 on human tissues

Multiplex immunofluorescence (7-plex) was performed with the following markers: $CD3^{+,}$ $CD8^{+}$, $CD68^{+}$, $PD\text{-}1^{+}$, $PD\text{-}L1^{+}$, PanC/K (tumor marker) and DAPI (nuclear marker) on representative tissues. Three types of tissue sections are shown as identified by a pathologist: normal tissue, atypical adenomatous hyperplasia (AAH) and adenocarcinoma to represent malignant tissue.

Chapter 3 – Figure 3

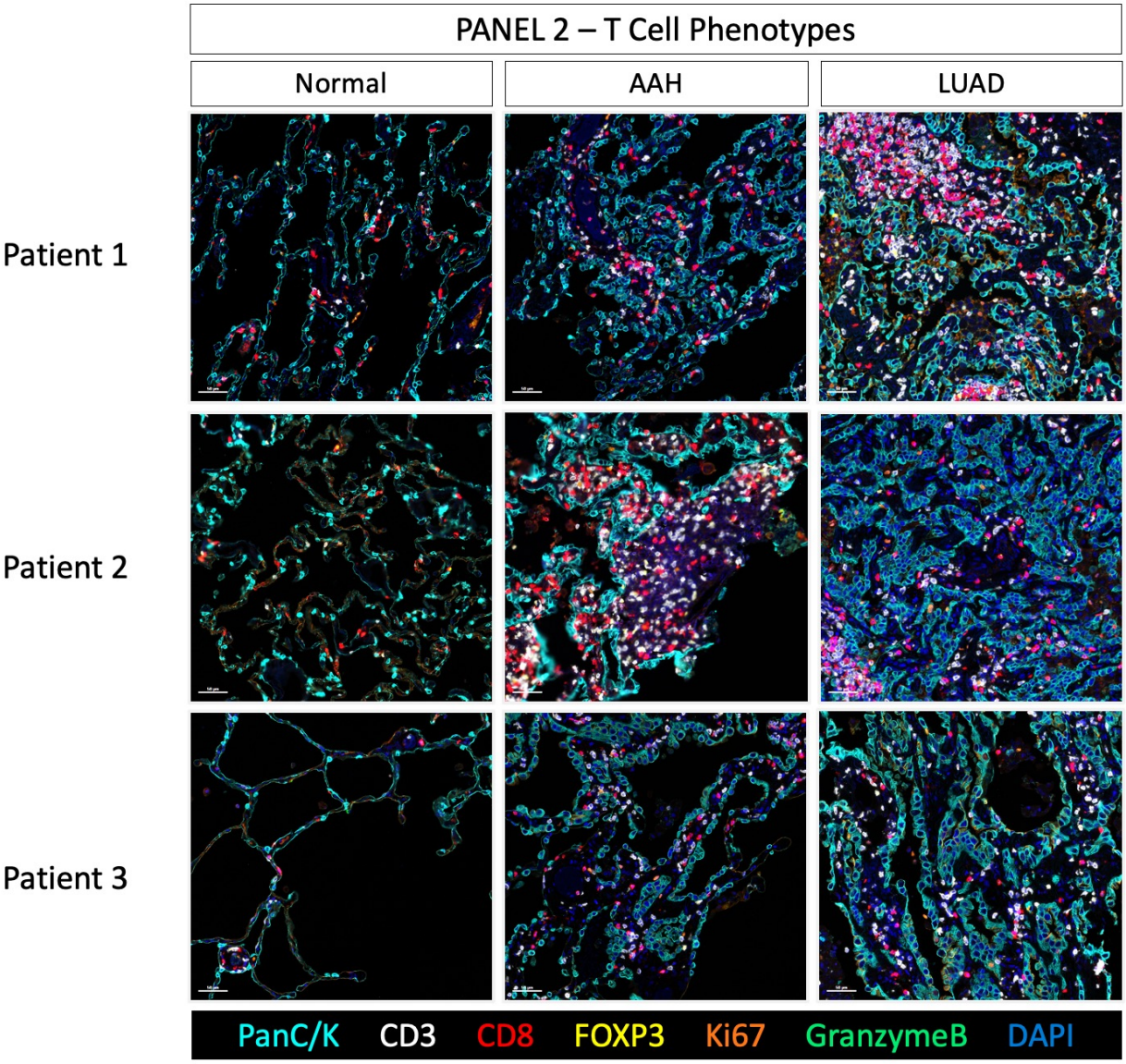

Figure 3

Representative images of multiplex immunofluorescence panel 2 on human tissues

Multiplex immunofluorescence (7-plex) was performed with the following markers: $CD4^{+,}$ $CD8^{+}$, $FOXP3^{+}$, Granzyme B, Ki67, PanC/K (tumor marker) and DAPI (nuclear marker) on representative tissues. Three types of tissue sections are shown as identified by a pathologist: normal tissue, atypical adenomatous hyperplasia (AAH) and adenocarcinoma to represent malignant tissue.

CONCLUDING REMARKS AND NEXT STEPS

Immune checkpoint blockade has revolutionized the lung cancer treatment paradigm within the last few years[8,80-84]. There has been a massive push to promote immunotherapy and various clinical trials have been undertaken to improve responses to ICB[128]. For example, IT injection of DC enhances the host tumor-specific immune response by providing access to the full repertoire of available tumor antigens[45,49,86,129]. Additionally, gene-engineered chemokines are designed to ameliorate tumor-induced immunosuppression and promote immune cell infiltration and activation. The combination of the two in our novel approach here has the potential to generate broader tumor-specific immune responses and obviates the need for the cumbersome patient-specific neoantigen prediction and validation. IT injection in the DC vaccine field has been established in the clinical setting with a completed phase I trial of IT CCL21-DC monotherapy in NSCLC and a second ongoing phase I trial of IT CCL21-DC combined with anti-PD-1 in NSCLC, demonstrating that the *in situ* DC vaccination approach, which is comparable to routine biopsy procedures, is safe and feasible with favorable safety profiles and promising clinical benefits[62,130].

The pre-clinical findings of our combination therapy of CCL21-DC and anti-PD-1 can potentially provide insight into the varied responses seen in the ongoing phase I clinical trial. Simultaneously, favorable patient outcomes will help inform the investigation of new areas of pre-clinical research utilizing this therapy. Taken together, the immune phenotyping of both pre-clinical and clinical studies will provide a synergistic approach to understanding the value of *in situ* DC vaccination. In addition to CCL21-DC, we also proposed CXCL9/10-DC as an additional potential gene-modified dendritic cell. Recent studies of somatic copy-number alterations (SCNAs) revealed potential associations with loss of CXCL9/10 in the TME, suggesting that aneuploid-dependent immune suppression may be combated by enhanced local expression of CXCL9/10 in the TME to improve the response to ICB[55,56]. A recent study further demonstrated that GPR182, a scavenging receptor for multiple chemokines including CXCL9/10, can limit antitumor immunity and response to ICB via chemokine scavenging in murine melanoma models[131]. In summary, we

hypothesize that CCL21-DC, with its clinical advancement, will be a strong candidate to potentiate ICB therapy while CXCL9/10-DC can enhance ICB efficacy in NSCLC bearing mutation profiles that may inhibit downstream effectors of CCL21-DC. In the future, the DC vaccination platform can be employed with other novel cytokine/ chemokine(s) or their combination to mechanistically target specific defects in the TME of NSCLC subtypes to enhance host tumor-specific T cell responses to achieve robust and durable efficacy.

Although recent advances in TKI and ICB therapies have revolutionized the treatment of lung cancer, durable responses are limited to only a subset of patients, and the overall survival rate for metastatic disease remains low. Therefore, innovative strategies to detect and intercept lung cancer at the earliest points of disease progression will have a major impact on patient care and clinical outcomes. Advances in obtaining precancerous tissues and the possibility of serial biopsies of the same lesions longitudinally will enable studies that fully define the determinants of progression to invasive disease. Studies that focus on the molecular profiling of premalignant lung tissues and their associated immune microenvironment, as well as the course of immune recognition and adaptive responses across the spectrum of disease will provide further insight into the mechanisms of lung cancer evolution and progression. This will identify actionable and personalized targets for early lung cancer intervention, potentially mitigating the mortality of this global disease.

EXPERIMENTAL METHODS

Cell lines and cell culture

Murine cell line 1940A were established from lung adenocarcinomas of conditional *Kras*^{G12D}*Tp53*$^{+/-}$*Lkb1*$^{-/-}$*Luc* (KPL) FVB mice and 1969B *Kras*^{G12D}*Tp53*$^{-/-}$ that express firefly luciferase[64]. The *Kras*^{G12D} LKR-13 line, established from a lung adenocarcinoma tumor from a *K-ras*^{LA1} mouse, was generously provided by Dr. Jonathan Kurie[132]. KPL-3M cell line with increased mutational burden was generated by *in vitro* exposure a KPL cell line to *N*-methyl-*N*-nitrosourea (MNU) as previously described[64]. Cell lines were maintained in culture media (RPMI-1640 medium supplemented with 10% FBS and 1% penicillin/streptomycin) at 37ºC in a humidified atmosphere of 5% CO_2, and utilized before 5 passages.

Generation of CCL21-DC

Bone marrow-derived DCs were generated as previously described[59]. Briefly bone marrow cells were cultured in DC media: 10% FBS in RPMI 1640 with 20ng/mL murine GM-CSF (Peprotech) and 10ng/mL murine IL-4 (Peprotech). The cells were seeded at concentration of 3 x 10^6 cells/mL into a sterile non-tissue culture-treated six-well plastic plate (Falcon) at 2 mL per well in a humidified CO_2 incubator (37°C, 5% CO_2). At day 3, the condition cultured media was changed with fresh media without depletion of cells. On the day of transduction at day 6, dendritic cells were harvested by gently pipetting loosely adherent and floating cells into a 15mL tube. Cells were then resuspended at a concentration of 3 x 10^6 cells/mL into virus media and plated at 3 mL per well into a new non-tissue culture-treated six-well plastic plate. Cells were then spin-fected at 800 x *g* for 2 hours at 32°C with pHIV-CCL21. Following transduction, cells were collected from the six-well and washed two times with DPBS (Corning) prior to injection. DC Viability was assessed by Trypan-blue staining before and after *Ccl21* transduction for all experiments.

Generation of CXCL9/10-DC

Bone marrow-derived DCs were generated as previously described[59]. Briefly bone marrow cells were cultured in DC media: 10% FBS in RPMI 1640 with 20ng/mL murine GM-CSF (Peprotech) and 10ng/mL murine IL-4 (Peprotech). The cells were seeded at concentration of 3 x 10^6 cells/mL into a sterile non-tissue culture-treated six-well plastic plate (Falcon) at 2 mL per well in a humidified CO_2 incubator (37°C, 5% CO_2). At day 3, the condition cultured media was changed with fresh media without depletion of cells. On the day of transduction at day 6, dendritic cells were harvested by gently pipetting loosely adherent and floating cells into a 15mL tube. Cells were then resuspended at a concentration of 3 x 10^6 cells/mL into virus media and plated at 3 mL per well into a new non-tissue culture-treated six-well plastic plate. Cells were then spin-fected at 800 x *g* for 2 hours at 32°C with pHIV-CXCL9 or pHIV-CXCL10. Following transduction, cells were collected from the six-well and washed two times with DPBS (Corning) prior to injection. Equal number cells transduced to make CXCL9-DC are combined with CXCL10-DC to make CXCL9/10-DC. DC Viability was assessed by Trypan-blue staining before and after *Ccl21* transduction for all experiments.

Dextran FITC

FITC-Dextran from Sigma (Catalog# FD40S) solution was made at a concentration of 25 mg/mL in Milli-Q water. FACS tubes were pre-chilled and for each condition 0.2-2x10^6 cells were placed in 200 uL of DC culture media, RPMI+10%FBS (Corning RPMI catalog# 10040CV, Gemini FBS catalog#100-500). 10 uL of the FITC-Dextran solution was added to the +FITC-Dextran conditions and either placed at 4°C or 37°C for 15 minutes. The No FITC-Dextran condition was incubated at 37°C for 15 minutes. After 15 minutes 1 mL of cold 1X DPBS (Corning catalog# 21031CV) was added to each FACS tube and spun for 5 minutes at 1500 RPM. After spinning, the supernatant was decanted and cells were incubated with CD86-PE (Biolegend catalog #374205) diluted 1:30 in FACS buffer, 2% FBS in 1X DPBS, for 15 minutes at 4°C. Cells were washed by adding 1mL

of FACS buffer and spinning as above. After spinning, supernatant was decanted and 100 uL of 0.5% Formalin (Epredia catalog# 5705) diluted in 1X DPBS was added to FACS tube and incubated for 20 minutes at room temperature. Cells were washed with FACS buffer and again spun down. Supernatant was decanted and cells were suspended in FACS buffer and analyzed by flow cytometry using the Agilent NovoCyte Quanteon Flow Cytometer.

ELISA

Mouse CCL21 ELISA was performed using the R&D Systems Mouse CCL21/6Ckine DuoSet ELISA Kit (Catalog# DY457) following the manufacturer's directions. Mouse CXCL9 (Catalog# DY#492) and CXCL10 ELISA (Catalog# DY466) were performed with R&D Systems DuoSet ELISA kits as well. The absorbance readings were taken using a BioRad absorbance plate reader. A standard curve was created by plotting the mean absorbance for each standard on the y-axis against the concentration on the x-axis and a best fit curve was drawn through the points on the graph and sample concentrations were determined based on this curve.

***In vivo* studies**

FVB/NCrl mice and 129-E mice were purchased from Charles River Laboratories. Tumor cells were implanted in 7-9-week-old mice subcutaneously at optimal doses as indicated in figure legends. Tumor length and width were measured by caliper and the volume calculated by the equation: 0.4*length*width^2. For immunotherapy studies, mice bearing ~50mm^3 tumors were randomized and treated with isotype control, genetically engineered as made above, IP 200 ug of anti-PD-1 antibody (BioXcell, Clone RMP1-14) or combination as illustrated in the figures. In secondary tumor challenge studies, mice were euthanized when tumor volume reached 12000 mm^3. Mice were housed in pathogen-free facilities at UCLA and all procedures were approved by the UCLA Animal Research Committee. Other experiments include anti-PD-L1 antibody (BioXcell, Clone 10F.9G2), mouse anti-CD4 for depletion (BioXcell, Clone GK1.5), mouse anti-CD8 for

depletion (BioXcell, Clone 2.43), mouse anti-CXCR3 antibody (BioXcell, Clone CXCR3-173), Fingolimod hydrochloride (Cayman, 10006292).

scRNA-seq sequencing

Single-cell suspension of murine tumors were prepared as previously described[64]. Cells were stained with Zombie-NIR LIVE/DEAD stain and CD45 antibody for 20 min a 4°C. Viable leukocytes were sorted using BD Biosceinces Aria II cell sorter with 100-mm nozzle. Samples were deliverd to the UCLA Technology Center for Genomics & Bioinformatics and processed for 10X Single Cell 3' Gene Expression V3 with Novaseq S2 with paired ends. Alternatively, RNA was isolated from sorted cells using the Qiagen RNeasy Plus Micro Kit per the manufacturer's instructions.

Immunophenotyping by flow cytometry

Single-cell suspension of murine spleens and tumors were prepared as previously described[64]. Staining was performed in the dark. Surface staining and intracellular staining for FOXP3 and Ki-67 were performed as previously described[64]. IFNg and TNFa production was evaluated by intracellular staining after *in vitro* stimulation with Cell Stimulation Cocktail (eBioscience) for 4 hours, utilizing the intracellular fixation and permeabilization buffer set (eBioscience). Data acquisition was performed on Attune NxT cytometer (ThermoFisher) and Novocyte Quanteon (Agilent), and data analyzed by FlowJo software (TreeStar).

Genomic profiling

Genomic profiling of tumor cells were prepared as previously described[64]. Briefly, genomic DNA was extracted from tumor cells (Qiagen, DNeasy blood and tissue kit) for WES. Tail DNA from three FVB/NCrl mice was included as a normal reference for variant calls. Libraries for WES were prepared using the Kapa Hyper Prep Kit (Roche, KK8504) followed by exome enrichment with SeqCap EZ Share Developer Probe (Roche, 08333025001). Sequencing was performed on

Hiseq3000 instrument as 150 bp pair-end runs with the aim of 100x depth at UCLA TCGB Core facility. Sequence reads were aligned to the mouse genome (mm10) with Burrows-Wheeler Aligner (v 0.7.17), then marked for duplicates and re-calibrated as suggested by Genome Analysis Toolkit (GATK). Strelka2 was utilized to call variants between cell line and the associated normal tail genome. When more than one reference normal genome was available (e.g. FVB mice), variant calls were performed to the individual normal genome independently and kept for down-stream analyses if they were called based on both reference genomes. Finally, a variant was called a mutation if (1) it was not in the germline mutation panel, determined from the FVB and 129-E tail genomes, (2) it was not supported by any read in the associated normal genome, (3) it was detected by at least 5 reads in cell lines, and (4) its variant allelic frequency (VAF) was > 0.1. The variants that passed these criteria were then annotated by Ensembl Variant Effect Predictor as nonsynonymous mutations. Mutation with VAF ≥ 0.4 in all related cell lines including the parental cell line were defined as truncal. Shared mutations among members of the family with VAF < 0.4 were named as branch. Mutations with VAF < 0.4 which were specific to one cell line and not shared with the related cell lines were defined as private.

Multiplex Immunofluorescence

Tumor samples or tissue collected and fixed for 24-48 hours before paraffin embedding. MIF was performed utilizing the Ventana Discovery Ultra (Roche) and Opal fluorophores (Akoya Biosciences). 5um-thick tissue sections on Superfrost microscopic slides (VWR International) were deparaffinized using EZ-Prep reagent (Roche) followed by antigen retrieval in CC1 buffer (pH 9, 95 °C; Roche). Discovery Inhibitor (Roche) was applied to inhibit enzymatic activities followed by 6 sequential rounds of staining. Each round included the addition of a primary antibody followed by detection using the OmniMap secondary antibody (Roche). Signal amplification was performed utilizing Opal fluorophores in the conditions suggested by the manufacturer. Between rounds of staining the tissue sections underwent heat-induced epitope retrieval to remove the

primary-secondary-HRP antibody complexes before staining with the subsequent antibody. The primary antibodies and corresponding fluorophores were stained with Opal 480, 520, 570, 620, 690 and 780 (Akoya Biosciences). The slides were then counterstained with Spectral DAPI (Akoya Biosciences) and mounted with ProLong Diamond antifade mounting medium (Thermo Fisher Scientific). Stained slides were imaged using the Vectra Polaris imaging system (Akoya Biosciences). A whole slide scan was acquired with 20x resolution and imported into the inForm software (Akoya Biosciences) followed by unmixing the spectral libraries, cell segmentation and cell phenotyping. Whole biopsy regions from each slide were then analyzed to identify and characterize the cells. The data was then exported and graphed with Prism (Graphpad). The representative images were exported using inForm software following spectral unmixing. Alternatively, whole slide scans were performed followed by spectral unmixing and imported in HALO (Indica Labs) for stitching and whole slide spatial analysis.

QUANTIFICATION AND STATISTICAL ANALYSIS

Experiments were performed at least three times, unless otherwise indicated. Results from one representative experiment are shown. Statistical analyses were performed in Prism 9 (GraphPad) unless otherwise noted. Statistical significance was determined using an unpaired, parametric *t*-test with 95% confidence interval. Results are reported as mean ± SEM, unless indicated. Tumor growth curve was analyzed using two-way ANOVA with Tukey post-test for time-associated comparison among multiple groups. Statistical significance is reported as the following: * $P<0.05$; **, $P< 0.01$; ***, $P<0.001$; ****, $P< 0.0001$.

REFERENCES

1 Torre, L. A. *et al.* Global cancer statistics, 2012. *CA Cancer J Clin* **65**, 87-108, doi:10.3322/caac.21262 (2015).

2 Tang, Y. *et al.* Biomarkers for early diagnosis, prognosis, prediction, and recurrence monitoring of non-small cell lung cancer. *Onco Targets Ther* **10**, 4527-4534 (2017).

3 Siegel, R. L., Miller, K. D., Fuchs, H. E. & Jemal, A. Cancer statistics, 2022. *CA Cancer J Clin* **72**, 7-33, doi:10.3322/caac.21708 (2022).

4 Howlader N., N. A. M., Krapcho M., Miller D., Bishop K., Altekruse S.F., Kosary C.L., Yu M., Ruhl J., Tatalovich Z., Mariotto A., Lewis D.R., Chen H.S., Feuer E.J., Cronin K.A. SEER Cancer Statistics Review, 1975-2013. *National Cancer Institute. Bethesda, MD.*, doi:https://seer.cancer.gov/csr/1975_2013/ (2016).

5 Molina, J. R., Yang, P., Cassivi, S. D., Schild, S. E. & Adjei, A. A. Non-small cell lung cancer: epidemiology, risk factors, treatment, and survivorship. *Mayo Clin Proc* **83**, 584-594, doi:10.4065/83.5.584 (2008).

6 Chen, Z., Fillmore, C. M., Hammerman, P. S., Kim, C. F. & Wong, K. K. Non-small-cell lung cancers: a heterogeneous set of diseases. *Nat Rev Cancer* **14**, 535-546, doi:10.1038/nrc3775 (2014).

7 Herbst, R. S., Morgensztern, D. & Boshoff, C. The biology and management of non-small cell lung cancer. *Nature* **553**, 446-454, doi:10.1038/nature25183 (2018).

8 Doroshow, D. B. *et al.* Immunotherapy in Non-Small Cell Lung Cancer: Facts and Hopes. *Clin Cancer Res* **25**, 4592-4602, doi:10.1158/1078-0432.CCR-18-1538 (2019).

9 Pacheco, J. M., Camidge, D. R., Doebele, R. C. & Schenk, E. A Changing of the Guard: Immune Checkpoint Inhibitors With and Without Chemotherapy as First Line Treatment for Metastatic Non-small Cell Lung Cancer. *Front Oncol* **9**, 195, doi:10.3389/fonc.2019.00195 (2019).

10 Zhang, C., Leighl, N. B., Wu, Y. L. & Zhong, W. Z. Emerging therapies for non-small cell lung cancer. *J Hematol Oncol* **12**, 45, doi:10.1186/s13045-019-0731-8 (2019).

11 Jamieson, N. B. & Maker, A. V. Gene-expression profiling to predict responsiveness to immunotherapy. *Cancer Gene Ther* **24**, 134-140 (2017).

12 Sharma, P., Hu-Lieskovan, S., Wargo, J. A. & Ribas, A. Primary, Adaptive, and Acquired Resistance to Cancer Immunotherapy. *Cell* **168**, 707-723 (2017).

13 Draghi, A., Chamberlain, C. A., Furness, A. & Donia, M. Acquired resistance to cancer immunotherapy. *Semin Immunopathol* **41**, 31-40, doi:10.1007/s00281-018-0692-y (2019).

14 Langer, C. J. *et al.* Carboplatin and pemetrexed with or without pembrolizumab for advanced, non-squamous non-small-cell lung cancer: a randomised, phase 2 cohort of the open-label KEYNOTE-021 study. *Lancet Oncol* **17**, 1497-1508, doi:10.1016/S1470-2045(16)30498-3 (2016).

15 Gandhi, L. & Garassino, M. C. Pembrolizumab plus Chemotherapy in Lung Cancer. *N Engl J Med* **379**, e18, doi:10.1056/NEJMc1808567 (2018).

16 Paz-Ares, L. *et al.* Pembrolizumab plus Chemotherapy for Squamous Non-Small-Cell Lung Cancer. *N Engl J Med* **379**, 2040-2051, doi:10.1056/NEJMoa1810865 (2018).

17 Socinski, M. A. *et al.* Atezolizumab for First-Line Treatment of Metastatic Nonsquamous NSCLC. *N Engl J Med* **378**, 2288-2301, doi:10.1056/NEJMoa1716948 (2018).

18 Kazandjian, D., Keegan, P., Suzman, D. L., Pazdur, R. & Blumenthal, G. M. Characterization of outcomes in patients with metastatic non-small cell lung cancer treated with programmed cell death protein 1 inhibitors past RECIST version 1.1-defined disease progression in clinical trials. *Semin Oncol* **44**, 3-7, doi:10.1053/j.seminoncol.2017.01.001 (2017).

19 Herbst, R. S. *et al.* Predictive correlates of response to the anti-PD-L1 antibody MPDL3280A in cancer patients. *Nature* **515**, 563-567, doi:10.1038/nature14011 (2014).

20 Tumeh, P. C. *et al.* PD-1 blockade induces responses by inhibiting adaptive immune resistance. *Nature* **515**, 568-571, doi:10.1038/nature13954 (2014).

21 Robert, L. *et al.* Distinct immunological mechanisms of CTLA-4 and PD-1 blockade revealed by analyzing TCR usage in blood lymphocytes. *Oncoimmunology* **3**, e29244, doi:10.4161/onci.29244 (2014).

22 Rizvi, N. A. *et al.* Cancer immunology. Mutational landscape determines sensitivity to PD-1 blockade in non-small cell lung cancer. *Science* **348**, 124-128 (2015).

23 Zou, W., Wolchok, J. D. & Chen, L. PD-L1 (B7-H1) and PD-1 pathway blockade for cancer therapy: Mechanisms, response biomarkers, and combinations. *Sci Transl Med* **8**, 328rv324 (2016).

24 Garon, E. B. *et al.* Pembrolizumab for the treatment of non-small-cell lung cancer. *N Engl J Med* **372**, 2018-2028 (2015).

25 McGranahan, N. *et al.* Clonal neoantigens elicit T cell immunoreactivity and sensitivity to immune checkpoint blockade. *Science* **351**, 1463-1469 (2016).

26 Gettinger, S. N. *et al.* A dormant TIL phenotype defines non-small cell lung carcinomas sensitive to immune checkpoint blockers. *Nat Commun* **9**, 3196 (2018).

27 Ayers, M. *et al.* IFN-gamma-related mRNA profile predicts clinical response to PD-1 blockade. *J Clin Invest* **127**, 2930-2940, doi:10.1172/JCI91190 (2017).

28 Litchfield, K. *et al.* Meta-analysis of tumor- and T cell-intrinsic mechanisms of sensitization to checkpoint inhibition. *Cell* **184**, 596-614 e514, doi:10.1016/j.cell.2021.01.002 (2021).

29 McGranahan, N. *et al.* Allele-Specific HLA Loss and Immune Escape in Lung Cancer Evolution. *Cell* **171**, 1259-1271 e1211, doi:10.1016/j.cell.2017.10.001 (2017).

30 Marty, R. *et al.* MHC-I Genotype Restricts the Oncogenic Mutational Landscape. *Cell* **171**, 1272-1283 e1215, doi:10.1016/j.cell.2017.09.050 (2017).

31 Skoulidis, F. *et al.* STK11/LKB1 Mutations and PD-1 Inhibitor Resistance in KRAS-Mutant Lung Adenocarcinoma. *Cancer Discov* **8**, 822-835 (2018).

32 Koyama, S. *et al.* STK11/LKB1 Deficiency Promotes Neutrophil Recruitment and Proinflammatory Cytokine Production to Suppress T-cell Activity in the Lung Tumor Microenvironment. *Cancer Res* **76**, 999-1008 (2016).

33 Li, R. *et al.* Inhibition of Granulocytic Myeloid-Derived Suppressor Cells Overcomes Resistance to Immune Checkpoint Inhibition in LKB1-Deficient Non-Small Cell Lung Cancer. *Cancer Res* **81**, 3295-3308, doi:10.1158/0008-5472.CAN-20-3564 (2021).

34 Dubinett, S. M., Batra, R. K., Miller, P. W. & Sharma, S. Tumor antigens in thoracic malignancy. *Am J Respir Cell Mol Biol* **22**, 524-527, doi:10.1165/ajrcmb.22.5.f186 (2000).

35 Rosenthal, R. *et al.* Neoantigen-directed immune escape in lung cancer evolution. *Nature* **567**, 479-485, doi:10.1038/s41586-019-1032-7 (2019).

36 Sharma, S. *et al.* T cell-derived IL-10 promotes lung cancer growth by suppressing both T cell and APC function. *Journal of Immunology* **163**, 5020-5028 (1999).

37 Srivastava, M. K. *et al.* Myeloid suppressor cells and immune modulation in lung cancer. *Immunotherapy* **4**, 291-304, doi:10.2217/imt.11.178 (2012).

38 Zhu, L. X. *et al.* IL-10 mediates sigma 1 receptor-dependent suppression of antitumor immunity. *J Immunol* **170**, 3585-3591 (2003).

39 Sharma, S. *et al.* Tumor cyclooxygenase-2/prostaglandin E2-dependent promotion of FOXP3 expression and CD4+ CD25+ T regulatory cell activities in lung cancer. *Cancer Res* **65**, 5211-5220, doi:65/12/5211 [pii]10.1158/0008-5472.CAN-05-0141 (2005).

40 Baratelli, F. *et al.* PGE(2) contributes to TGF-beta induced T regulatory cell function in human non-small cell lung cancer. *Am J Transl Res* **2**, 356-367 (2010).

41 Simoni, Y. *et al.* Bystander CD8(+) T cells are abundant and phenotypically distinct in human tumour infiltrates. *Nature* **557**, 575-579, doi:10.1038/s41586-018-0130-2 (2018).

42 Scheper, W. *et al.* Low and variable tumor reactivity of the intratumoral TCR repertoire in human cancers. *Nat Med* **25**, 89-94, doi:10.1038/s41591-018-0266-5 (2019).

43 Yost, K. E. *et al.* Clonal replacement of tumor-specific T cells following PD-1 blockade. *Nat Med* **25**, 1251-1259, doi:10.1038/s41591-019-0522-3 (2019).

44 Liu, B. *et al.* Temporal single-cell tracing reveals clonal revival and expansion of precursor exhausted T cells during anti-PD-1 therapy in lung cancer. *Nature Cancer* **3**, 108-121, doi:10.1038/s43018-021-00292-8 (2022).

45 Santos, P. M. & Butterfield, L. H. Dendritic Cell-Based Cancer Vaccines. *J Immunol* **200**, 443-449, doi:10.4049/jimmunol.1701024 (2018).

46 Saxena, M. & Bhardwaj, N. Re-Emergence of Dendritic Cell Vaccines for Cancer Treatment. *Trends Cancer* **4**, 119-137 (2018).

47 Hammerich, L. *et al.* Systemic clinical tumor regressions and potentiation of PD1 blockade with in situ vaccination. *Nat Med* **25**, 814-824, doi:10.1038/s41591-019-0410-x (2019).

48 Khalil, D. N. *et al.* In situ vaccination with defined factors overcomes T cell exhaustion in distant tumors. *J Clin Invest* **129**, 3435-3447, doi:10.1172/JCI128562 (2019).

49 Saxena, M., van der Burg, S. H., Melief, C. J. M. & Bhardwaj, N. Therapeutic cancer vaccines. *Nat Rev Cancer* **21**, 360-378, doi:10.1038/s41568-021-00346-0 (2021).

50 Spranger, S., Dai, D., Horton, B. & Gajewski, T. F. Tumor-Residing Batf3 Dendritic Cells Are Required for Effector T Cell Trafficking and Adoptive T Cell Therapy. *Cancer Cell* **31**, 711-723 e714, doi:10.1016/j.ccell.2017.04.003 (2017).

51 House, I. G. *et al.* Macrophage-Derived CXCL9 and CXCL10 Are Required for Antitumor Immune Responses Following Immune Checkpoint Blockade. *Clin Cancer Res* **26**, 487-504, doi:10.1158/1078-0432.CCR-19-1868 (2020).

52 Zhao, Y., Yu, X. & Li, J. Manipulation of immunevascular crosstalk: new strategies towards cancer treatment. *Acta Pharm Sin B* **10**, 2018-2036, doi:10.1016/j.apsb.2020.09.014 (2020).

53 Dangaj, D. *et al.* Cooperation between Constitutive and Inducible Chemokines Enables T Cell Engraftment and Immune Attack in Solid Tumors. *Cancer Cell* **35**, 885-900 e810, doi:10.1016/j.ccell.2019.05.004 (2019).

54 Romero, J. M. *et al.* A Four-Chemokine Signature Is Associated with a T-cell-Inflamed Phenotype in Primary and Metastatic Pancreatic Cancer. *Clin Cancer Res* **26**, 1997-2010, doi:10.1158/1078-0432.CCR-19-2803 (2020).

55 Davoli, T., Uno, H., Wooten, E. C. & Elledge, S. J. Tumor aneuploidy correlates with markers of immune evasion and with reduced response to immunotherapy. *Science* **355**, doi:10.1126/science.aaf8399 (2017).

56 William, W. N., Jr. *et al.* Immune evasion in HPV(-) head and neck precancer-cancer transition is driven by an aneuploid switch involving chromosome 9p loss. *Proc Natl Acad Sci U S A* **118**, doi:10.1073/pnas.2022655118 (2021).

57 Li, T. *et al.* TIMER: A Web Server for Comprehensive Analysis of Tumor-Infiltrating Immune Cells. *Cancer Res* **77**, e108-e110, doi:10.1158/0008-5472.CAN-17-0307 (2017).

58 Aran, D., Hu, Z. & Butte, A. J. xCell: digitally portraying the tissue cellular heterogeneity landscape. *Genome Biol* **18**, 220, doi:10.1186/s13059-017-1349-1 (2017).

59 Baratelli, F. *et al.* Pre-clinical characterization of GMP grade CCL21-gene modified dendritic cells for application in a phase I trial in non-small cell lung cancer. *J Transl Med* **6**, 38 (2008).

60 Yang, S. C. *et al.* Intrapulmonary administration of CCL21 gene-modified dendritic cells reduces tumor burden in spontaneous murine bronchoalveolar cell carcinoma. *Cancer Res* **66**, 3205-3213 (2006).

61 Yang, S. C. *et al.* Intratumoral administration of dendritic cells overexpressing CCL21 generates systemic antitumor responses and confers tumor immunity. *Clin Cancer Res* **10**, 2891-2901 (2004).

62 Lee, J. M. *et al.* Phase I Trial of Intratumoral Injection of CCL21 Gene-Modified Dendritic Cells in Lung Cancer Elicits Tumor-Specific Immune Responses and CD8+ T-cell Infiltration. *Clin Cancer Res* **23**, 4556-4568 (2017).

63 Salehi-Rad, R. *et al.* Novel Kras-mutant murine models of non-small cell lung cancer possessing co-occurring oncogenic mutations and increased tumor mutational burden. *Cancer Immunol Immunother*, doi:10.1007/s00262-020-02837-9 (2021).

64 Salehi-Rad, R. *et al.* Novel Kras-mutant murine models of non-small cell lung cancer possessing co-occurring oncogenic mutations and increased tumor mutational burden. *Cancer Immunol Immunother* **70**, 2389-2400, doi:10.1007/s00262-020-02837-9 (2021).

65 Metzemaekers, M., Vanheule, V., Janssens, R., Struyf, S. & Proost, P. Overview of the Mechanisms that May Contribute to the Non-Redundant Activities of Interferon-Inducible CXC Chemokine Receptor 3 Ligands. *Front Immunol* **8**, 1970, doi:10.3389/fimmu.2017.01970 (2017).

66 Jin, H. T. *et al.* Cooperation of Tim-3 and PD-1 in CD8 T-cell exhaustion during chronic viral infection. *Proc Natl Acad Sci U S A* **107**, 14733-14738, doi:10.1073/pnas.1009731107 (2010).

67 Im, S. J. *et al.* Defining CD8+ T cells that provide the proliferative burst after PD-1 therapy. *Nature* **537**, 417-421, doi:10.1038/nature19330 (2016).

68 Karin, N. CXCR3 Ligands in Cancer and Autoimmunity, Chemoattraction of Effector T Cells, and Beyond. *Front Immunol* **11**, 976, doi:10.3389/fimmu.2020.00976 (2020).

69 Bronger, H. *et al.* CXCL9 and CXCL10 predict survival and are regulated by cyclooxygenase inhibition in advanced serous ovarian cancer. *Br J Cancer* **115**, 553-563, doi:10.1038/bjc.2016.172 (2016).

70 Chen, D. S. & Mellman, I. Oncology meets immunology: the cancer-immunity cycle. *Immunity* **39**, 1-10, doi:10.1016/j.immuni.2013.07.012 (2013).

71 Cancer Genome Atlas Research, N. Comprehensive molecular profiling of lung adenocarcinoma. *Nature* **511**, 543-550, doi:10.1038/nature13385 (2014).

72 Ahn, E. *et al.* Role of PD-1 during effector CD8 T cell differentiation. *Proc Natl Acad Sci U S A* **115**, 4749-4754, doi:10.1073/pnas.1718217115 (2018).

73 Patsoukis, N., Wang, Q., Strauss, L. & Boussiotis, V. A. Revisiting the PD-1 pathway. *Sci Adv* **6**, doi:10.1126/sciadv.abd2712 (2020).

74 Gillette, M. A. *et al.* Proteogenomic Characterization Reveals Therapeutic Vulnerabilities in Lung Adenocarcinoma. *Cell* **182**, 200-225 e235, doi:10.1016/j.cell.2020.06.013 (2020).

75 Borst, J., Ahrends, T., Babala, N., Melief, C. J. M. & Kastenmuller, W. CD4(+) T cell help in cancer immunology and immunotherapy. *Nat Rev Immunol* **18**, 635-647, doi:10.1038/s41577-018-0044-0 (2018).

76 Ahrends, T. & Borst, J. The opposing roles of CD4(+) T cells in anti-tumour immunity. *Immunology*, doi:10.1111/imm.12941 (2018).

77 Williams, J. B. *et al.* Tumor heterogeneity and clonal cooperation influence the immune selection of IFN-gamma-signaling mutant cancer cells. *Nat Commun* **11**, 602, doi:10.1038/s41467-020-14290-4 (2020).

78 Nicos, M., Krawczyk, P., Crosetto, N. & Milanowski, J. The Role of Intratumor Heterogeneity in the Response of Metastatic Non-Small Cell Lung Cancer to Immune Checkpoint Inhibitors. *Front Oncol* **10**, 569202, doi:10.3389/fonc.2020.569202 (2020).

79 Li, S. *et al.* Characterization of neoantigen-specific T cells in cancer resistant to immune checkpoint therapies. *Proc Natl Acad Sci U S A* **118**, doi:10.1073/pnas.2025570118 (2021).

80 Gandhi, L. *et al.* Pembrolizumab plus Chemotherapy in Metastatic Non–Small-Cell Lung Cancer. *New England Journal of Medicine* **378**, 2078-2092, doi:10.1056/NEJMoa1801005 (2018).

81 Reck, M. *et al.* Pembrolizumab versus Chemotherapy for PD-L1-Positive Non-Small-Cell Lung Cancer. *The New England journal of medicine* **375**, 1823-1833, doi:10.1056/NEJMoa1606774 (2016).

82 Topalian, S. L. *et al.* Safety, activity, and immune correlates of anti-PD-1 antibody in cancer. *The New England journal of medicine* **366**, 2443-2454, doi:10.1056/NEJMoa1200690 (2012).

83 Borghaei, H. *et al.* Nivolumab versus Docetaxel in Advanced Nonsquamous Non-Small-Cell Lung Cancer. *The New England journal of medicine* **373**, 1627-1639, doi:10.1056/NEJMoa1507643 (2015).

84 Brahmer, J. *et al.* Nivolumab versus Docetaxel in Advanced Squamous-Cell Non-Small-Cell Lung Cancer. *The New England journal of medicine* **373**, 123-135, doi:10.1056/NEJMoa1504627 (2015).

85 McGranahan, N. *et al.* Allele-Specific HLA Loss and Immune Escape in Lung Cancer Evolution. *Cell* **171**, 1259-1271.e1211, doi:10.1016/j.cell.2017.10.001 (2017).

86 Perez, C. R. & De Palma, M. Engineering dendritic cell vaccines to improve cancer immunotherapy. *Nat Commun* **10**, 5408, doi:10.1038/s41467-019-13368-y (2019).

87 Santos, P. M. & Butterfield, L. H. Dendritic Cell–Based Cancer Vaccines. *The Journal of Immunology* **200**, 443-449, doi:10.4049/jimmunol.1701024 (2018).

88 Champiat, S. *et al.* Intratumoral Immunotherapy: From Trial Design to Clinical Practice. *Clinical cancer research : an official journal of the American Association for Cancer Research* **27**, 665-679, doi:10.1158/1078-0432.CCR-20-0473 (2021).

89 Sharma, S. *et al.* SLC/CCL21-mediated anti-tumor responses require IFNgamma, MIG/CXCL9 and IP-10/CXCL10. *Mol Cancer* **2**, 22 (2003).

90 Sharma, S. *et al.* CCL21 Chemokine Therapy for Lung Cancer. *Int Trends Immun* **1**, 10-15 (2013).

91 Lee, J. M. *et al.* Phase I Trial of Intratumoral Injection of CCL21 Gene-Modified Dendritic Cells in Lung Cancer Elicits Tumor-Specific Immune Responses and CD8(+) T-cell Infiltration. *Clinical cancer research : an official journal of the American Association for Cancer Research* **23**, 4556-4568, doi:10.1158/1078-0432.Ccr-16-2821 (2017).

92 Westcott, P. M. *et al.* The mutational landscapes of genetic and chemical models of Kras-driven lung cancer. *Nature* **517**, 489-492 (2015).

93 Chung, W.-J. *et al.* Kras mutant genetically engineered mouse models of human cancers are genomically heterogeneous. *Proceedings of the National Academy of Sciences* **114**, E10947-E10955, doi:10.1073/pnas.1708391114 (2017).

94 McFadden, D. G. *et al.* Mutational landscape of EGFR-, MYC-, and Kras-driven genetically engineered mouse models of lung adenocarcinoma. *Proc Natl Acad Sci U S A* **113**, E6409-E6417, doi:10.1073/pnas.1613601113 (2016).

95 Zilionis, R. *et al.* Single-Cell Transcriptomics of Human and Mouse Lung Cancers Reveals Conserved Myeloid Populations across Individuals and Species. *Immunity* **50**, 1317-1334 e1310, doi:10.1016/j.immuni.2019.03.009 (2019).

96 Bosteels, C. *et al.* Inflammatory Type 2 cDCs Acquire Features of cDC1s and Macrophages to Orchestrate Immunity to Respiratory Virus Infection. *Immunity* **52**, 1039-1056 e1039, doi:10.1016/j.immuni.2020.04.005 (2020).

97 Maier, B. *et al.* A conserved dendritic-cell regulatory program limits antitumour immunity. *Nature* **580**, 257-262, doi:10.1038/s41586-020-2134-y (2020).

98 Garris, C. S. *et al.* Successful Anti-PD-1 Cancer Immunotherapy Requires T Cell-Dendritic Cell Crosstalk Involving the Cytokines IFN-gamma and IL-12. *Immunity* **49**, 1148-1161 e1147, doi:10.1016/j.immuni.2018.09.024 (2018).

99 Ciucci, T. *et al.* The Emergence and Functional Fitness of Memory CD4(+) T Cells Require the Transcription Factor Thpok. *Immunity* **50**, 91-105 e104, doi:10.1016/j.immuni.2018.12.019 (2019).

100 Miller, B. C. *et al.* Subsets of exhausted CD8(+) T cells differentially mediate tumor control and respond to checkpoint blockade. *Nat Immunol* **20**, 326-336, doi:10.1038/s41590-019-0312-6 (2019).

101 Siddiqui, I. *et al.* Intratumoral Tcf1(+)PD-1(+)CD8(+) T Cells with Stem-like Properties Promote Tumor Control in Response to Vaccination and Checkpoint Blockade Immunotherapy. *Immunity* **50**, 195-211 e110, doi:10.1016/j.immuni.2018.12.021 (2019).

102 Mittal, D., Gubin, M. M., Schreiber, R. D. & Smyth, M. J. New insights into cancer immunoediting and its three component phases--elimination, equilibrium and escape. *Curr Opin Immunol* **27**, 16-25, doi:10.1016/j.coi.2014.01.004 (2014).

103 Blackburn, E. H. Cancer interception. *Cancer Prev Res (Phila)* **4**, 787-792, doi:10.1158/1940-6207.CAPR-11-0195 (2011).

104 Beane, J. *et al.* Detecting the Presence and Progression of Premalignant Lung Lesions via Airway Gene Expression. *Clin Cancer Res* **23**, 5091-5100, doi:10.1158/1078-0432.CCR-16-2540 (2017).

105 Ehrlich, P. Ueber den jetzigen Stand der Karzinomforschung. *Ned Tijdschr Geneeskd* **5**, 273–290 (1909).

106 Lawrence, H. S. *Cellular and humoral aspects of the hypersensitive states; a symposium held at the New York Academy of Medicine*. (P.B. Hoeber, 1959).

107 Burnet, F. M. The concept of immunological surveillance. *Prog Exp Tumor Res* **13**, 1-27, doi:10.1159/000386035 (1970).

108 Old, L. J. & Boyse, E. A. Antigens of tumors and leukemias induced by viruses. *Fed Proc* **24**, 1009-1017 (1965).

109 Dighe, A. S., Richards, E., Old, L. J. & Schreiber, R. D. Enhanced in vivo growth and resistance to rejection of tumor cells expressing dominant negative IFN gamma receptors. *Immunity* **1**, 447-456, doi:10.1016/1074-7613(94)90087-6 (1994).

110 Shinkai, Y. *et al.* RAG-2-deficient mice lack mature lymphocytes owing to inability to initiate V(D)J rearrangement. *Cell* **68**, 855-867, doi:10.1016/0092-8674(92)90029-c (1992).

111 Dunn, G. P., Bruce, A. T., Ikeda, H., Old, L. J. & Schreiber, R. D. Cancer immunoediting: from immunosurveillance to tumor escape. *Nat Immunol* **3**, 991-998, doi:10.1038/ni1102-991 (2002).

112 Dunn, G. P., Old, L. J. & Schreiber, R. D. The three Es of cancer immunoediting. *Annu Rev Immunol* **22**, 329-360, doi:10.1146/annurev.immunol.22.012703.104803 (2004).

113 Dunn, G. P., Old, L. J. & Schreiber, R. D. The immunobiology of cancer immunosurveillance and immunoediting. *Immunity* **21**, 137-148, doi:10.1016/j.immuni.2004.07.017 (2004).

114 Smyth, M. J., Godfrey, D. I. & Trapani, J. A. A fresh look at tumor immunosurveillance and immunotherapy. *Nat Immunol* **2**, 293-299, doi:10.1038/86297 (2001).

115 Global Burden of Disease Cancer, C. *et al.* Global, Regional, and National Cancer Incidence, Mortality, Years of Life Lost, Years Lived With Disability, and Disability-Adjusted Life-Years for 29 Cancer Groups, 1990 to 2017: A Systematic Analysis for the Global Burden of Disease Study. *JAMA Oncol*, doi:10.1001/jamaoncol.2019.2996 (2019).

116 National Lung Screening Trial Research, T. *et al.* Reduced lung-cancer mortality with low-dose computed tomographic screening. *N Engl J Med* **365**, 395-409, doi:10.1056/NEJMoa1102873 (2011).

117 National Lung Screening Trial Research, T. *et al.* Results of initial low-dose computed tomographic screening for lung cancer. *N Engl J Med* **368**, 1980-1991, doi:10.1056/NEJMoa1209120 (2013).

118 de Koning, H. J. *et al.* Reduced Lung-Cancer Mortality with Volume CT Screening in a Randomized Trial. *N Engl J Med* **382**, 503-513, doi:10.1056/NEJMoa1911793 (2020).

119 Campbell, J. D. *et al.* The Case for a Pre-Cancer Genome Atlas (PCGA). *Cancer Prev Res (Phila)* **9**, 119-124, doi:10.1158/1940-6207.CAPR-16-0024 (2016).

120 Srivastava, S., Ghosh, S., Kagan, J., Mazurchuk, R. & National Cancer Institute's, H. I. The Making of a PreCancer Atlas: Promises, Challenges, and Opportunities. *Trends Cancer* **4**, 523-536, doi:10.1016/j.trecan.2018.06.007 (2018).

121 Srivastava, S., Ghosh, S., Kagan, J. & Mazurchuk, R. The PreCancer Atlas (PCA). *Trends Cancer* **4**, 513-514, doi:10.1016/j.trecan.2018.06.003 (2018).

122 Krysan, K. *et al.* The Immune Contexture Associates with the Genomic Landscape in Lung Adenomatous Premalignancy. *Cancer Res* **79**, 5022-5033, doi:10.1158/0008-5472.CAN-19-0153 (2019).

123 Mascaux, C. *et al.* Immune evasion before tumour invasion in early lung squamous carcinogenesis. *Nature* **571**, 570-575, doi:10.1038/s41586-019-1330-0 (2019).

124 Antonia, S. J. *et al.* Durvalumab after Chemoradiotherapy in Stage III Non-Small-Cell Lung Cancer. *N Engl J Med* **377**, 1919-1929, doi:10.1056/NEJMoa1709937 (2017).

125 Rosner, S., Reuss, J. E. & Forde, P. M. PD-1 Blockade in Early-Stage Lung Cancer. *Annu Rev Med* **70**, 425-435, doi:10.1146/annurev-med-050217-025205 (2019).

126 Rusch, V. W. *et al.* Neoadjuvant atezolizumab in resectable non-small cell lung cancer (NSCLC): Initial results from a multicenter study (LCMC3). *Journal of Clinical Oncology* **36**, 8541-8541, doi:10.1200/JCO.2018.36.15_suppl.8541 (2018).

127 Shu, C. A. *et al.* Neoadjuvant atezolizumab and chemotherapy in patients with resectable non-small-cell lung cancer: an open-label, multicentre, single-arm, phase 2 trial. *Lancet Oncol* **21**, 786-795, doi:10.1016/S1470-2045(20)30140-6 (2020).

128 Zhou, F., Qiao, M. & Zhou, C. The cutting-edge progress of immune-checkpoint blockade in lung cancer. *Cell Mol Immunol* **18**, 279-293, doi:10.1038/s41423-020-00577-5 (2021).

129 Melero, I., Castanon, E., Alvarez, M., Champiat, S. & Marabelle, A. Intratumoural administration and tumour tissue targeting of cancer immunotherapies. *Nat Rev Clin Oncol* **18**, 558-576, doi:10.1038/s41571-021-00507-y (2021).

130 Liu, B. *et al.* Abstract CT226: A Phase I trial of in situ vaccination with autologous CCL21-modified dendritic cells (CCL21-DC) combined with pembrolizumab for advanced NSCLC. *Cancer Research* **79**, CT226-CT226, doi:10.1158/1538-7445.Am2019-ct226 (2019).

131 Torphy, R. J. *et al.* GPR182 limits antitumor immunity via chemokine scavenging in mouse melanoma models. *Nat Commun* **13**, 97, doi:10.1038/s41467-021-27658-x (2022).

132 Wislez, M. *et al.* Inhibition of mammalian target of rapamycin reverses alveolar epithelial neoplasia induced by oncogenic K-ras. *Cancer Res* **65**, 3226-3235, doi:10.1158/0008-5472.CAN-04-4420 (2005).